POLITECNICO DI MILANO

SCUOLA INTERPOLITECNICA DI DOTTORATO

Doctoral Program in Physics

Final Dissertation

Magnetic tunneling junctions for biosensing and antiferromagnet-based spintronic devices

Edoardo Albisetti

Tutor
prof. Riccardo Bertacco

Co-ordinator of the Research Doctorate Course
prof. Paola Taroni

February 2014

Alla mia famiglia

Abstract

Since the discovery of giant magnetoresistance in 1988 and its breakthrough application in data storage technology, magnetoresistive phenomena have been extensively studied and nowadays constitute the core of a variety of spintronic devices. Among them, magnetoresistive sensors in combination with magnetic markers are particularly suited for biosensing applications due their high sensitivity and ease of integration in compact lab-on-a-chip platforms.

This thesis deals with the realization and optimization of a biosensing platform based on magnetic tunneling junctions (MTJs), and on the development of novel spintronic devices comprising tunneling junctions whose magnetoresistance is governed by antiferromagnets, with no ferromagnets.

The starting point of this work was the fabrication of MTJ-based sensor arrays by magnetron sputtering and optical lithography. This task was carried out starting from the optimization of the single functional layers, up to the final integration of the microfabricated sensor chips with the microfluidic platform and with a multiplexed electronic setup for data acquisition. Our preliminary experiments on the detection of magnetic bead sedimentation led to the formulation of a new model for the sensor sensitivity to the magnetic markers, whose predictions were confirmed experimentally. Such model can be used for identifying the optimal working point on the sensor magnetoresistive curve, in order to maximize the sensitivity and reduce the limit of detection of the assays, as well as for realizing novel improved sensors starting from the design of their magnetic response.

The maximization of the sensor sensitivity was investigated also from the point of view of the spatial distribution of the magnetic beads on the sensor area. For addressing experimentally this issue in biomolecular recognition experiments, we developed a technique based on conventional optical lithography for creating micron-sized patterns of probe biomolecules such as single strand DNA. The detection of synthetic DNA hybridization events was successfully carried out both in conventionally functionalized and biopatterned sensors, showing a significant increase in the binding signal on biopatterned sensors, consistent with calculations. Our biosensing platform was also employed for detecting natural *Hepatitis E* virus DNA, with the aim of realizing an integrated Lab-on-a-Chip platform for the point-of-care detection of pathogens in the agri-food industry.

MTJ-based sensors, due to their extremely high sensitivity to weak magnetic fields, are very promising for the study of the activity of neural cells *in-vitro* through the detection of the magnetic fields generated by ionic currents. In these studies, the control over the growth and orientation of neurons with respect to the sensor is fundamental to have a detectable signal. Such control can be achieved patterning gradients of extracellular matrix (ECM) proteins in correspondence of the sensors. With this goal, we demonstrated that thermochemical nanolithography (TCNL) can be used for patterning gradients of ECM proteins combining the high control over the protein concentration with a nanometric resolution.

In parallel with the work on biosensing, the realization and studies on antiferromagnet-based tunneling junctions were carried out. The field of antiferromagnetic spintronics received a great boost with the demonstration of the first spintronic device whose transport is controlled by the tunneling anisotropic magnetoresistance (TAMR) in an antiferromagnet. Following this work, IrMn/MgO/Ta tunnel junctions (with no ferromagnetic materials) were fabricated in our group by sputtering and optical lithography. Field cooling experiments demonstrated the possibility to store magnetic information in such devices exploiting TAMR. In particular, two different metastable resistance states were reached performing field cooling across the Néel temperature of IrMn, with a different orientation of the applied magnetic field. In perspective, such tunneling junctions can be the starting point for developing a new kind of thermally assisted MRAM devices based on TAMR in antiferromagnets.

Preface

The present thesis reports most of the work carried out by the author, Edoardo Albisetti, from the beginning of his Ph.D. studies on January 1st, 2011. The main supervisor has been Prof. R. Bertacco from Politecnico di Milano. The experimental activity was performed in three institutions:

- Laboratory for Epitaxial Nanostructures on Silicon and for Spintronics (LNESS), Politecnico di Milano, Como, Italy.
- Istituto di Chimica del Riconoscimento Molecolare (ICRM-CNR), Milan, Italy.
- School of Physics, Georgia Institute of Technology, Atlanta GA, U.S. (9 months stay).

This Ph.D. work has resulted in the following publications and contributions. In the thesis, these papers will be referred to as, e.g. [P3]

Journal Papers

P1. Torti, A., Mondiali, V., Cattoni, A., Donolato, M., Albisetti, E., Haghiri-Gosnet, A. M., Vavassori, P., Bertacco, R. (2012). Single particle demultiplexer based on domain wall conduits. *Applied Physics Letters*, **101**(14), 142405. doi:10.1063/1.4755785

P2. Petti, D., Albisetti, E., Reichlová, H., Gazquez, J., Varela, M., Molina-Ruiz, M., Lopeandía, A. F., Olejník, K., Novák, V., Fina, I., Dkhil, B., Hayakawa, J., Marti, X., Wunderlich, J., Jungwirth, T., Bertacco, R. (2013). Storing magnetic information in IrMn/MgO/Ta tunnel junctions via field-cooling. *Applied Physics Letters*, **102**(19), 192404. doi:10.1063/1.4804429

P3. Albisetti, E., Petti, D., Cantoni, M., Damin, F., Torti, a, Chiari, M., & Bertacco, R. (2013). Conditions for efficient on-chip magnetic bead detection via magnetoresistive sensors. *Biosensors & Bioelectronics*, **47**, 213–7. doi:10.1016/j.bios.2013.03.016

P4. Petti, D., Torti, A., Damin, F., Sola, L., Rusnati, M., Albisetti, E., Bugatti, A., Bertacco, R., Chiari, M. (2014). Functionalization of gold surfaces with copoly (DMA-NAS-MAPS) by

dip coating: Surface characterization and hybridization tests. *Sensors and Actuators B: Chemical*, **190**, 234–242. doi:10.1016/j.snb.2013.08.077

P5. Albisetti, E., Petti, D., Damin, F., Cretich, M., Torti, A., Chiari, M., Bertacco, R. Photolithographic bio-patterning of magnetic sensors for biomolecular recognition. Submitted to *Sensors and Actuators B: Chemical*

P6. Savoini, M., Piovera, C., Rinaldi, C., Albisetti, E. Petti, D., Khorsand, A. R., Duò, L., Dallera, C., Cantoni, M., Bertacco, R., Finazzi, M., Carpene, E., Kimel, A. V., Kirilyuk, A., Rasing, Th. Bias-controlled ultrafast demagnetization in magnetic tunnel junctions. Submitted to *Physical Review Letters*

P7. Dal Conte, S., Conforti, M., Petti, D., Albisetti, E., Longhi, S., Bertacco, R., De Angelis, C., Cerullo, G. and Della Valle, G. Disentangling electrons and phonons nonlinear optical response in metal-dielectric Bragg filters. Submitted to *Physical Review B*

Conference proceedings

P8. Albisetti, E., Petti, D., Damin, F., Cretich, M., Bagnati, M., Sola, L., … Bertacco, R. (2013). Optimization of the bio-functionalized area of magnetic biosensors. *The European Physical Journal B*, **86**(6), 261. doi:10.1140/epjb/e2013-30676-4

Conference contributions

1. Poster presentation “On-chip brownian magnetorelaxometry with magnetic tunnel junctions” at Magnet 2011 conference, Turin, Italy (Feb 2011).

2. Talk “Magnetic tunneling junctions for bead magnetorelaxometry” al X Convegno Nazionale Materiali Nanofasici, Bologna, Italy (Sep 2011).

3. Talk “Selective bio-functionalization of magnetic biosensors by optical lithography” at XCVII National Congress of Italian Physical Society, L'Aquila, Italy (Sep 2011).

4. Poster presentation “Magnetic Tunneling Junctions for biomolecular detection” at SuperFOx conference, Como, Italy (Jun 2012).

5. Talk “Selective bio-functionalization of magnetic biosensors” at JEMS 2012, Parma, Italy (Sep 2012).

6. Talk “A tunable antiferromagnet-only-based magnetic tunnel junnction” at ICMFS 2012, Shanghai, China (Sep 2012).

7. Talk “Spintronic memory devices without ferromagnets: IrMn/MgO/Ta tunnel junctions exploiting field-cool anisotropic magnetoresistance” at Magnet 2013, Naples, Italy (Feb 2013).

8. Short Talk and Poster presentation “Photolithographic bio-patterning of magnetic sensors for biomolecular recognition” at MMB2013, Marina del Rey CA, USA (Apr 2013).

9. Talk “Nano-patterning of chemical gradients by thermochemical nano-lithography for neuronal guidance” at 7th Southeast Soft Material Workshop, Georgia Institute of Technology, Atlanta GA, U.S (May 2013).

Edoardo Albisetti
L-NESS – Physics Department
Politecnico di Milano
February 2014

Acknowledgements

In these past three years, I was fortunate enough to always have the support and inspiration from colleagues, friends and family. I was given the opportunity to meet and know great people from many places, and challenged to find what my real passions are. For all this, I am sincerely grateful.

First of all I would like to thank Prof. Riccardo Bertacco for supporting and trusting me and for his help and constant availability during all the phases of my activity. I would like to thank him especially for his encouragement and unlimited enthusiasm when pursuing novel ideas.

Thanks to Prof. Elisa Riedo and Prof. Jennifer Curtis for welcoming me in their groups at Georgia Tech and for giving me freedom and advice during my American stay.

Thanks to Dr. Marcella Chiari for the support and for making such a fruitful collaboration between ICRM and our group possible.

Thanks to Prof. Paola Taroni, for advising me during these years as co-ordinator of the doctoral program.

I would like to thank the whole L-NESS crew, which made via Anzani feel like a second home, and the ideal stimulating environment for research and drinking; starting from the incredible Marco Lion, half MacGyver, half Hetfield. Thanks to Greta and her unique diplomatic attitude which makes every day a surprise, to Christian and Matteo from the LASSE side of the world, to Massi, Fabio, Cecs, Jacopo, Danny, Erica and Laura for the time spent around Como and the insanely flavored Cecch-Isa house. Thanks to Eli and Andrea Mario for all the awesome adventures we had. Thanks to Monica, Valeria, Marco and Sergio for making the commute a real treat (and for waking me up at Como Borghi every day).

A special thanks to Daniela, for all the successes, failures, discussions and laughs we had during these years.

I am grateful to my colleagues and friends in Atlanta for the great time I spent at Georgia Tech. Thanks to Lucy, Douglas and Suenne, who taught me everything about the lab, to Alex for showing me, for real, how much freedom there is in the U.S., to Gao, for sharing cookies during the long nights spent at the lab in December. I would like to thank Dr. Keith Carroll for being so helpful with TCNL and for the inspiring discussions about physics, politics and karaoke. Thanks to the friends from the School of Physics, College of Computing and outside Georgia

Tech for all the biking, dancing and dining together. Thanks to Paolo and Luca, for bringing northern and southern Italy so close.

I would like to thank the colleagues from ICRM in Milan, in particular Marina, Francesco, Laura, Finchia for the long-lasting collaboration and their “magic” polymer.

I am grateful to my family for always discussing, advising and supporting my choices, and for listening with interest to obscure “magnetic” stories.

Finally, thanks to Edo, Max, Ale, Albe, Pol, Q, Crive, Piè, Jack, Pupi, Moli, Sad, Milly, Fra, and all the friends I was lucky to have throughout these years, for all the memories we share and for those we will.

Contents

List of figures

List of tables

1. Introduction

The work presented in this experimental Ph.D. thesis is focused on the development and realization of devices based on magnetic tunneling junctions (MTJs) and their applications in the fields of biosensing and antiferromagnet-based spintronics. This introduction gives an overview on the state of the art in magnetic biosensing technology and magnetoresistive spintronic devices, illustrating the context and motivations of this work. Finally, an outline of the topics presented in each section of the thesis is given.

1.1 Evolution and applications of magnetoresistance in magnetic multilayers

Magnetoresistance is the change in the electrical resistivity of a material under the influence of an external magnetic field. The first observation of such effect was carried out in 1856 by Lord Kelvin, who noticed a change in the resistance of nickel and iron according to the orientation of the applied magnetic field with respect to the direction of the current flow. The physical origin of such effect, the **Anisotropic Magnetoresistance (AMR)**, lies in the spin-orbit coupling. As the magnetization rotates, the conduction electrons undergo a different amount of scattering when traversing the lattice; macroscopically this effect is seen as a change in the electrical resistance of the material.[1] The change in the resistance due to AMR in conventional ferromagnetic transition metal alloys such as Permalloy ($Ni_{80}Fe_{20}$) is theoretically around 4% at room temperature.[2] The low magnitude of the AMR effect, and its intrinsic bulk nature, were the major drawbacks of AMR in technological applications, because with the shrinking of the components size, interface effects rather than bulk ones dominate the electrical transport.

This problems were overcome in 1988 by the discovery of **Giant Magnetoresistance (GMR)** in ferromagnetic multilayers.[3] The GMR effect was first observed in Fe/Cr multilayers in the so-called current-in-plane configuration (CIP), i.e. with a current flow parallel to the multilayer interfaces. In GMR, the resistance of the system is determined by the spin-dependent scattering at the interfaces of the multilayer, which depends on the relative orientation of the magnetizations of the ferromagnetic layers.[4] In Fe/Cr multilayers (Fig. 1.1 (a)), with no applied field, the magnetizations of adjacent ferromagnetic layers are aligned antiferromagnetically due to the interlayer coupling through the Cr spacer, leading to an increased scattering and thus to a higher resistance. Applying a sufficiently large external magnetic field, the

magnetizations are aligned and thus a low resistance state is reached due to the lower scattering at the interfaces. Nowadays, GMR values up to around 20% are obtained at room temperature in optimized spin-valve structures.[5] Spin-valve devices consist of two ferromagnetic layers separated by a non-magnetic spacer (lower panel in Fig. 1.1 (b)). Contrarily to GMR multilayers, the magnetization of one layer is fixed by the exchange bias with an antiferromagnet,[6] while the other is free to rotate with the external magnetic field.

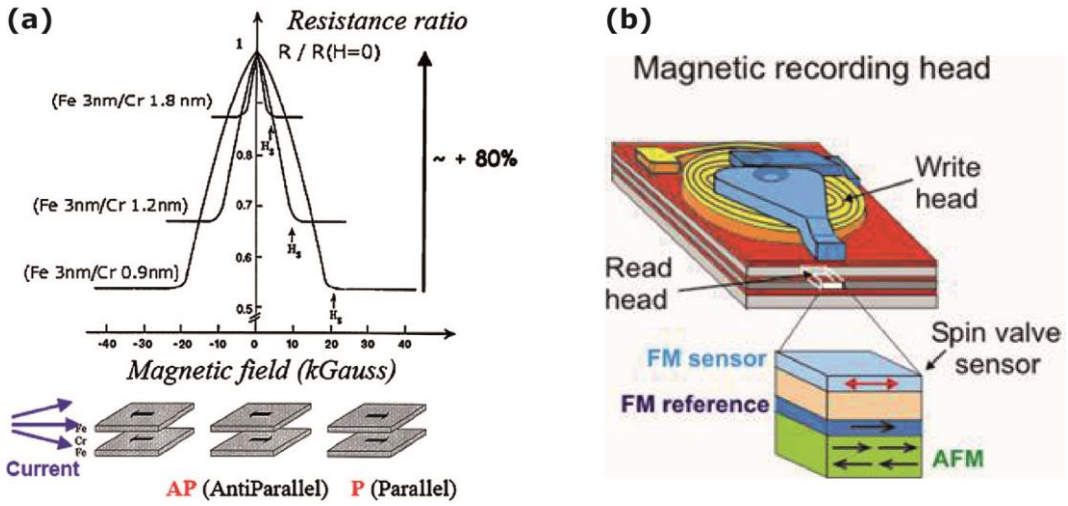

Fig. 1.1 (a) First observation of GMR effect in Fe/Cr multilayers at 4.2 K (from [3]). (b) Spin-valve structure as a magnetic field sensor in the read-head of magnetic hard drives.

The larger magnitude of GMR with respect to AMR and the fact that it allows a straightforward scalability due to its interfacial nature, opened up a wide range of applications and stimulated further investigation in the field of magnetoresistive phenomena. The most effective early application of GMR devices was as magnetic field sensors in the read-head of hard disks (Fig. 1.1 (b)) replacing AMR heads, which led to a substantial increase in the density of stored information.[7]

Tunneling Magnetoresistance (TMR) is observed in junctions consisting of two ferromagnetic electrodes separated by a thin insulating spacer, the magnetic tunneling junctions (MTJs). If the spacer is thin enough, upon the application of a potential difference across the junction an electric tunneling current is generated. Due to the spin-dependent tunneling effect (see section 2.1), the tunneling resistance of the junction depends on the relative orientation of the magnetizations of the two electrodes (Fig 1.2 (a)).

TMR was first discovered by Jullière in 1975,[9] however for more than a decade after Jullière first studies, TMR received little attention because it was not observed at room temperature. It attracted renewed attention after the discovery of GMR and its applications. In 1995, Moodera *et al.*[10] obtained TMR ratios as high as 18% at room temperature with amorphous aluminum oxide tunnel barriers and 3*d* ferromagnetic electrodes. Following the great impact of such a

high MR ratio, in the following years TMR was increased to about 70% by optimizing the ferromagnetic electrode materials and the conditions for fabricating the Al_2O_3 barrier.[11] For having higher TMR values, *half metal* electrodes (e.g. manganites such as $La_{0.67}Sr_{0.33}MnO_3$ (LSMO)), have been employed because of their 100% spin polarization, reaching TMR ratios up to 1800% at 4.2 K.[12] However, at higher temperatures half metallicity decreases rapidly, resulting in a drop of the magnetoresistance.

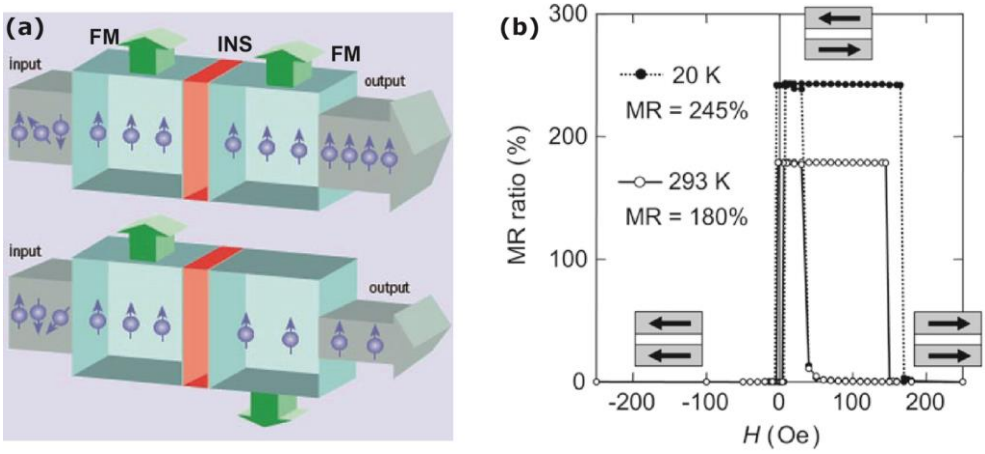

Fig 1.2 (a) Sketch of the spin-dependent tunneling transport in magnetic tunneling junctions. The resistance is low (high) when the magnetizations are parallel (antiparallel). (b) First observation of the giant TMR effect in epitaxial MgO-based magnetic tunneling junctions (from [8]).

The great boost in TMR technology was given in 2001 by Butler[13] and Mathon,[14] who predicted with first-principle calculations that epitaxial MTJs with a crystalline magnesium oxide (MgO) tunnel barrier would give rise to TMR ratios of over 1000%. In 2004 TMR ratios of about 220% were obtained at RT in sputtered MTJs with a crystalline MgO (100) barrier and amorphous CoFe electrodes.[15] TMR ratios up to 180% were reached in the same year in epitaxial MgO MTJs grown by molecular beam epitaxy (Fig 1.2 (b)).[16] This so-called *giant TMR effect* in MgO-based MTJs is enabled by the combination of coherent tunneling through the crystalline MgO barrier and spin-filtering effect of MgO, in contrast with the non-coherent tunneling across amorphous alumina barriers (see section 2.1.4).

As shown in Fig. 1.3, from the point of view of the spintronic applications, MgO-based MTJs have already been applied in HDDs read-heads and are promising candidates for building MRAMs (Magnetic Random Access Memory),[8] combining the short access time of the conventional semiconductor-based RAM and the non-volatile character of the magnetic memories.[7]

Recently, a magnetoresistive effect, namely the **Tunneling Anisotropic Magnetoresistance (TAMR),** has been discovered studying tunneling junctions comprising only one ferromagnetic electrode.[17] The first evidence of such effect was observed in (Ga,Mn)As/AlO_x/Ti junctions,

which showed a spin-valve like magnetoresistive signal despite the absence of a second ferromagnetic electrode. In such systems, the change in the tunneling resistance is due to anisotropy in the density of states of the only ferromagnet, induced by the spin-orbit coupling.[18] One of the reasons why TAMR is particularly promising in spintronics applications, is because it does not require coherent spin transfer across the junction; furthermore, as it will be discussed in depth in section 2.3, TAMR opens new possibilities in exploiting antiferromagnetic materials as active components in novel spintronic devices.

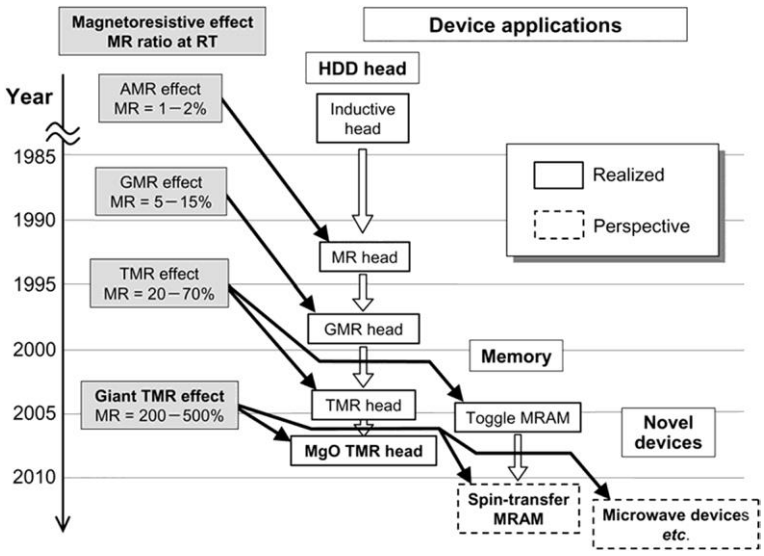

Fig. 1.3 History and technological impact of magnetoresistive effects at room temperature (from [8]).

In this framework, part of the thesis work (section 9) was devoted to the realization of tunneling junctions comprising an antiferromagnetic electrode and a non-magnetic electrode, with no ferromagnetic elements in the device. It was demonstrated that it is possible to store magnetic information in such junctions, performing a field-cooling across the Néel temperature of the antiferromagnet, exploiting the TAMR effect in the antiferromagnet. It can be envisioned the development of thermally-assisted MRAM devices exploiting this effect.

In the following section, an overview over the state of the art of biosensing technology in the framework of the development of compact lab-on-a-chip devices is given; in particular, the working principle and the features of magnetoresistive biosensing will be discussed.

1.2 Biosensors and lab-on-a-chip devices

Biosensors are devices which incorporate a biological sensing element in conjugation with physicochemical transducers for allowing further processing and delivery of the acquired information. The virtually unlimited potential applications of biosensing technologies, which

range from medical diagnostics, to defense, to food safety, to environmental control, have been estimated to be worth billions of U.S. dollars and are increasingly gathering attention both from industry and academia.[19] In particular, following the fast development of microfabrication techniques driven by the semiconductor industry since the 60s, and microfluidic technologies in the last decades, the interest towards easy-to-use, inexpensive portable devices for decentralized, *in situ* or home analysis grew stronger. A further evolution of this concept consists in the possibility to integrate a series of complex laboratory tasks other than biosensing, in a single compact device, the *lab-on-a-chip* (LOC).[20,21]

Despite the differences in the detection methods presented hereafter, the figures of merit which define the performance of biosensing platforms can be summarized as follows:

- *Sensitivity* is defined as the slope of the analytical calibration curve. An analytical method is sensitive when a small change in analyte concentration causes a large change in the response.
- *Selectivity*. A method is selective when the response of the analyte can be differentiated from every other response. High selectivity is needed for quantifying accurately an analyte in the presence of interferences, so that only the analyte of interest will contribute to the measure.
- *Limit of Detection (LOD)* is the concentration or the quantity derived from the smallest signal that can be detected with acceptable degree of certainty for a given analytical procedure. LOD can be used as a figure of merit that describes the ability of a biosensor to discriminate the signal from the noise level, thus defining the signal-to-noise ratio that is the distance between the analytical signal of the analyte and the instrumental noise.[22]
- *Dynamic range* is related to the range of concentrations of analyte which can be quantified by the sensor. The dynamic range is usually closely related to the sensitivity, and both must be carefully calibrated for matching the requirement of the specific assay.
- *Repeatabilty and reproducibility* refer to the closeness of the agreement between the results of successive measurements, carried out in the same (repeatability) or different (reproducibility) conditions related to operators, apparatus, laboratories and/or intervals of time between subsequent analyses.

1.2.1 Lab-on-a-Chip

Lab-on-a-chip devices are generally considered a subset of MEMS devices and often indicated by "Micro Total Analysis Systems" (μTAS) as well. They deal with the handling of extremely small fluid volumes down to less than pico-liters. The controlled motion of the fluids, the DNA amplification, drug screening and many others analytical technique have been miniaturized in

LOC platforms. Many of today's applications and possibilities of microfluidic lab-on-a-chip systems have been reviewed by Weigl et al.[23] and Dittrich et al.[24] Beyond basic research, nowadays a wide variety of LOC platforms were successfully introduced in the market, providing microfluidic-based point-of-care diagnostics for viral and bacterial infections, cardiovascular and kidney diseases, bipolar disorder etc.[25]

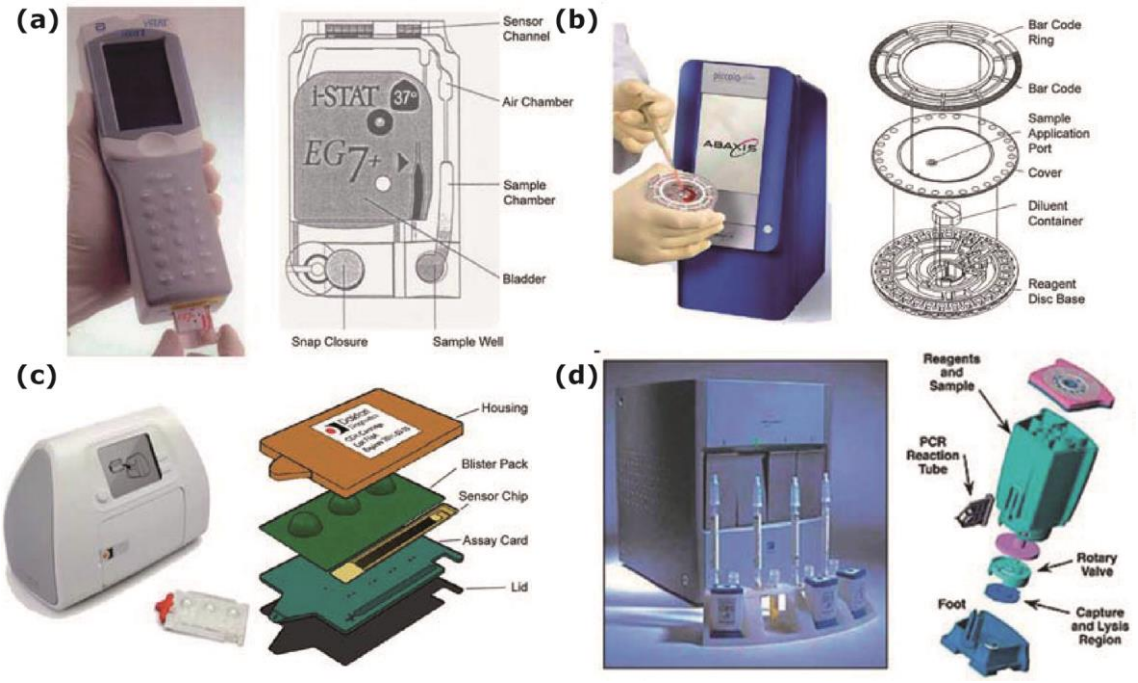

Fig. 1.4 Images and schemes of selected platforms for POC diagnostics. (a) and (b) i-STAT® and Abaxis® systems, respectively, for common blood tests. (c) Dakari® system for monitoring HIV disease. (d) Cepheid system®, for detection of DNA and RNA signatures. Adapted from [25].

The main advantages of miniaturization, which justify such a strong interest in LOC platforms, may be summarized as follows:

- Low fluid volume consumption, due to the use of microfluidics, leads to lower reagents costs, less waste and less required sample volumes in diagnostics.
- Better efficiency and faster analysis due to the short diffusion distances, fast heating, high surface to volume ratios and small heat capacities.
- Better reproducibility and process control due to the fast response of the system.
- The compactness of the system leads to the integration of many advanced features in a single device, allowing a high parallelization and thus high throughput analyses.
- Low fabrication costs, allowing cost-effective disposable chips and mass production.
- Possibility of integrating several functionalities into hand-held, easy-to-use portable devices allowing point-of-care (POC) diagnostics.

Fig. 1.4 illustrates the schematics of selected commercial LOC platforms for a variety of POC tests. Among these, a promising and explored application is in HIV testing through CD4 + T-cell counting. In this case, POC diagnostics is the highly favorable option due to the high prevalence of HIV in developing countries (Dakari Diagnostics® system in panel (c)). Other systems are designed to perform a broad menu of the most commonly performed diagnostic tests, including cardiac markers, blood gases, chemistries and electrolytes, lactate, coagulation, and hematology using disposable cartridges (i-STAT® System and Abaxis® systems in panel (a) and (b) respectively).

One of the most important fields, which gathered increasing attention due to the extensive improvements in genome sequencing of the last decades, is the detection of DNA and RNA signatures. LOC platforms for nucleic acid-based detection, other than in clinical diagnostics (Cepheid® system in panel (d)), find interesting applications also in the agrifood industry for the quantification of pathogens. In this context, an important part of the thesis work is focused on the development and optimization of a magnetoresistive biosensing platform for detecting DNA-DNA hybridization events, and towards the integration of such platform in a LOC device for the point-of care detection of *Hepatitis E* virus or *Listeria*.

1.2.2 DNA biosensing in lab-on-chip platforms

While DNA sequencing has become the technique of choice to address many different biological and diagnostic issues, it is inherently a slow technique requiring the use of bulk apparati, i.e. unsuitable for POC applications.

On the other hand, DNA biosensors are widely used due to their inherent physicochemical stability, specificity and suitability for performing multiplexed analysis. The most common working principle involves the detection of the highly specific hybridization events between single strand DNA (ssDNA) “probes”, immobilized on the surface of a transducer, and complementary ssDNA “target”, which is usually dispensed in solution on the surface of the sensor. The detection of the molecular recognition events can be direct (label-free), or by means of additional markers bound to the target molecules. The latter generally have the advantage of large signal-to-noise ratio, since markers generally possess properties which can be easily distinguished from the background. However, the use of markers requires an additional molecular recognition step, which can reduce the overall detection efficiency.

DNA microarrays combined with fluorescent detection (Fig. 1.5) are currently the most widespread technology for multiplexed DNA detection. They consist of an arrayed series of thousands of microscopic spots of probe DNA oligonucleotides, each containing a specific DNA sequence. The analyte is then brought in contact with the array and hybridization between complementary DNA strands takes place; the unbound molecules are then removed with a

washing step. Then, a fluorescent label functionalized with a probe molecule is injected, which binds to the now immobilized target analyte. This protocol is known as sandwich assay; alternatively, the fluorophore can be attached to the analyte itself and the last hybridization step can be omitted. The array is then scanned by a laser and imaged by a CCD camera, and the probe is identified by the coordinates of the fluorescent feature.

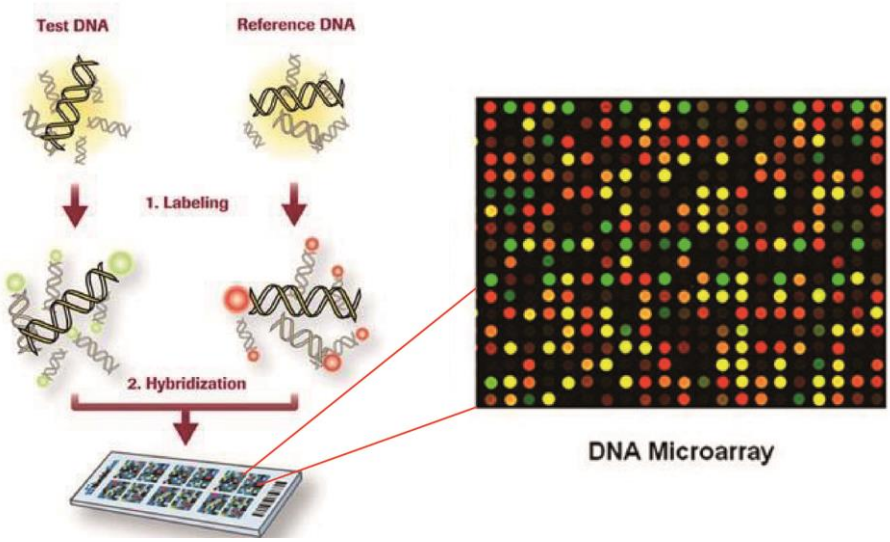

Fig. 1.5 Left panel: scheme of detection in DNA microarrays. Right panel: fluorescence image of a DNA microarray.

Currently, standard fluorescence-based detection systems and most of the hybridization-based detection systems heavily rely on DNA amplification techniques, such as Polymerase Chain Reaction (PCR), for enhancing the assay sensitivity and LOD. PCR is a biochemical technology in molecular biology to amplify a single or few copies of a piece of DNA across several orders of magnitude, generating thousands to millions of copies of a particular DNA sequence.[26] Despite the fact that PCR is a common and indispensable technique used in medical and biological research labs for a variety of applications, it is still a complex procedure which is unsuitable for point-of-care applications.

In the past decade, a wide variety of on-chip DNA biosensing techniques were investigated with the ultimate goal to reduce the LOD from the picomolar range of the current microarray technology, to the attomolar range, for enabling diagnostic assays with real, non-amplified biological samples.[27] Among these, electromechanical devices integrating microcantilevers[28] or quartz crystal microbalances[29] present LOD of 10^{-11} and 10^{-14} M, respectively. Other systems based on electrochemical detection methods are closer to the required sensitivity.[30,31] Magnetoresistive biosensors, which will be discussed in the next section, have demonstrated limit of detection in the zeptomolar range.[32] For a review on the recent advances in DNA-biosensing technology and comparison between the different techniques see [33].

1.2.3 Magnetoresistive biosensing

Magnetoresistive biosensing consists in using magnetic markers in combination with MR magnetic field sensors for detecting biomolecular recognition events. Following the first demonstration in 1998[34] driven by the development of GMR based magnetic field sensors in data storage, magnetoresistive biosensing was extensively investigated in the past decade, and devices based on AMR,[35–38] GMR,[32,39–42] and TMR were demonstrated,[43–45] reaching LOD in the femtomolar[26] and zeptomolar[32] range employing different detection methods and magnetic markers.

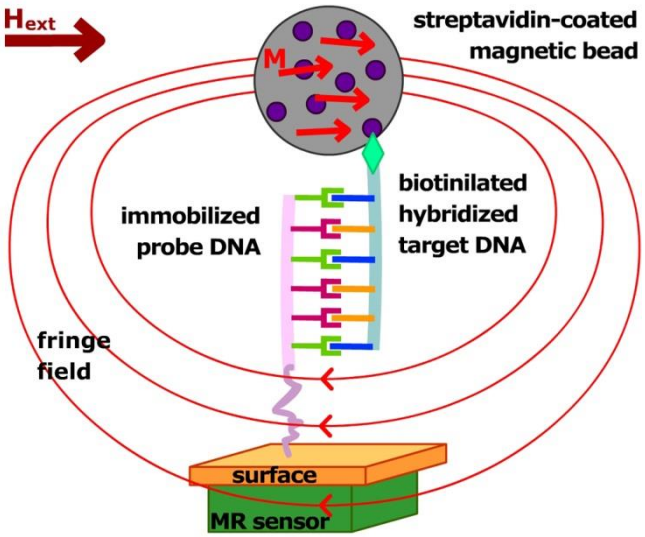

Fig. 1.6 Sketch of the detection of a DNA-DNA hybridization event with MR sensors in combination with magnetic markers.

Among the large family of MR sensors, GMR sensors based on spin-valves and TMR sensors based on MTJs provide the best results in terms of sensitivity and LOD. Between these two, the former are currently the most widespread because of the easier fabrication and integration in LOC devices, despite the latter provide the absolute best results in terms of detection of weaker magnetic fields.[46] Recent advances in magnetoresistive biosensing and comparisons on their performances are reviewed in [46,47].

Other than their extremely high sensitivity and LOD, and fast performance, magnetoresistive sensors have some advantages which make them ideal candidates for integration in LOC devices:

(i) the direct translation of magnetic signal into an electrical one through magnetoresistance makes them readily integrable with conventional electronic platforms;

(ii) their fabrication is based on well-established semiconductor processing techniques, allowing for low cost mass production and high scalability.

The magnetic labels employed are non-remanent superparamagnetic beads (see section 2.8) whose size can vary from a few microns in diameter to a few nanometers depending on the application and type of sensor.

(iii) The use of magnetic markers is particularly advantageous because usually all other components in the sample solution are non-magnetic, thus eliminating interference effects and minimizing the background signal;

(iv) their magnetic properties are stable over time (in contrast with fluorescent labels which are affected by bleaching and quenching effects) and their surface is easily functionalized with suitable receptors, which simplifies specific binding to desired biomolecules;

(v) the possibility to apply local forces on the markers by generating magnetic gradient fields or exploiting a controlled domain wall motion in magnetic nanostructures,[36,39,48,49] opens up the interesting option of manipulating molecules through the motion of their labels.

The most common detection scheme in DNA magnetoresistive biosensors is very similar to the fluorescence-based microarrays (Fig. 1.6).

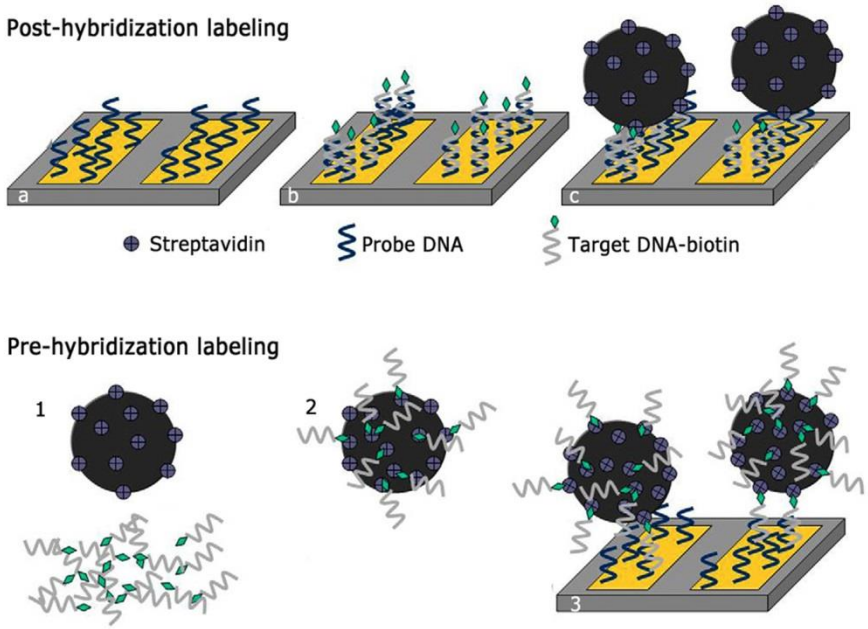

Fig. 1.7 *Post-hybridization* versus *pre-hybridization* labeling of biotinylated target DNA with streptavidin coated magnetic nanoparticles. Adapted from [26].

The probe molecule (e.g. probe ssDNA) is immobilized on the surface of the magnetoresistive sensors, then the target molecules (e.g. complementary ssDNA) in solution are dispensed on the sensors and hybridization occurs. A washing step then removes the non-hybridized molecules. The magnetic labeling can be performed before (*pre-hybridization*) or after (*post-hybridization*) the hybridization step (Fig. 1.7), where the former has usually been found to be less effective in terms of lower concentration of immobilized biomolecules, because the steric hindrance of the magnetic beads reduces the efficiency of the hybridization reaction.[26]

For measuring, an external magnetic field is applied in order to align the magnetic moments in the magnetic markers and produce a detectable fringe field on the sensor. The sensitivity and LOD of the assay are influenced by a multitude of factors, other than the absolute sensor performances. In the framework of this thesis, the maximization of the sensor sensitivity in MTJ-based sensors is extensively investigated in terms of measurement configuration and spatial distribution of the immobilized probes in sections 5 and 6, respectively.

1.3 Outlook of the thesis

The work presented in this thesis started as a continuation of my master thesis work, which I carried out in the Spin Electronics group at the L-NESS laboratory of Politecnico di Milano in Como, Italy under the supervision of Prof. R. Bertacco. The beginning of my master thesis coincided with the purchase of the AJA ATC Orion sputtering system which was also used in this work for fabricating the MTJ based sensors. The primary goal was to optimize the sputtering deposition of the single layers and to characterize and optimize the magnetic properties of functional magnetic multilayers (such as exchange biased bilayers and synthetic antiferromagnet structures) with the aim to employ them for the fabrication of MTJ sensors. By the end of the thesis, the first MTJ-based sensors were successfully microfabricated by optical lithography and characterized.

The first part of my work was carried out between the L-NESS laboratory, in Prof. Bertacco's group, and the Istituto di Chimica e Riconoscimento Molecolare (ICRM-CNR), in Milan, in Dr. Marcella Chiari's group, who partly funded my Ph.D. studies in the framework of SPINBIOMED project from Fondazione Cariplo aiming to the realization of an MTJ-based biosensing platform with LOD in the picomolar range. Part of my studies were also funded in the framework of LOCSENS project from Regione Lombardia under the supervision of Prof. Bertacco. At the end of the first year I was awarded with a 2 year additional Ph.D. scholarship from Scuola Interpolitecnica which allowed me to spend a 9 month period at the Georgia Institute of Technology, Atlanta GA, U.S. in prof. Elisa Riedo's group.

Since the beginning, my research activity followed two directions. The first one was focused on the realization and optimization of an MTJ-based biosensing platform for detecting DNA-DNA hybridization events and, later on, aiming to the study of the activity of neural cells in vitro; the latter towards the realization of novel spintronic devices based on non-conventional magnetic tunneling junctions where the electrical transport is governed by antiferromagnetic materials. The former studies were carried out in collaboration with Dr. Chiari (ICRM-CNR, Milan, Italy), and later with Prof. Riedo (Georgia Institute of Technology, Atlanta GA, U.S.) and the latter with Dr. Marti and Prof. Jungwirth (Institute of Physics ASCR, Praha, Czech Republic).

The first part of my studies on MTJ-based sensing platforms started from the preliminary results on the fabrication of MTJs of my master thesis, and focused on the optimization of the devices performances in terms of reduced hysteresis and linearity of the sensor characteristics and high TMR values, combining an optimization of the sputtering deposition, annealing process and junction geometry. In the following months, a microfluidic system and an electronic platform based on multiplexing and double modulation technique were designed and integrated with the MTJ-sensor arrays. The preliminary experiments on the detection of magnetic bead sedimentation allowed us to develop a model for maximizing the sensor sensitivity to the magnetic beads selecting the optimal working point on the sensor characteristics. Meanwhile, following this model, we performed biomolecular recognition experiments with synthetic DNA. Since the sensitivity of the experiments depends on the spatial distribution of the magnetic beads in the vicinity of the sensor, we developed a method based on optical lithography for biopatterning the sensor area, which proved effective in increasing significantly the binding signal with respect to conventionally functionalized sensors. The following work on MTJs was focused on the design of a new sensor layout for an integrated LOC platform for the detection of pathogens in the agrifood industry (LOCSENS project). Furthermore, the detection of natural *Hepatitis E* virus DNA was demonstrated with our platform. The last part of my work on biosensing was carried out with the aim of using our MTJ sensors for detecting the neural activity in vitro. For maximizing the sensitivity, it is fundamental to have a control over the growth and orientation of neurons with respect to the MTJ sensors. With this goal, my research activity at the Georgia Institute of Technology, Atlanta, was focused on developing a technique based on thermochemical nanolithography for patterning gradients of extracellular matrix proteins and control the growth of neurons on the surface of the sensors.

The second research line, regarding antiferromagnet (AF)-based spintronics, consisted in the realization and study of sputtered tunneling junctions comprising an AF electrode and a non-magnetic electrode, with no ferromagnetic materials. The goal was to exploit the TAMR effect in the antiferromagnet for demonstrating the feasibility of antiferromagnetic-only spintronic devices. With this purpose, field cooling experiments, where the resistance of the junction was

recorded as a function of the temperature for different orientations of the applied magnetic field, were performed. It was shown that it is possible to set different metastable states characterized by two different electrical resistances by performing a field cooling with different directions of the applied magnetic field. This demonstrated the possibility to store magnetic information in an antiferromagnet-only based spintronic device.

The thesis comprises 10 chapters, and covers most of the work I carried out in my doctoral studies. Below, the outline of each chapter is given:

1. **Introduction**. The motivation, context and organization of the work are presented.
2. **Theory.** In this chapter, the physical phenomena exploited in MTJ-based sensors and TAMR devices are reviewed, presenting theoretical and experimental studies.
3. **Experimental Techniques.** The working principles of the thin film deposition, micro-nano fabrication, and characterization techniques employed in this experimental work are hereby presented.
4. **Realization of an MTJ-based magnetic biosensing setup.** In this chapter, the work which led to the realization of the magnetoresistive biosensing platform is presented. Starting from the optimization of the sputtering deposition, to the characterization of the functional magnetic layers, to the final integration of the sensor array with microfluidics and electronics. The sensor characteristic is optimized in terms of TMR value, low coercivity and linearity, and a statistical analysis of the microfabrication yield is given.
5. **Conditions for efficient bead detection in magnetoresistive sensors.** This chapter presents the results on the work on the optimization of the sensitivity of the MTJ sensing platform to magnetic beads. A model for maximizing the sensitivity by selecting the optimal working point on the sensor characteristic is developed. Experiments of bead sedimentation were performed for confirming the validity of the proposed approach.
6. **Photolithographic biopatterning of MTJ-based biosensors for molecular recognition.** Here, the development of a novel technique based on optical lithography for biopatterning the sensor area with probe ssDNA molecules is presented. The effectiveness of the technique in enhancing the magnetic signal in biological experiments is demonstrated by means of calculations and experiments of detection of hybridization events.
7. **Towards a Lab-on-chip platform for detecting DNA pathogens.** In this chapter, the early results of the ongoing work aiming to the integration of our biosensing platform in a LOC device for detecting pathogens in the agrifood industry are presented. The detection of natural *Hepatitis E* virus DNA using our conventional platform is demonstrated. Furthermore, the design of the single components of the LOC platform and preliminary results of bead detection using integrated electronics are presented.

8. **Thermochemical nanolithography of protein gradients for neuronal guidance.** Here, we present the studies on the patterning of nano and micron-sized gradients of extracellular matrix proteins using thermochemical nanolithography. This work, still in progress, aims to the fine control of the growth and positioning of neurons on the surface of MTJ sensor arrays for enabling the study of neural activity *in-vitro*, exploiting the high resolution and sensitivity which MTJ sensors can provide.
9. **Storing magnetic information in IrMn/MgO/Ta tunnel junctions via field cooling.** Here, the fabrication and characterization of IrMn/MgO/Ta tunnel junctions by magnetron sputtering is presented. The details and results on the field cooling experiments which demonstrated the possibility to tune the junction resistance in a non-volatile way exploiting the TAMR effect, are shown.
10. **Conclusion and perspectives.** This conclusive chapter summarizes the results of the experimental work presented in this thesis and provides some outlooks for further development of such research lines.

2. Theory

In this section, an overview on the physical effects related to MTJ-based biosensors and antiferromagnet-based tunneling devices is given. Some of the key experimental works which allowed the demonstration of the proposed theoretical models are reviewed.

2.1 Tunneling magnetoresistance theory

2.1.1 Tunneling conductance in a Metal/Insulator/Metal system

Let us consider the electron tunneling process between two metallic electrodes through an insulating barrier. We will treat the case of an ideal junction with a bias voltage *V* applied across, in order to study the tunneling conductance dependence on the system parameters.

As shown in Fig. 2.1 (a), the Fermi levels of the two metal electrodes lay inside the insulator bandgap. This creates an approximately rectangular potential barrier whose height is set by the minimum of the insulator conduction band. When no voltage is applied across the junction, the system is in thermodynamic equilibrium and the Fermi levels of the two metal electrodes coincide.

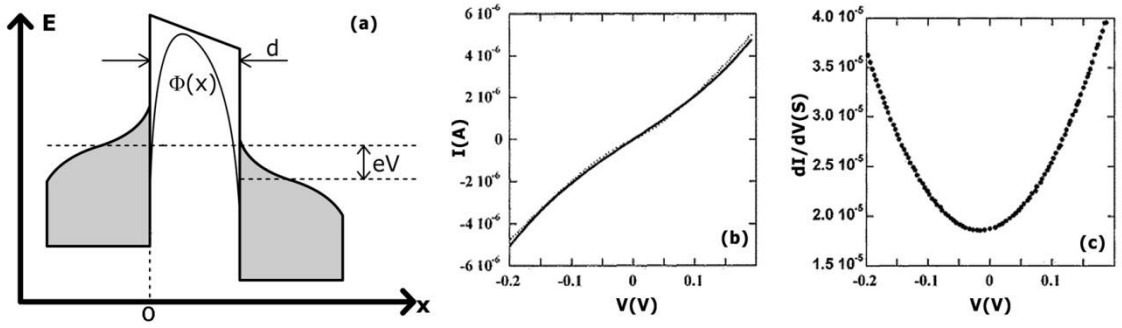

Fig. 2.1 In (a), bandstructure for a MIM junction biased with a potential *V*. In (b), *I*:*V* characteristic at *T* = 13 K for a tunnel junction of the type CrO_2/barrier/Co fitted to the Simmons model (solid black line) (from [50]). In (c), d*I*/d*V* versus *V* for the same junction (from [50]).

This leads to no net current flowing across the junction because the energy levels on both sides of the barrier are filled. Applying a voltage *V* changes slightly the barrier shape and splits the two Fermi levels of a quantity *eV*, where *e* is the electronic charge. This brings some empty levels in correspondence with the filled ones on the other side of the barrier, allowing a net

tunneling current flowing from the negatively charged electrode. The net current is the difference between the tunneling currents in the two directions:

$$j = j_{l\to r} - j_{r\to l} \tag{2.1}$$

Each one of the two contributions depends on the density of states in the two electrodes, on the tunneling probability, and on the occupancy of the metal energy levels described by the Fermi distribution. Thus, the expression for the total tunneling current is:

$$j = \frac{e}{2\pi\hbar}\sum_k \int dE\rho_r(E)\rho_l(E+eV)|M(E)|^2[f(E)-f(E+eV)] \tag{2.2}$$

Where the sum is performed on the transversal components of the wavevector (i.e. k_x and k_y), $\rho(E)$ is the density of states, $f(E)$ is the Fermi distribution and $|M(E)|^2$ is the matrix element which is proportional to the tunneling probability $|T(E)|^2$ calculated using the WKB method, i.e. approximating the arbitrarily shaped barrier with a series of infinitesimally thick rectangular barriers:[51]

$$|T(E)|^2 \approx \exp\left\{-\frac{2}{\hbar}\int_0^d \sqrt{2m[\Phi(\tau)-E]}d\tau\right\} \tag{2.3}$$

Where Φ is a potential barrier of arbitrary shape and m is the electron mass.

The problem of evaluating the general formula, Eq. (2.2), has been tackled by several different simplified models.[52,53] In the work of Simmons,[54] an analytical expression for the dependence of j on the applied voltage V was derived. The model assumes T = 0 K, approximating the Fermi distribution with step functions; furthermore, it considers a potential barrier of arbitrary shape $\Phi(x)$ and average height $\bar{\Phi}$, and it employs free-electron relations for the density of states. The $j(V)$ characteristic is linear for $V \ll \Phi$, but becomes cubic ($j \propto \alpha V + \beta V^3$) for slightly higher potentials, leading to a parabolic conductance $\partial j/\partial V$ (Fig. 2.1 (b) and (c)). Furthermore, the exponential dependence of the current on the barrier height and on the square root of the barrier width is conserved. However, the application of a free electron model leads to a cancellation of the density of states (DOS) of the two electrodes in the expression for the tunneling current. If this were true, there could be no TMR effect. In order to accurately calculate the tunneling current, more sophisticated models have to be applied.

2.1.2 Jullière model for TMR

In ferromagnetic conductors, the *spin-splitting* of the bandstructure leads to separate spin-up and spin-down density of states. This phenomenon can be exploited in junctions with ferromagnetic electrodes for having a spin-dependent tunneling conductance. The first experiments on similar systems were performed by Meservey e Tedrow at the beginning of the

'70s.[55] They studied Al/Al_2O_3/ferromagnet type junctions, observing a spin-dependent tunneling effect from a ferromagnetic electrode to a superconducting one.

The first phenomenological interpretation to the tunneling magnetoresistance was given by Jullière in 1975.[9] Fig. 2.2 shows Jullière's original result on a junction with iron and cobalt electrodes separated by an oxidized amorphous germanium layer.

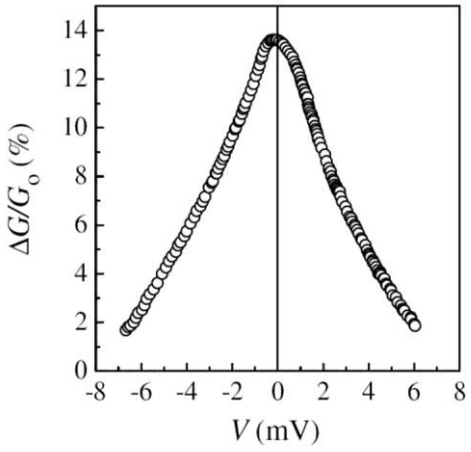

Fig. 2.2 Conductance variation depending on the applied voltage in a Fe/Ge/Co junction at T = 4.2 K. From [9].

In this model, Jullière assumes that the spin is conserved in the tunneling process, therefore spin up and spin down (with respect to the magnetization of the ferromagnet) electrons carry the current in parallel in two independent channels. Thus Eq. (2.1) can be rewritten as:

$$j = j_{l\to r}^{\uparrow} + j_{l\to r}^{\downarrow} - j_{r\to l}^{\uparrow} - j_{r\to l}^{\downarrow} \tag{2.4}$$

In the simplest case for T = 0 K, the only electrons able to cross the barrier are those whose energy ranges between $E_F - eV$ and E_F (Fig. 2.1 (a)). For sufficiently small bias voltages V, the DOS $\rho(E)$ and the tunneling matrix element $|M(E)|^2$ can be approximated as constant over this energy range, with their values replaced by those at the Fermi energy. Thus, from Eq. (2.4), one retrieves that the conductance is a sum of two terms corresponding to the two independent spin channels, each one proportional to the DOS product. For the two extreme cases of parallel (*P*) and antiparallel (*AP*) alignment of the electrodes' magnetization vectors:

$$\begin{cases} G_P = G_{\uparrow\uparrow} + G_{\downarrow\downarrow} \propto (\rho_{l\uparrow}\rho_{r\uparrow} + \rho_{l\downarrow}\rho_{r\downarrow})|M|^2 \\ G_{AP} = G_{\uparrow\downarrow} + G_{\downarrow\uparrow} \propto (\rho_{l\uparrow}\rho_{r\downarrow} + \rho_{l\downarrow}\rho_{r\uparrow})|M|^2 \end{cases} \tag{2.5}$$

Where $\rho_{l\uparrow(\downarrow)}$ and $\rho_{r\uparrow(\downarrow)}$ are the density of states of the two FM electrodes at the Fermi level. The tunneling matrix element is assumed to be identical for both spin orientations and thus do not bring any difference in the conductances.

Following this, let us define the TMR ratio:

$$TMR = \frac{R_{AP} - R_P}{R_P} = \frac{G_P - G_{AP}}{G_{AP}} = \frac{2P_1P_2}{1 - P_1P_2} \tag{2.6}$$

where P_i is the *effective spin-polarization* for the electrode *i*, which is a measure of the spin-polarization related to the tunneling phenomena through a specific barrier.

From Eq. (2.5) we can write the expression for the effective spin-polarization in Jullière's model:

$$P_i = \frac{\rho_{i\uparrow} - \rho_{i\downarrow}}{\rho_{i\uparrow} + \rho_{i\downarrow}} \tag{2.7}$$

It is worth noting that, in Jullière's model, *P* coincides with the spin-polarization of the DOS of the ferromagnets at the Fermi level.

Jullière's model is widely used for describing spin-dependent tunneling systems, but fails in many ferromagnet/insulator/ferromagnet junctions because, as we already pointed out, some phenomena are still to be included in the physical model of the device, particularly concerning the junction barrier interface and insulator properties.

2.1.3 Effective spin polarization

As suggested in Eq. (2.6), depending on the effective spin polarization *P* of the two electrodes, the magnetoresistance can be *normal* or *inverse*; in the former case the polarization of the two ferromagnets has the same sign, thus the resistance of the antiparallel configuration is the highest; in the latter case, the polarizations have opposite sign, resulting in a higher resistance of the parallel configuration. In either cases, the total junction resistance can be pictured as the parallel of the resistances of the two independent spin channels, as shown in Fig. 2.3 (a) and (b) in the case of *normal* TMR. In the conductive configuration (a) one channel has much lower resistance than the other, shortening the circuit.

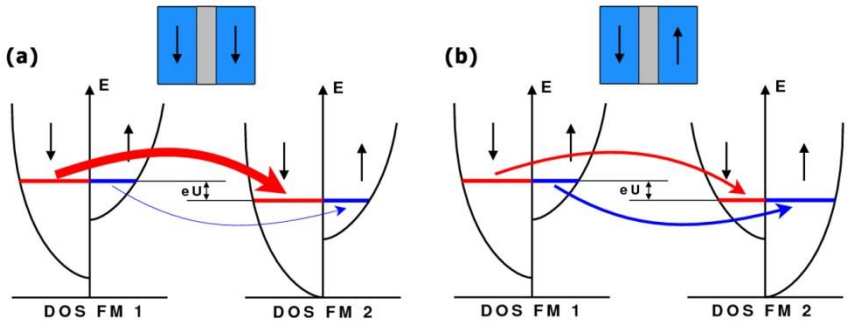

Fig. 2.3 Schematic representation of normal TMR process. (a) and (b) are the low and high resistance configurations, respectively.

As we have already pointed out, the effective spin polarization is influenced by several factors. Among these, the relation between the DOS and the tunneling matrix element $|M|^2$ plays a major role. In fact, the tunneling probability is different for states with different symmetry; this means that certain part of the total density of states is selected, depending on the barrier material and thickness. A remarkable example of this phenomenon involves the 3*d* ferromagnetic metals studied by Mersevey and Tedrow (i.e. Co and Ni).[55]

They observed that in such materials the *effective polarization* is positive, despite they have a negative polarization of the *d*-band DOS at the Fermi level (i.e. their majoritary *d*-band lays below the Fermi level). This apparent contradiction is explained considering that *s* and *d* states have different tunnel probabilities. In fact, due to their reduced effective mass, the *s* states, which have a positive polarization of the DOS at E_F, dominate the tunneling process, while the *d* states decay rapidly into the barrier. As a result, for thick enough barriers, the *effective spin polarization* is positive, and so the TMR, despite the *d*-band polarization at the Fermi level is negative.

2.1.4 Coherent tunneling transport across MgO barriers

Tunneling in a MTJ with an amorphous barrier is illustrated schematically in Fig. 2.4 (a), where the top electrode layer is Fe(0 0 1) as an example of a 3*d* ferromagnet. Various Bloch states of different symmetries exist in the top electrode. Because of the amorphicity of the tunnel barrier, there is no crystallographic symmetry in the tunnel barrier; thus all the Bloch states, regardless of their symmetry, can couple with evanescent states in the barrier and therefore have finite tunneling probability. This tunneling process can be regarded as a *totally incoherent tunneling*, and it is well described by Jullière's model, which assumes, as we have seen before, that tunneling probabilities are equal for all the Bloch states in the electrodes.

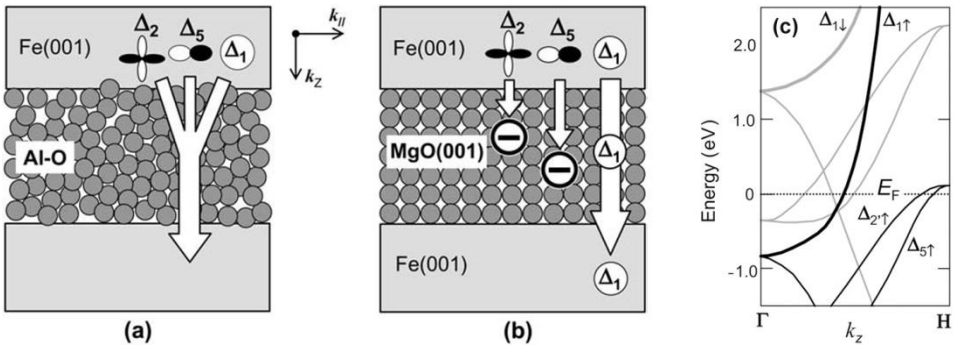

Fig. 2.4 Schematic illustrations of electron tunneling through (a) an amorphous Al-O barrier and (b) a crystalline MgO(0 0 1) barrier. (c) Band dispersion of bcc Fe in the $k_{\parallel} = 0$ (Γ–H) direction. From [56].

In 3*d* ferromagnetic metals and alloys, Bloch states with Δ_1 symmetry (*spd* hybridized states) usually have a large positive spin polarization (*SP* > 0) at E_F, whereas Bloch states with Δ_2

symmetry (*d* states) often have a negative spin polarization (SP < 0) at E_F. Therefore, since Bloch states of both symmetries can tunnel, the *net* effective spin polarization of the tunneling electrons will be reduced together with the TMR value.

It is worth noting that even for alumina barriers the assumption of totally incoherent tunneling is not valid, therefore the actual tunneling process is considered to be an intermediate process between the completely incoherent tunneling represented by Jullière's model and the coherent tunneling. If only the highly spin-polarized Δ_1 states coherently tunnel through a barrier (Fig. 2.4 (b)), a very high effective spin polarization of tunneling current and thus a very high TMR ratio are expected.

Such an ideal coherent tunneling is theoretically expected in epitaxial Fe(0 0 1)/MgO(0 0 1)/Fe(0 0 1) MTJs and is illustrated schematically in Fig. 2.4 (b). For the $k_{\parallel} = 0$ direction, in which the tunneling probability is the highest, the evanescent states in the band gap of MgO present three different symmetries: Δ_1, Δ_5 and Δ_2 (Fig. 2.4 (c)). When the symmetries of tunneling wave functions are conserved, the Bloch states couple with evanescent states of selected symmetry; e.g. Fe Δ_1 Bloch states couple with MgO Δ_1 evanescent states.

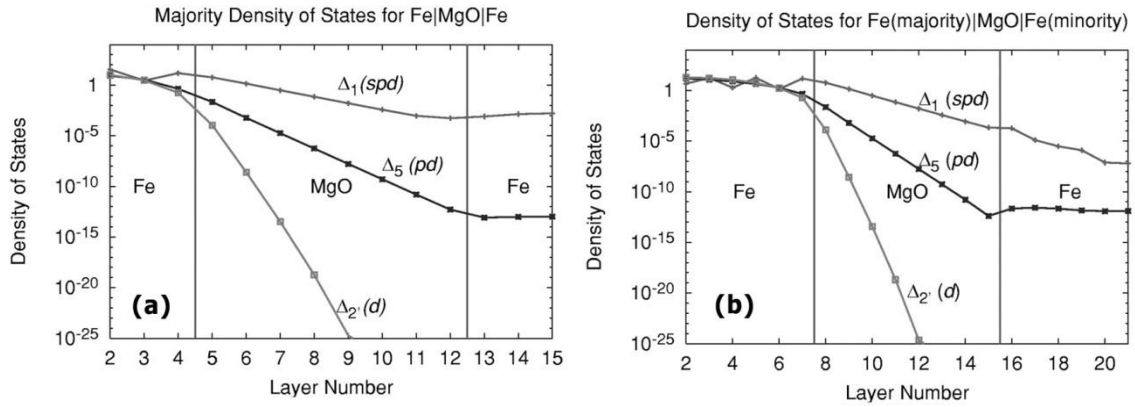

Fig. 2.5 (a) Tunneling DOS of majority-spin states for $k_{\parallel} = 0$ in Fe(001)/MgO (8 monolayers)/Fe(001) with parallel magnetic state. (b) Tunneling DOS for majority spins tunneling from the left Fe electrode in case of antiparallel alignment for $k_{\parallel} = 0$ in Fe(001)/MgO 8 monolayers)/Fe(001). From [13].

Since the MgO evanescent states decay with different rates depending on their symmetry, also the tunneling probability of the coupled Bloch states will be different. Fig. 2.5 (a) shows the partial DOS (obtained by first-principle calculations) for the decaying evanescent states in a MgO barrier layer in the case of parallel magnetic alignment.[13] Among these states, the Δ_1 evanescent states are those presenting the slowest decay, thus the dominant conductive channel is represented by the Δ_1 states, which in Fe, at the Fermi level, are present only for majority spin electrons. In the antiparallel configuration (Fig. 2.5 (b)) the resistivity is higher; indeed the majority electrons of the left ferromagnet will couple with the Δ_1 evanescent states

of MgO, but in the second electrode they will not find the same symmetry of the minority state, and thus they will be reflected. The conduction channel will be therefore represented by Δ_5 majority states, which can be coupled with the state of the second ferromagnet but decay faster in MgO. The states with different symmetry (Δ_2, Δ_2') decay very rapidly and do not contribute to conduction. This is the so-called *spin-filtering* effect of the MgO barrier that leads to predicted TMR ratios up to 1000%.

It is worth noting that highly spin-polarized Δ_1 Bloch states are present not only in bcc Fe (0 0 1) but also in many others bcc ferromagnetic metals and alloys based on Fe and Co. For example, in Co layers, only the Δ_1 states exist at E_F in the majority-spin band, because the other majority-spin band branches Δ_2 and Δ_5 are located below E_F, thus resulting in a higher TMR in Co-based MTJ.[57]

2.2 Sputtered CoFeB/MgO/CoFeB MTJs

Among all the Fe and Co alloys used as electrodes in sputtered MTJs, CoFeB/MgO/CoFeB junctions are the most widely used system, with the highest TMR ratio at room temperature.[58,59] In such systems, thermal annealing has proven to be one of the most crucial steps to achieve high TMR ratios, since it is during the post-annealing process that the TMR increases up to a few hundred percent, from typically 20–40 % in the as-deposited state.

Boron ensures that deposited CoFeB layers are amorphous; this implies reduced interface roughness and, most importantly, allows the sputtered MgO barrier to have a strong (001) texture as-deposited. During the post-growth thermal annealing (a.k.a. *solid state epitaxy* process), the top and bottom interfaces of the highly (001)-oriented MgO layer serve as templates for the crystallization of amorphous CoFeB layers in the (001) orientation, thus forming the epitaxial CoFeB(001)/MgO(001)/CoFeB(001) structure which enables the coherent tunneling process.[56,60]

Fig. 2.6 shows the dependence of the resistance per area product (a) and of the TMR ratio (b) as a function of the MgO barrier thickness, for different post-growth annealing temperatures. The tunneling resistance increases exponentially with respect to the barrier thickness, which is a result we expect according to the general calculations about tunneling phenomena in chapter 2.1.1.

The dependence of the TMR value on barrier thickness for different annealing temperatures is shown in Fig. 2.6 (b). In the ranges from 1.35 to 2.2 nm, the TMR ratio increases dramatically with increasing annealing temperature. This is due to the better crystalline quality of the structures achieved with higher annealing temperature. The fact that for thin enough barriers, TMR generally increases for thicker barriers can be explained by the fact that for thicker

barriers the contribution of spurious conducting channels (e.g. interface resonant states) decreases, leaving the coherent process as the only tunneling channel.

Fig. 2.6 (c) shows the *I*–*V* curves in the parallel configuration indicates virtually ohmic transport, while the anti-parallel configuration shows typical non-linear tunnel characteristic; the *I*–*V* characteristic in the parallel configuration may be due to the matching of the symmetry of the tunneling electronic states predicted by theoretical studies.[61,13]

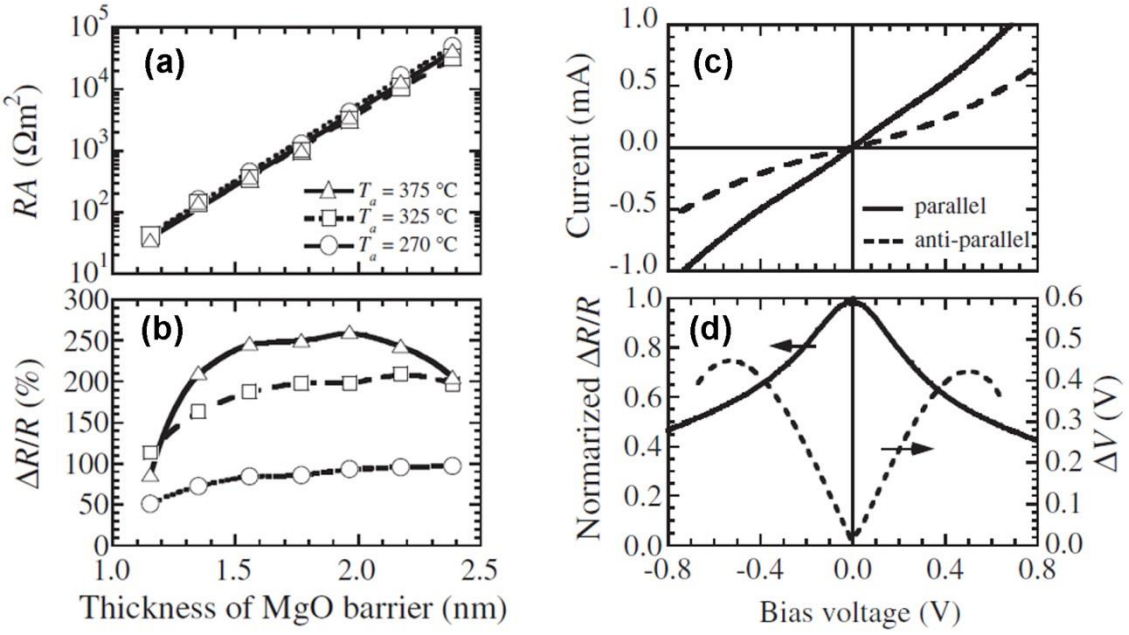

Fig. 2.6 (a) RA and (b) ΔR/R at room temperature as functions of thickness of MgO barrier. Dotted, dashed, and solid lines show data for MTJs annealed at 270, 325, and 375° C. (c) I-V curves of MTJs in parallel (solid line) and in anti-parallel configuration (dashed line). (d) Normalized TMR ratio (solid line) and output voltage ΔV (dashed line), as functions of bias voltage. Adapted from [61].

The dependence of the TMR ratio on the junction voltage (Fig. 2.6 (d)) i.e. the fact that the TMR decreases monotonically by increasing the voltage, is common to many TMR processes, One of the main causes of such effect can be identified in the spin-flip scattering by interface magnons. Let us consider an electron at the Fermi level in one ferromagnet tunneling towards the other ferromagnet; due to the presence of an applied voltage *V*, it will have an excess of energy *eV* with respect to the Fermi level of the second electrode. This ”hot electron” can decay reversing its spin and transferring its energy excess to a collective excitation of local spins (i.e. a magnon) at the interface between the insulating barrier and the magnetic electrode. This results in a reduction of the resistance due to the opening of new conductive channels and in a decrease of the TMR in the junctions.[62]

2.3 Tunneling anisotropic magnetoresistance (TAMR) for antiferromagnetic spintronics

Tunneling anisotropic magnetoresistance (TAMR) was identified for the first time in 2004 by Gould et al.[18] in a structure consisting of a normal metal – insulator – ferromagnetic semiconductor tunneling device. The authors reported a spin-valve like tunnel magnetoresistance signal in such junctions, which comprise only one ferromagnetic layer. The origin of such a behavior comes from the strong spin-orbit coupling in the single ferromagnetic layer rather than from the injection and detection of a spin polarized current by two coupled ferromagnets.

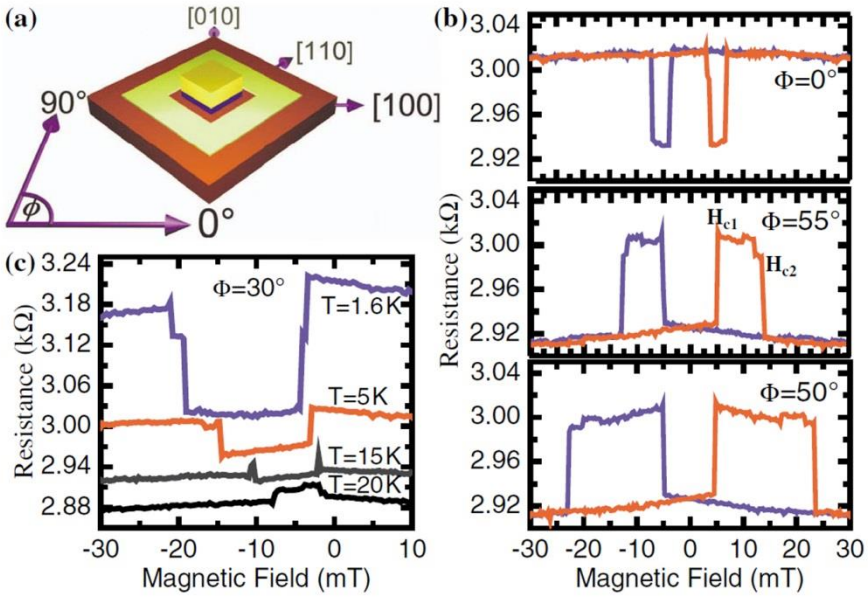

Fig. 2.7 Device schematic showing the contact geometry and the crystallographic directions. (b) Hysteretic magnetoresistance curves acquired at 4.2 K with 1 mV bias by sweeping the magnetic field along various directions. Spin-valve-like features of varying widths and signs are clearly visible, delimited by two switching events labeled H_{c1} and H_{c2}. The magnetoresistance is independent of the bias direction or amplitudes up to 1 meV. (c) TAMR along 30° for temperatures from 1.6 to 20 K, showing a change of sign of the signal. The curves are vertically offset for clarity. From [18].

Fig. 2.7 presents representative magnetoresistance curves at various angles measured in a (Ga,Mn)As/AlO_x/Ti tunneling junction. For each curve, the field is swept from negative saturation to positive saturation and back, but the plot focuses on the interesting region from --30 to +30 mT. In all cases, the magnetoresistance shows spin-valve-like behavior with an amplitude of ~3% delimited by two switching events (labeled H_{c1} and H_{c2} in the figure) between which the resistance of the sample is different from its value outside these events. However, the width and even the sign of the TAMR feature depend on ϕ. Noteworthy, despite

the feature changing signs as a function of ϕ, the device has only two distinct resistance states: a low one of ~2920 Ω and a high one of ~3000 Ω.[18]

Analyzing the device behavior of the angle ϕ and field intensity *H* the authors show that the sample is in a high-resistance state when *M* lies along the $[100]$ or $[\bar{1}00]$ crystallographic direction, and a lower resistance when *M* lies along the $[010]$ or $[0\bar{1}0]$. They provide an interpretation of the measured spin-valve-like effect as a tunneling anisotropic magnetoresistance (TAMR) due to a two-step magnetization reversal and a magnetization dependent density of states (DOS) in the (Ga,Mn)As layer.

A theoretical analysis was performed, illustrating that anisotropies in the (Ga,Mn)As DOS with respect to the magnetization orientation are large enough to explain the observation of the TAMR effect (details in Ref [18]).

TAMR effect is particularly appealing in spintronics applications, because it relaxes the requirement for coherent spin-transport through the barrier and furthermore, avoiding the second ferromagnetic layer may have fundamental consequences for the operation at high temperatures as it eliminates the need for a buried ferromagnetic layer which cannot be effectively treated by post-growth annealing.[63]

Recently, Shick *et al*.[64], suggested that in antiferromagnetic bimetallic compounds such as IrMn, the TAMR effect should be maximized. In fact, in transition metal ferromagnets a generic principle has been outlined, based on studies of magneto-crystalline anisotropies and of the TAMR and CBAMR (Coulomb blockade AMR)[65–67]: the magnetic anisotropy phenomena are maximized in bimetallic systems combining large spontaneous moments on the *3d* shell of a transition metal and large magnetic susceptibility and SOC on the *5d*-shell of a noble metal. Since Mn carries the largest moment among transition metals and most of the bimetallic alloys containing Mn order antiferromagnetically, strong magnetic anisotropy phenomena and AFM spintronics merge naturally together.[64]

The first spintronic device whose electrical transport was governed by an antiferromagnet was demonstrated by Park *et. al* in 2011.[68] The authors reported more than 100% spin-valve-like signal in a NiFe/IrMn/MgO/Pt stack with an antiferromagnet on one side and a non-magnetic metal on the other side of the tunnel barrier. Ferromagnetic moments in NiFe are reversed by external fields of approximately 50 mT or less, and the exchange-spring effect[69] of NiFe on IrMn induces rotation of antiferromagnetic moments in IrMn, which is detected by the measured tunneling anisotropic magnetoresistance (see section 9).

2.4 Exchange Bias

The *exchange bias* is the unidirectional pinning of the magnetization of a ferromagnet (FM) by an antiferromagnet (AFM) as a result of the magnetic interface exchange coupling. This anisotropy was discovered in 1956 by Meiklejohn and Bean[70] when studying Co particles embedded in their native antiferromagnetic oxide. Since then it was observed in many different systems containing FM/AFM interfaces; among these, AFM/FM bilayers are favored because of the improved control over the interface and of their easer integrability in devices.[71]

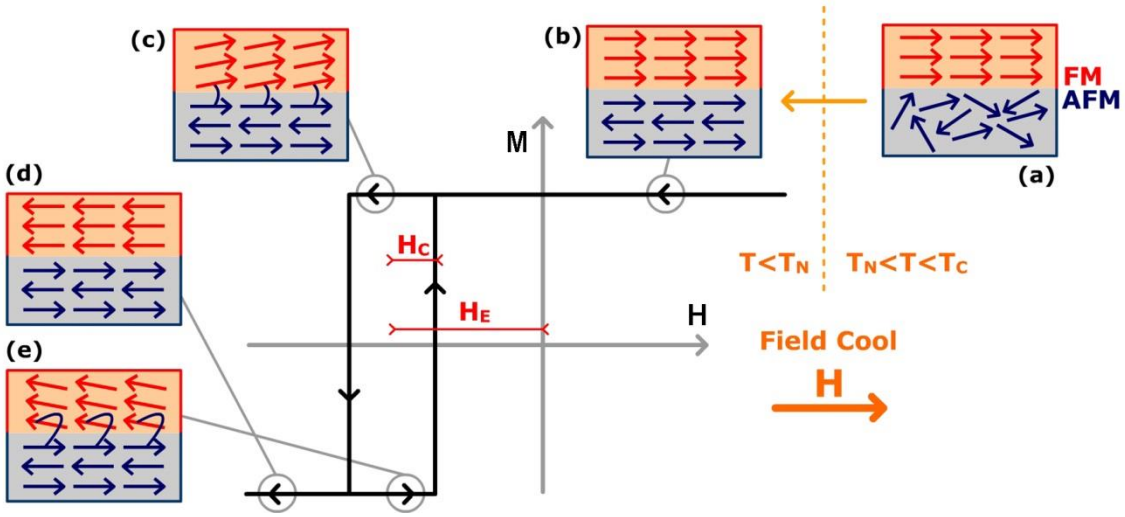

Fig. 2.8 Schematic diagram of the spin configuration of an FM/AFM bilayer at different stages (a)-(e) of an exchange biased hysteresis loop. Note that the spin configurations are not necessarily accurate portraits of the actual rotation of the FM or AFM magnetizations.

Exchange bias is observed cooling the AFM/FM bilayer in the presence of a static magnetic field from a temperature above T_N (AFM Néel temperature), and below T_C (FM Curie temperature) to temperatures $T < T_N$. After the field cooling procedure, the hysteresis loop of the AFM/FM system is shifted of a quantity H_E along the field axis generally in the opposite direction of the field. Furthermore, the hysteresis loops have an increased coercivity H_C. Both these effects disappear at the AFM Néel temperature, confirming that it is the presence of the AFM material which causes this anisotropy.

In the most intuitive picture shown in Fig. 2.8 (a), during the annealing the magnetization of the ferromagnetic layer aligns parallel to the external magnetic field H, while the spin configuration of the antiferromagnet remains random.
Upon the cooling through T_N, the AFM interfacial spins align ferromagnetically to the FM due to direct exchange interaction, while the other spin planes in the AFM "follow" the AFM order so as to produce zero net magnetization (b). When the field is reversed, at $T < T_N$, the FM spins start to rotate whereas the AFM spins remain frozen. Therefore, the AFM spins at the interface

exert a microscopic torque on the FM spins, to keep them in their original position (c). As a result, the FM spins have one single stable configuration (i.e. an unidirectional anisotropy) as if there were an extra (internal) biasing field shifting the hysteresis loop, i.e. *exchange bias*.

2.4.1 Modeling exchange bias

Meiklejohn's model[70,72] is based on the following assumptions: the FM and AFM layers are single magnetic domains; the AFM and FM anisotropy axes are parallel and the interface coupling is ferromagnetic. In this picture, the energy per unit area of an exchange bias system, assuming coherent rotation of the magnetization, can be written as:

$$E = -HM_{\mathrm{FM}}t_{\mathrm{FM}}\cos(\theta-\beta) + K_{\mathrm{FM}}t_{\mathrm{FM}}\sin^2\beta + K_{\mathrm{AFM}}t_{\mathrm{AFM}}\sin^2\alpha + \\ -J_{\mathrm{INT}}\cos(\beta-\alpha) \tag{2.8}$$

where H is the applied field, M_{FM} the saturation magnetization, t_{FM} and t_{AFM} the thickness of the FM and AFM layers, K_{FM} and K_{AFM} the anisotropy constants of the FM and AFM layers and J_{INT} the interface coupling constant. As shown in Fig. 2.9 (a), β is the angle between the magnetization and the FM anisotropy axis, α is the angles between the sublattice AFM magnetization (M_{AFM}) and the AFM anisotropy axis, and θ is the angle between the applied field and the FM anisotropy axis. The first term in the energy equation accounts for the effect of the applied field on the FM layer, the second term is the effect of the FM anisotropy, the third term takes into account the AFM anisotropy and the last term takes into consideration the interface coupling.

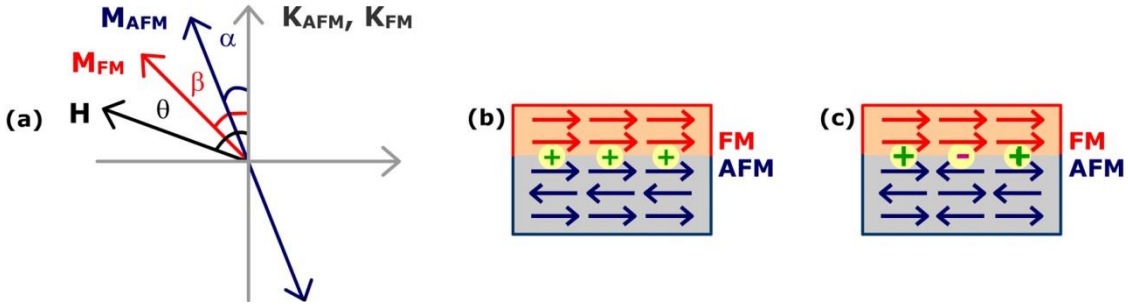

Fig. 2.9 In (a), schematic diagram of angles involved in an exchange bias system. On the right, spin configuration at a smooth ferromagnet-antiferromagnet interface in case of (b) uncompensated moment structure and (c) compensated moment structure.

In the simplest case, the FM anisotropy is assumed negligible (this condition is often fulfilled in experiments): $K_{\mathrm{FM}}\,t_{\mathrm{FM}} << K_{\mathrm{AFM}}\,t_{\mathrm{AFM}}$. Thus Eq. (2.8) becomes:

$$E = -HM_{\mathrm{FM}}t_{\mathrm{FM}}\cos(\theta-\beta) + K_{\mathrm{AFM}}t_{\mathrm{AFM}}\sin^2\alpha - J_{\mathrm{INT}}\cos(\beta-\alpha) \tag{2.9}$$

Minimizing the energy with respect to α and β, one obtains the loop shift:

$$H_E = \frac{J_{\mathrm{INT}}}{M_{\mathrm{FM}} t_{\mathrm{FM}}} \tag{2.10}$$

Another important result from this minimization is that the condition $K_{\mathrm{AFM}} t_{\mathrm{AFM}} \geq J_{\mathrm{INT}}$ is required for the observation of exchange anisotropy: if the above condition is not satisfied, the AFM spins follow the motion of the FM layer, thus no loop shift should be observed, only an increase of coercivity.

From Eq. (2.9) it is clear that the loop shift magnitude is determined by J_{INT}. Considering a J_{INT} similar to the ferromagnetic exchange, H_E is predicted to be several orders of magnitude larger than the experimental results; this simple ideal model, although it provides a useful and intuitive explanation of the phenomenon, does not represent in a proper way the FM/AFM interfacial environment. Meiklejohn's model assumes a perfectly smooth interface and a totally uncompensated spin configuration (Fig. 2.9 (b)) at the AFM/FM interface, i.e. considers all the AFM interfacial spins aligned in the same direction. Since the predictions far exceed the actual exchange bias magnitudes, the totally uncompensated spin configuration seems unlikely.

Recently, micromagnetic models have studied the AFM/FM interface ground spin configuration varying the number of uncompensated moments.[73] It was found that the favorable configuration in case of fully compensated interfaces is achieved when the FM magnetization lays perpendicular to the AFM uniaxial anisotropy axis. Increasing the amount of uncompensated moments, leads to a rapid transition from perpendicular to parallel anisotropy.

It is widely accepted that breaking the in-plane translational symmetry for having uncompensated spins is required to explain bias in most systems.[74] This symmetry breaking can either be the result of interface roughness, magnetic domains, defects, the grain structure, or of a combination of these four factors.

Elaborate models have been developed considering one or more of these conditions as possible sources of bias. A key factor, common to most of this models, is that the uncompensated spins are distributed stochastically in the AFM, supporting the conjecture of a statistical origin of the exchange bias.

In this context, relatively recent XMLD (X-ray magnetic dichroism spectro-microscopy) investigations[75] have shed some light on the micromagnetic structure on both sides of a ferromagnetic/antiferromagnetic interface, confirming that the bias of the ferromagnetic spins is determined, domain by domain, by the spin directions in the underlying antiferromagnetic layer. This local bias is attributed to a surplus of uncompensated spins in the individual AFM domains which are frozen in after growth. The cooling through T_N has the function to shift the

balance of the microscopically biased domains, resulting in a preferred macroscopic spin direction, that is, exchange bias.

Despite the multitude of models which have been developed, the exchange anisotropy remains an open issue especially concerning the interfacial interactions at the atomic scale, which are still unclear. Furthermore, even narrowing down to the macroscopic behavior, for having reliable predictions the general models must be accompanied by considerations about the specific system.

2.4.2 Exchange bias in AFM/FM bilayers

It has been observed that exchange bias is roughly inversely proportional to the FM thickness ($H_E \propto 1/\, t_{\mathrm{FM}}$),[71] indicating that exchange bias is an interface effect. However, if the FM layer is too thin, the relation is no longer valid, probably because the FM layer becomes discontinuous. The thickness at which this occurs (usually a few nm) varies from system to system and depends on the microstructure and growth of the FM layer.

The dependence of H_E on the AFM thickness is more complicated and depends on the specific system, on its microstructure and on the measurement temperature. The general trend is that for thick AFM layers, e.g. over 20 nm, H_E is independent on the thickness of the AFM layer. As the AFM thickness is reduced, H_E decreases abruptly and finally, for thin enough AFM layers (usually a few nm) H_E becomes zero, as shown in Fig. 2.10 (a). The decrease of H_E for thin layers is due to several factors. As discussed, the condition $K_{\mathrm{AFM}} t_{\mathrm{AFM}} \geq J_{\mathrm{INT}}$ must be fulfilled for having a non-zero H_E; furthermore, the AFM domain structure may also affect H_E if the thickness becomes comparable to the AFM domain wall size. Finally, decreasing the thickness of the AFM layer may change the AFM grain size which in turn influences the critical thickness at which H_E becomes 0.

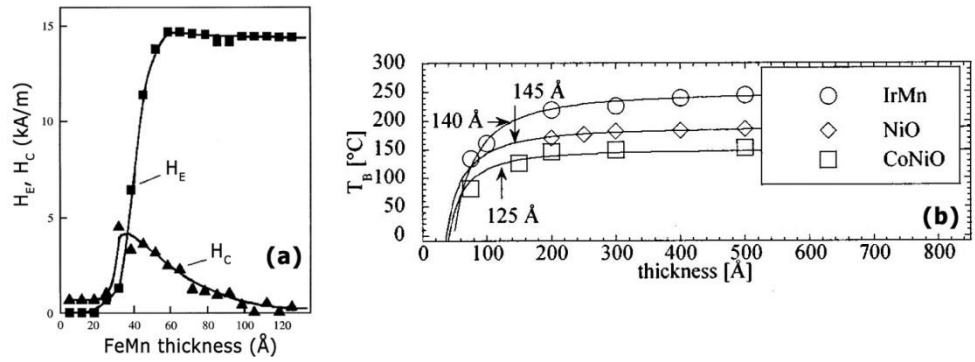

Fig. 2.10 In (a), dependence of exchange bias H_E and coercivity H_C with the AFM layer thickness for 7 nm $Fe_{80}Ni_{20}$ on FeMn (from [72]). In (b), blocking temperature as a function of $Co_{0.5}Ni_{0.5}O$, NiO, and IrMn thickness with theoretical curve fits (from [76]).

The exchange bias vanishes above the *blocking temperature* (T_B). T_B can be much lower than the bulk T_N. The origin of this effect seems to be related, at least in part, to the grain size and thickness of the AFM layer. In other words, if the grain size (or the layer thickness) is smaller (thinner) than a system dependent critical dimension of the AFM, the Néel temperature of the AFM is substantially reduced Fig. 2.10 (b)). This assumption seems to be supported by the fact that systems with single crystal AFM or thick AFM films with large grains tend to have $T_B \sim T_N$, while systems with very thin films have $T_B < T_N$.[76]

2.5 Interlayer Exchange coupling

The antiferromagnetic coupling between two ferromagnetic layers separated by a thin non-magnetic spacer was first observed by Grünberg in 1986.[77] A few years later, Parkin discovered that the coupling oscillates between the ferromagnetic and the antiferromagnetic configuration as a function of the spacer thickness.[78]

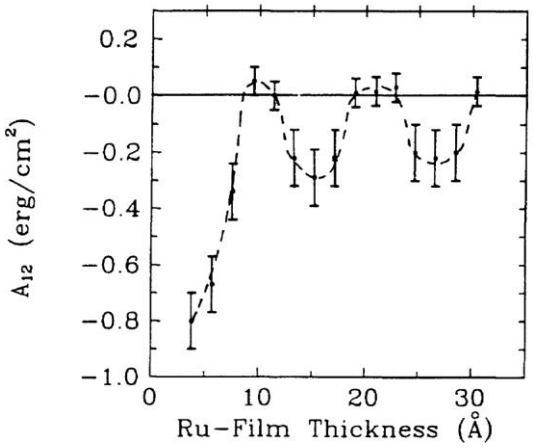

Fig. 2.11 Determined values of the interlayer exchange constant, A_{12}, as a function of the Ru layer thickness in Co/Ru superlattices deposited by magnetron sputtering. From [79].

The interaction which is responsible of this behavior is often referred to as *bilinear coupling* because the coupling energy per area is proportional to the product of both the magnetizations of the ferromagnetic layers $\widehat{\boldsymbol{m}_\iota}$:

$$\frac{E}{A} = -A_{12}\widehat{\boldsymbol{m}_1}.\widehat{\boldsymbol{m}_2} \tag{2.11}$$

in this form, positive (negative) values of the coupling constant A_{12} favor a parallel (antiparallel) alignment of the magnetizations.

Fig. 2.11 shows the oscillatory dependence of the interlayer exchange coupling A_{12} on the Ru spacer thickness in case of sputtered Co/Ru superlattices. Oscillations with a period of 11.5 Å are resolved.[79]

Since the first experiments, a great number of theoretical studies has been performed, essentially focusing on the oscillatory character of the coupling. In 1993, the *quantum well model*[80,81] allowed a unification of the previous works about the interlayer exchange coupling. Such model is based on spin-dependent reflections at the boundaries of the spacer metal with the ferromagnetic layers. This confinement of the conduction electrons in the spacer leads to a modification of the density of states in the spacer and to a change in the system's energy. Since the reflection coefficients are spin-dependent, the change in energy will be different for ferromagnetic and antiferromagnetic alignment of the magnetizations of the two ferromagnetic layers (Fig. 2.12). In this framework, the oscillatory behaviour of the coupling is due to the change in the energy and occupation of quantized states with the thickness of the spacer, which causes alternatively the parallel or the antiparallel configurations to have the lowest energy. For more details on the model, see [80,81].

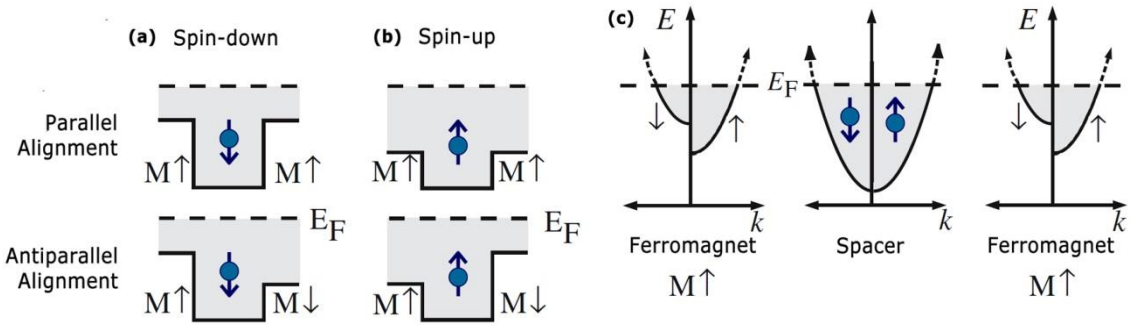

Fig. 2.12 Spin-dependent quantum wells seen by a spin-up (a) and spin-down (b) confined electron for parallel and antiparallel magnetizations of the ferromagnetic layers. In (c) the spin-split bandstructure for the ferromagnetic layers and the spin-independent one of the spacer.

2.6 Néel coupling

The orange peel coupling, or Néel coupling, is a ferromagnetic coupling between two magnetic layers separated by a non-magnetic spacer and is induced by the magnetostatic interaction between the magnetic poles at rough interfaces. It was first studied by Néel in 1962,[82] who provided a model in the approximation of an infinite thickness of the magnetic layers. The model was further refined by Zhang[83] and Kools[84] for keeping into account of the finite thickness of the layers.

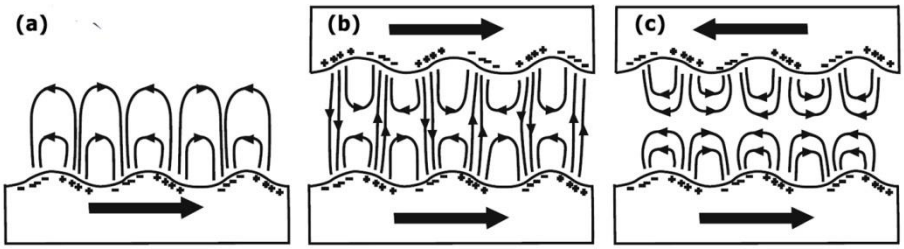

Fig. 2.13 Orange peel coupling from correlated roughness. Fringe field and magnetic "charges" in case of a rough surface (a), of two separated magnetic layers with parallel magnetizations (low energy configuration) (b) and of two separated magnetic layers with antiparallel magnetizations (high energy configuration) (c). From [85].

When the surface of a ferromagnetic material is rough, magnetic poles arise because the intralayer exchange is strong enough to prevent the magnetization from rotating and following the surface profile. When the roughness is slowly varying and its amplitude is small compared to the distance between the two magnetic layers, it is possible to describe the magnetic configuration at the interfaces with distributions of magnetic "charges" on flat surfaces:

$$\sigma(\mathbf{R}) = \mathbf{M} \cdot \mathbf{n}(\mathbf{R}) \tag{2.12}$$

where **M** is the magnetization of the layer (which is uniform in the plane) and **n**(**R**) is the normal to the surface (which changes due to the corrugation with the position on the surface **R**).

In case the layers have a correlated roughness, the two interface normals will be locally opposite. Ferromagnetic coupling arises from the fact that, if the two magnetizations are aligned ferromagnetically, also the magnetic charges will be locally opposite, thus minimizing the magnetostatic energy of the system (Fig. 2.13 (b)).

2.7 Micromagnetism

The magnetic response of a material is the result of many competing physical processes. The easiest way for predicting the magnetization **M**(**H**) of a material under the influence of an external field is to find its equilibrium configurations. This can be done summing all the energy contributions to the system, and then minimizing the expression with respect to the **M** vector. There are four main contributions to the energy of the system, i.e. mainly four physical processes tailor the behavior of the system: exchange energy, magnetocrystalline anisotropy, magnetostatic interaction and Zeeman energy.

Exchange Energy. The exchange interaction is the responsible for ferromagnetism and for many other magnetic interactions i.e. exchange bias or bilinear coupling in magnetic multilayers. Usually it is described by the Heisenberg hamiltonian:[86]

$$H = -\sum_{i \neq j=1}^{N} J_{ij}\mathbf{S}_i\mathbf{S}_j \tag{2.13}$$

where $\mathbf{S}_i$ is the spin angular momentum of the ion localized in the *i* lattice position and the exchange integral J_{ij} measures the intensity of the exchange coupling between the moments *i* and *j*. Usually, in cubic crystals, the exchange integral decreases rapidly increasing the distance between the atoms, so the sum is performed only among first neighbors. The exchange energy is totally isotropic, because it does not depend on the absolute direction of the two spins. As a result, if there was no other energy term, the magnetization would always vanish in zero applied field.

Magnetocrystalline anisotropy. Crystalline magnetic materials exhibit magnetic anisotropy since their magnetic properties are different along different crystallographic directions. As a result, the magnetization aligns easier along certain crystallographic directions, the so-called *easy-axes*, whereas it aligns with more difficulty along other directions, the so-called *hard-axes*; this fact has a major influence on the shape and properties of the hysteresis loops of the magnetization. The magnetocrystalline anisotropic energy is defined as the work needed to align the magnetization along one direction starting from the easy axis. In systems with only one preferred direction (*uniaxial anisotropy*) the energy density *E*/*V* can be written as a power series of $\sin\theta$, where θ is the angle between the magnetization and the preferential direction of the crystal *z*:[86]

$$\frac{E}{V} = K_0 + K_1 \sin^2\theta + K_2 \sin^4\theta + \cdots \tag{2.14}$$

If $K_1 > 0$ the energy is minimized when moments align along *z*, which becomes the easy-axis; if $K_1 < 0$, there is an easy-plane where the energy is equally low perpendicular to *z*. It is possible to quantify the strength of the anisotropy by introducing the anisotropy field $H_K = 2K/\mu_0 M_S$, where M_S is the saturation magnetization of the material.

Magnetostatic interaction (shape anisotropy). The magnetic moments interact with the dipolar field created by the neighboring moments. When the sample has finite dimensions, magnetic poles form at the surface giving rise to a stray field outside and inside the material. The lowest energy configuration is the one which minimizes this stray field by confining it in the sample, in a sort of closed flux configuration, according to the general expression for the magnetostatic energy:

$$E_M = -\frac{1}{2}\mu_0 \int_{all\ space} H^2 dV \tag{2.15}$$

The presence of magnetic domains in the system is mainly the result of the competition between the exchange interaction and magnetic anisotropy, which tend to align the moments, and the magnetostatic interaction which tries to minimize the stray field favoring close paths for the magnetization inside the material as shown in Fig. 2.14. This results in the formation of the so-called magnetic domains, regions in which the atomic magnetic moments are aligned.

For magnetic bodies with second order surface the demagnetizing field can be expressed through the following relation: $\mathbf{H}_\mathrm{D} = N \cdot \mathbf{M}$, where **M** is the magnetization vector and *N* the demagnetizing tensor, which is strongly related to the shape of the material. The shape-dependence of the demagnetizing field can be exploited in patterned systems for inducing shape-dependent preferential directions for the magnetization, i.e. the so-called *shape anisotropy*. In general, the demagnetizing field will be stronger along the direction corresponding to a small extension of the sample, because the stray field to counteract is larger. On the contrary, the magnetization will be forced to align along the long side of the sample. This is also the reason why thin-films usually show preferentially in-plane magnetization.

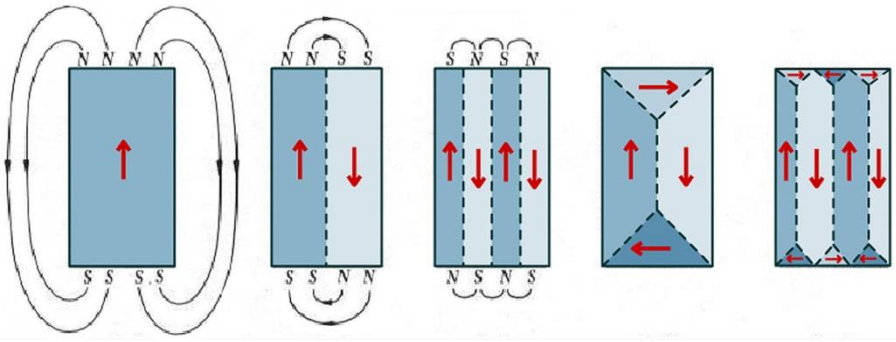

Fig. 2.14 Domain formation: from left to right, reduction of the stray field and of the magnetostatic energy by domain creation.

Zeeman Energy. This is the energy possessed by the magnetic moments in an external applied field **H** and it is described by the relation:

$$E_Z = -\mu_0 \int_V \mathbf{H} \cdot \mathbf{M} dV \tag{2.16}$$

where *V* is the sample volume. It is, like the magnetostatic interaction among the material dipoles, a long-range energy contribution.

2.8 Superparamagnetism

In the sub-micron size range magnetic objects are often in single domain configuration. In the simplest approximation, a single domain particle with uniaxial anisotropy, will then have two possible magnetization states, parallel or anti-parallel to the direction of its easy axis. These two states are separated by an energy barrier, which is related to the anisotropy of the material. The energy, as a function of the magnetization angle θ formed with the anisotropy axis, is $E(\theta) = KV \sin^2 \theta$, where K is the material anisotropy constant and V is the particle volume. The transition between the two states can be thermally activated, with an average time between two events which is given by:

$$\tau = \tau_0 \exp\left(\frac{KV}{k_B T}\right) \tag{2.17}$$

where k_B is the Boltzmann constant, T is the absolute temperature and τ_0 is of the order of 10^{-9} – 10^{-11} s for non-interacting particles. As the particle size is reduced, the energy barrier KV decreases and the rate of switching goes up. At $KV/k_B T \approx 25$, the switching time goes below 1 s and the particles are called *superparamagnetic*. The diameter at which a particle becomes superparamagnetic lies in the range from 5 to 10 nm.[87] In this condition, the magnetic moment of the particle as a whole is free to fluctuate in response to the thermal activation, while the individual atomic moments maintain their ferromagnetic ordered state relative to each other.[88]

The observation of superparamagnetism depends both on the temperature, as stated in Eq. (2.17) but also on the experimental observation time. The superparamagnetic blocking temperature, T_b, is defined as the temperature at which the superparamagnetic relaxation time equals the timescale of the experimental technique. Below the blocking temperature, the ferromagnetic order appears, because the magnetization relaxation process becomes slow in comparison to the time required by a particular investigation technique. In absence of external magnetic field, the resulting fluctuations in the direction of the magnetization cause the total magnetic moment average to be zero. This means that superparamagnetic particles have no remanent magnetization and, when inserted in a field, their magnetic moment will tend to align to the field lines. In addition, in contrast to paramagnetic materials, whose relative magnetic susceptibility is significantly lower, the magnetization of superparamagnetic materials can easily attain the saturation magnetization M_s, which is very high for ferromagnetic materials (Fig. 2.15 (a)).

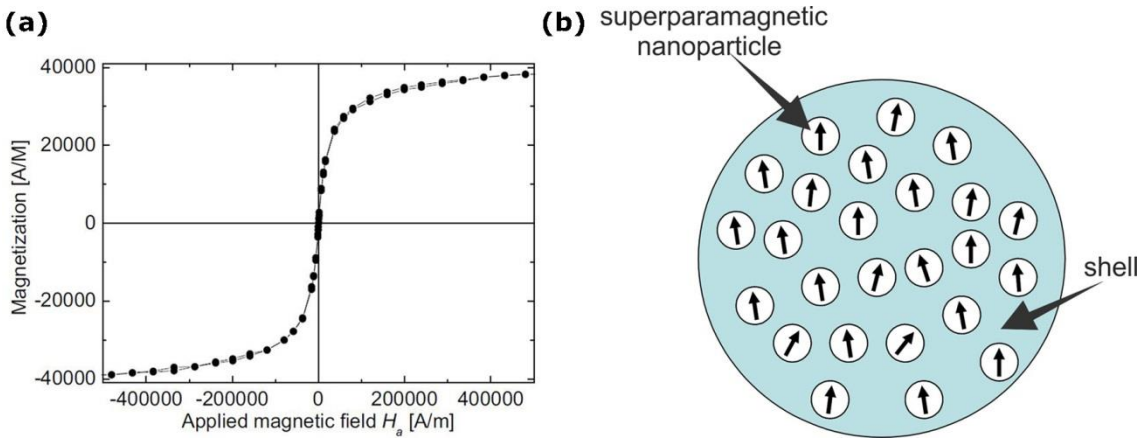

Fig. 2.15 (a) Hysteresis loop for Invitrogen MyOne® superparamagnetic beads measured by using a vibrating sample magnetometer. (b) Magnetic bead formed by magnetic nanoparticles in a non-magnetic matrix/shell.

In most of the biomedical applications, magnetic particles should react strongly to an applied magnetic field while agglomeration and clusterization of particles is highly undesired. For these reasons, the absence of remanence and the high χ_r value have made superparamagnetic particles widely used. These properties allow the particles to be separated using a magnet, but also to be easily resuspended when removed from the magnetic field.

In the experimental part of this thesis, Micromod nanomag® -D streptavidin nanoparticles with 250 nm diameter nm were used. Such beads consist of a nonmagnetic polymeric matrix with inclusions of small iron oxide superparamagnetic nanoparticles, as shown in Fig. 2.15 (b).

Superparamagnetism is observed also in magnetic thin films, below a critical thickness which depends on the material and deposition conditions. The weakening of ferromagnetism in thin films can be attributed to different mechanisms. As a thin film transitions from three-dimensional to two-dimensional ferro-magnetism, the magnetic ordering temperature T_C is often reduced. If a thin film's T_C drops below room temperature, the measured room-temperature coercivity will vanish. On the other hand, when a thin enough film is deposited, it can form magnetic islands or clusters rather than a continuous film. These magnetic clusters will be superparamagnetic as long as the ambient thermal energy is large enough to cause relaxation of the magnetization vectors of the clusters. In the superparamagnetic state, coercivity can also vanish if the measurement speed is slow relative to the relaxation rate of the magnetization.[89,90]

In this thesis work, superparamagnetism in thin CoFeB layers (below 1.5 nm[89]) grown on MgO is exploited, together with the shape anisotropy, for having a linear and hysteresis free sensor response (see section 4.2).

3. Experimental Techniques

3.1 Magnetron Sputtering

Magnetron sputtering is a physical vapor deposition technique which allows a good film adhesion to the substrate, and a high control on the thickness, uniformity and composition of the deposited material. Furthermore, even materials with very high melting points and low vapor pressure are easily sputtered while evaporation of these materials is problematic or impossible. The availability of many parameters that control sputter deposition make it a complex process, but also allows large degree of control over the growth and microstructure of the film. Fig. 3.1 shows a sketch of the sputtering process.

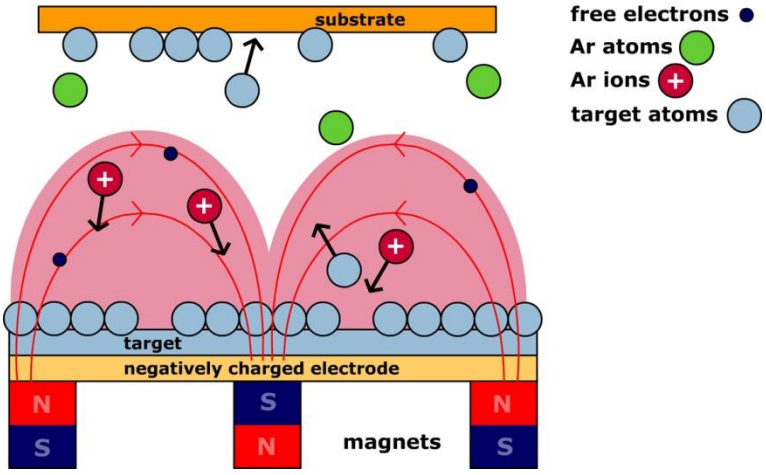

Fig. 3.1 Schematic of the magnetron sputtering process.

In sputtering chambers, first a gaseous plasma is created, then plasma ions are accelerated towards the source material (the so-called *target*), which is eroded by ions via momentum transfer. This causes an ejection of the source material in the form of neutral atoms, clusters of atoms or molecules. As these neutral particles are ejected, they will mainly travel in a straight direction (apart from the interaction with the reactive gases in the chamber) until they come in contact with the substrate, such as a Si wafer, that is finally coated by a thin film of the source material. In order to create the plasma, atoms of an inert gas (frequently Ar) are introduced into the HV (High Vacuum) chamber and a negative bias voltage is applied to the target. Free electron and Ar^+ ions are immediately accelerated by the electron field in proximity to the

target and ionize by collision the Ar atoms leaving Ar^+ ions and e^- free electrons. The newly ionized Ar^+ ions and electrons, accelerated by the target potential, ionize other Ar atoms in a cascade process which ignites the plasma. At this point, positively charged Ar^+ ions are accelerated towards the negatively biased electrode, striking the surface and releasing source material and more free electrons by energy transfer.

In magnetron sputtering, permanent magnets are located behind the target in order to confine the free electrons in a magnetic field directly above the target surface. This provides a double advantage: first, the free electrons, which are rejected by the negatively charged target, are prevented from bombarding the substrate, which would cause overheating and structural damage; second, the circuitous path carved by the free electrons along the lines of the magnetic field enhances the probability of ionizing neutral Ar atoms by several orders of magnitude. This increase in available ions significantly increases the rate at which target material is eroded and subsequently deposited onto the substrate.

A particular care must be taken when insulating and/or ferromagnetic targets are used. In the former case, charge build-up effects hinder the erosion mechanism. This can be avoided with the use of *RF sputtering* where the sign of the target bias is varied at a high rate. When RF power is used, usually the minimum Ar pressure needed for igniting the plasma is higher than the deposition pressure, for this reason a *plasma-strike* with high Ar pressures is performed before the deposition. When ferromagnetic targets are used, instead, the problem lies in the stray magnetic field leaking from the target. The solution is to counteract this field placing specifically designed magnets behind the target.

AJA Orion sputtering system. In this work, the AJA ATC Orion sputtering system shown in Fig. 3.2 has been used. This system is provided with 10 magnetron sputtering sources which are arranged in a specific circular pattern and pointing to a common focal point, where the substrate is located. The sources are positioned in the bottom part of the chamber in the so-called *sputtering up* configuration, so that sputtered material travels from the bottom to the top, avoiding redeposition on the substrate and giving cleaner samples with respect to sputtering-down systems. As counterpart, the redeposition of material on the sources surface can be a source of shortcuts of the guns and a specific cleaning procedure of the chamber after a long period of use is recommended. Depending on the material, the sources are powered either by DC generators, for Ru, Ta, IrMn, Ti, Au and CoFeB, or by a RF generator, for SiO_2, MgO, Al_2O_3 and CoFe. The latter needs an RF bias not because of charging problem, but because its strong magnetization gives rise to a high stray field which makes the plasma ignition difficult. The deposition chamber is kept in HV around 10^{-9} Torr by a cryopump which is located on the side of the chamber. The substrate holder, which is bound to the top cap of the vacuum chamber, can be moved in the vertical direction for optimizing the substrate-target

distance, which affects first of all deposition rate and uniformity. Besides, it can be heated in a controlled fashion through a PID controller, and biased through DC or RF generators. Furthermore, a permanent magnet (H ~ 300 Oe) can be added to the sample-holder in order to induce an uniaxial anisotropy direction in the ferromagnetic films.

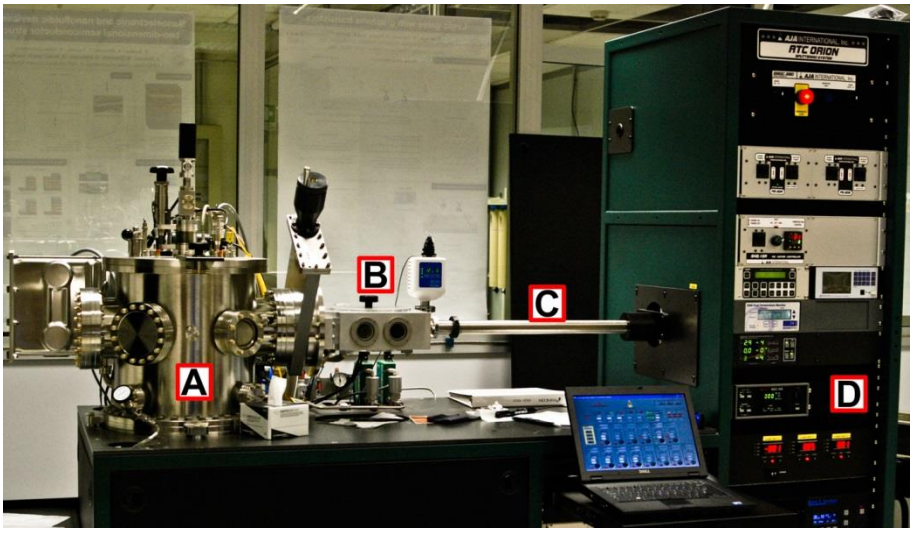

Fig. 3.2 Our AJA ATC Orion sputtering system. A is the deposition chamber, B is the load-lock, C the transfer arm, D the generators which power the sources located under the deposition chamber.

During deposition, the substrate holder is kept in rotation for guaranteeing a low non-uniformity of the deposited film, below 2% in a three inches wafer. The substrates are transferred into the deposition chamber through the adjacent load-lock, which is turbo-pumped down to the 10^{-6} Torr before to start the transfer. This reduces dramatically the sample contaminations and inclusions and allows multistep processes. The deposition process is entirely controlled remotely by the *Phase II* Labview software, which can be operated either manually, i.e. setting all the parameters real-time while depositing, or automatically, i.e. saving all the parameters before the deposition in "process" files which are then recalled later. In the latter operation mode the machine switches automatically all the deposition parameters during deposition, allowing for high reproducibility. For determining the deposition rate, a quartz micro-balance is mounted in the deposition chamber. It relies on the change in the resonance frequency of a quartz crystal when additional material is deposited onto it.

3.2 Optical Lithography

Optical lithography is a widespread microfabricating method which combines high throughput to a high resolution (below 1 um, depending on the light source employed). This technique is based on transferring a certain bidimensional geometry *pattern* from a template, the *mask*, to the sample, exploiting the change in solubility of a suitable polymer, the *photoresist*, when it is

exposed to UV light. Essentially, first the photoresist is cast over the whole sample in the so-called *spinning* process, then the mask is placed upon the sample and then the system is irradiated with UV light. The pattern on the mask is defined by the contrast between the zones which are transparent to UV light and the zones which are not. As a consequence, after UV irradiation, the mask pattern is transferred onto the resist in the form of soluble zones and non-soluble zones. The last step, the *development*, consists of treating the sample with a suitable solvent which wipes away the soluble zones and leaves unchanged the non-soluble ones. As a result, the mask pattern is transferred onto the sample in the form of zones with resist and zones without resist. After optical lithography, the pattern is effectively transferred to the sample by either etching away *subtractive* process) or covering with additional material *additive* process) the zones which are unprotected by the resist.

3.2.1 The process

A generic process, shown Fig. 3.3, consists of the following steps:

(a) Cleaning the sample
(b) Depositing the photoresist (spinning process)
(c) Exposing the sample to UV radiation
(d) Developing the resist
(e) Subtractive or additive process
(f) Strip of lift-off

In the following paragraphs a detailed description of each lithographic step will be given.

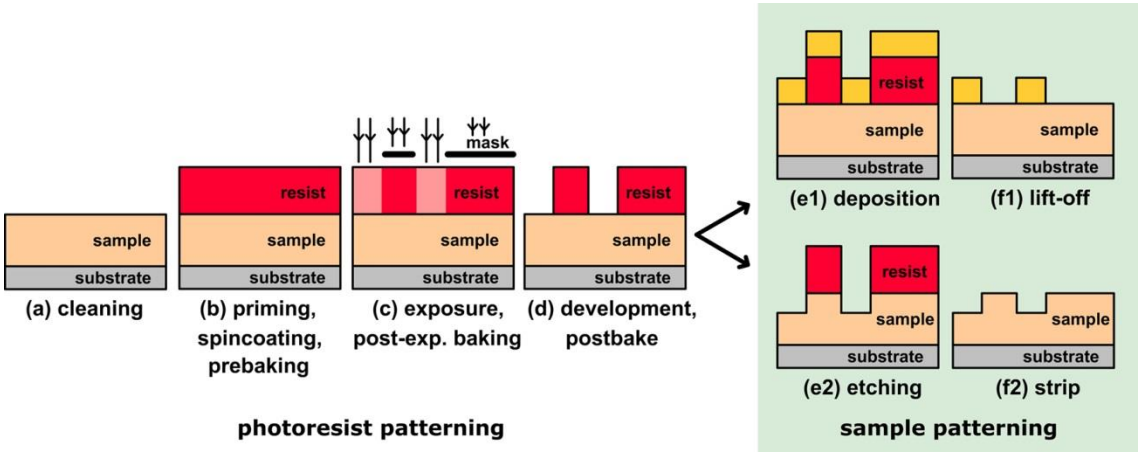

Fig. 3.3 Main phases of a photolithographic process with positive resist.

Cleaning of the sample. Superficial contaminations can hinder the resist adhesion and the good quality of the transferred image. In case the surface is already cleaned, a simple heating at T=120°-140° C for a few minutes is enough for enabling the H_2O desorption from the surface. When the surface is contaminated by particles or organic impurities, the standard cleaning procedure consists of an ultrasonic bath in acetone and a subsequent isopropanol rinsing for removing the contaminated acetone and avoiding the formation of acetone halos on the surface. A better adhesion of the resist is achieved on hydrophobic surfaces, because the polymer is an apolar substance and the formation of polar bounds O-H prevent the resist from wetting the substrate. For achieving hydrophobicity, an adhesion promoter *Primer* is deposited on the sample surface in the same way as the photoresist (see below).

Deposition of the photoresist. The deposition of the resist occurs via *spin coating*. Some drops of resist are dispensed on the sample, which is put in rotation at high speed. The centrifuge force at about 1000 rpm spreads the resist, creating a uniform, thin (some microns thick) layer. The resist thickness *t* depends on the angular speed and on the viscosity η of the polymer in accordance with the empirical formula:

$$t = K\frac{C^{\alpha}\eta^{\beta}}{\omega^{\delta}} \tag{3.1}$$

where K, C, α, β, δ are parameters related to the particular system employed. The spin coating method provides a high processing speed and a high homogeneity of the layer thickness. In case the sample has no rotational symmetry, the resist becomes thicker at the corners due to the increased air turbulence during the spinning.

After the spincoating, a *soft baking* is performed keeping the sample at about T=100° C for several minutes. This allows the complete evaporation of the solvent containing the polymer, the decrease of the mechanic stresses induced by spincoating and the enhancement of the resist adhesion to the sample surface.

Exposition. The exposure to UV light radiation modifies the chemical properties of the resist, producing a different solubility in the exposed and non-exposed part of the film. The image transfer is realized through a mask obtained by patterning with Cr a transparent quartz substrate, so that the metallized zones absorb the radiation, protecting the underlying resist from the exposure. The mask-aligner used in this work is the Karl Suss MA56 (in Fig. 3.4 (a)), which allows to realize both the *contact* and *proximity* printing, using mask up to 5'' and wafer up to 4'' in diameter.

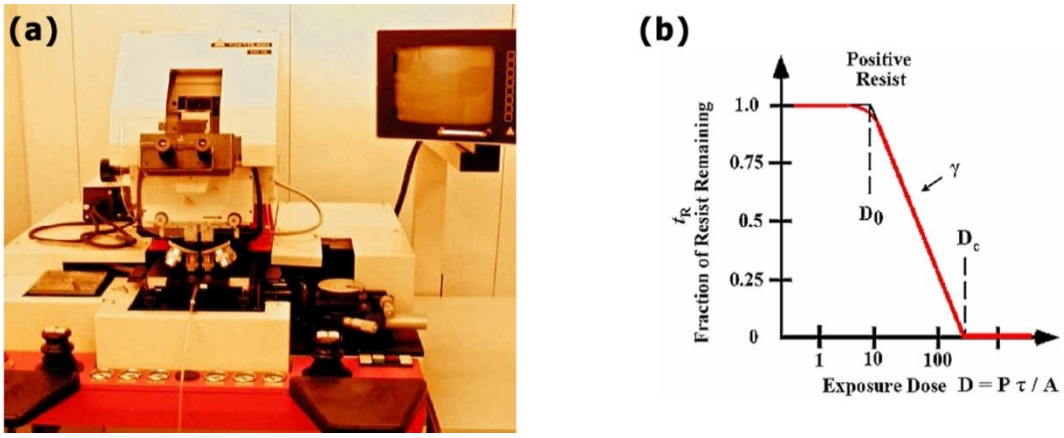

Fig. 3.4 (a) Our Karl Suss MA56 mask aligner. (b) Fraction of the remaining resist as a function of the dose.

The UV radiation is obtained from the Hg I line (365 nm) of a mercury lamp with an intensity of about 12.6 mW/cm^2. The resists employed is AZ5214E which is *positive*; this means that the exposure causes a breaking in the polymer chains, thus enhancing the resist solubility and consequently allowing its removal in the development step. The maximum achievable resolution is measured as critical dimension (CD), the linear dimension of the smallest object that is transferable through the mask. The resolution is limited by diffraction (in case of contact exposure, where the mask is in direct contact with the resist, the limit is CD ~ λ), by the quality of the mask and by the resist contrast.

The quantity of residual resist on the sample as a function of the dose D ($D = P \cdot \delta t \,/\, A$, with P power of the radiation, δt exposure time and A exposed area) is shown in Fig. 3.4 (b) for a positive resist. D_0 is the minimum dose for which the resist becomes soluble; D_C is the critical dose, above which the resist becomes completely soluble. The contrast is defined as:

$$\gamma = \frac{1}{\log \frac{D_C}{D_0}} \tag{3.2}$$

In a high contrast resist, the difference in solubility between exposed and non-exposed zones is enhanced, because it becomes less sensitive to the radiation scattered by the exposed zones. This leads to the formation of vertical and well defined walls after developing.

Photoresist development. During the developing process, an appropriate solvent removes the part of resist with higher solubility and leaves the rest unchanged. In case of positive resist, the exposed part is dissolved, while the part protected by the mask during exposure remains on the substrate. For a negative resist the mechanism is opposite.

Subtractive: etching and stripping. Ion beam etching, which is described in the next paragraph in detail, is based on the removal of the sample material due to the collision with accelerated Ar^+ ions.

In this case, the function of the resist is to protect the underlying material from the ion bombardment. At the end of the etching process, the residual resist is removed using acetone or other suitable solutions (e.g. the *Remover*).

Additive: deposition and lift-off. In this case the resist-covered areas are protected from the deposition of new material. After the deposition, the resist lift-off removes also the overlying material, leaving the deposited material only in the zones which were not protected by the resist.

3.2.2 Inverse photolithography

In order to facilitate the lift-off procedure, it is desirable to have slits in the newly deposited material, so that the solvent (e.g. acetone) can filter until the resist layer causing its detachment from the sample (Fig. 3.5 (f)). As shown in Fig. 3.5 (e), positive lithography gives rise to an uninterrupted deposited layer whereas, using a *negative* resist or an *inverted positive* resist, the suitable cracked profile is obtained. In our work we chose the latter option. Fig. 3.5 shows the steps of an inverse lithography process.

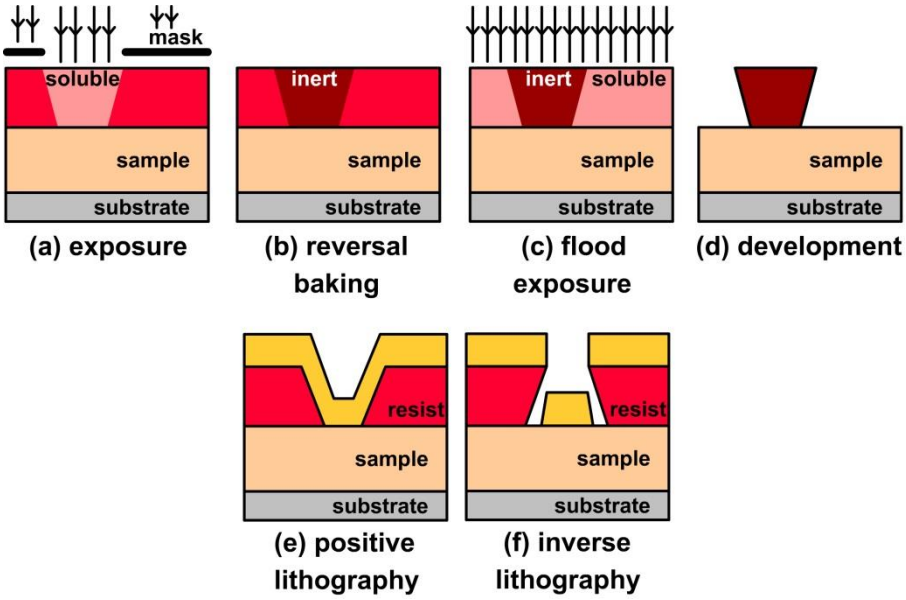

Fig. 3.5 In (a)-(d), inverse lithography process steps. In (e) and (f) *overcut* and *undercut* effects on the deposition, respectively. The undercut profile allows an easier detachment of the resist during the lift-off process.

After the exposition (a), the sample is baked so that a *cross-linking* of the polymeric chains in the exposed zones takes place. This makes the exposed area non-soluble and insensitive to further light exposure (b); after this, the sample is exposed without mask in the so-called *flood exposure* step (c). As a result, all the resist which was not exposed in the first step becomes soluble, whereas the rest, which experienced crosslinking, remains non-soluble (d). This

procedure allows to obtain the inversion of the mask image and an *undercut* profile (walls inclined more than 90°), which provides the slits required in the lift-off.

3.3 Ion Beam Etching

Fig 3.6 shows the ion beam etching (IBE) experimental apparatus. IBE is a physical dry etching technique where Ar^+ ions are accelerated towards the sample in a vacuum chamber ($p \sim 10^{-7}$ Torr by a cryopump). Not dissimilarly with what happens with sputtering targets, the sample material is removed by energy transfer between the accelerated Ar atoms and the sample surface. Ar^+ ions are generated from inert Ar gas through a discharge current. Here, a filament run by current, which is the cathode, emits electrons by thermoionic effect. These electrons, accelerated towards the anode by the tension applied between the electrodes (*discharge voltage*), hit and ionize the Ar atoms giving rise to Ar^+ ions and free electrons. These free electrons, which are also accelerated by the potential difference, contribute to maintain the plasma. Some of the Ar^+ ions are then accelerated toward the sample by a grid set at a negative potential (*accelerator voltage*).

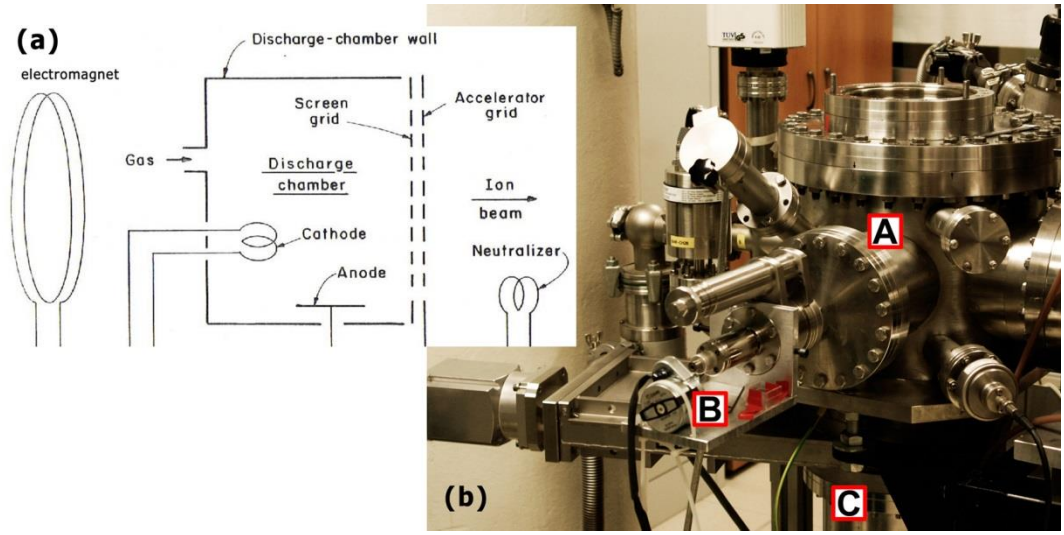

Fig 3.6 In (a), schematic of the ion beam etching experimental apparatus. In (b) our IBE system, where A is the etching chamber, B is the motor which enables the rotation of the sample during the etching process and C is the cryopump which keeps the etching chamber in HV.

Thanks to the decoupling between the electrodes which generate the plasma and those which accelerate the plasma to the sample, it is possible to control independently the flux of Ar ions (increasing or decreasing ionization through the *discharge voltage*) and the energy of the accelerated ions (through the *accelerator voltage* of the grid). Between grid and sample a second filament produces electrons by ionizing Ar atoms (Plasma Bridge Neutralizer). These electrons avoid the positive charge build-up on the sample both neutralizing the Ar^+ ions of the

beam before they reach the sample and directly compensating the positive charges on the sample surface. The Ar flux in the discharge chamber and the one for the neutralizer are independently controlled by two different fluximeters (both Ar fluxes are 4 sccm in our case). During the etching process, the sample holder is kept in rotation for insuring the uniformity of the etching rate on the whole surface. Furthermore, it is possible to tilt the sample holder with respect to the incident beam by 30° and 60° to avoid the redeposition of material during the etching.

The etching rate depends on many factors, including the composition of the etched material. If the sample, as in our case, consists of a multilayer stack of different materials grown under different conditions, it is rather complicated to calculate accurately the etching time, especially when dealing with critical lithographic processes such as the junction definition. For this reason, we employed a visual method based on the so-called flags for determining when to stop the etching. The flags are exact replicas of the to-be etched part of the sample, grown on a transparent substrate. During the etching, sample and flags are mounted together on the holder, so that they are etched in the same exact way.

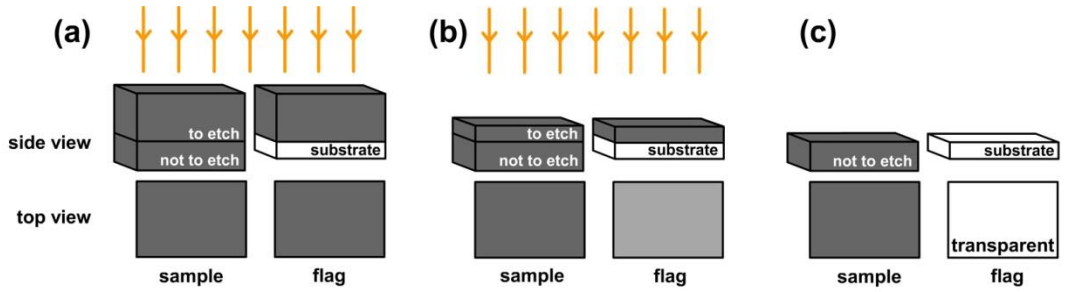

Fig. 3.7 Visual method based on the use of *flags* for determining when to stop the etching process.

As shown in Fig. 3.7, when the flags become transparent, it means that all the flag material and the correspondent part of the sample have been removed, thus the etching can be stopped. Of course, the flag-based method can be used only if the last layer to etch is not transparent, as it is in most of our cases.

3.4 Field annealing in vacuum

As we have seen before, the sensors must be annealed in a magnetic field before to be used. This allows to enable the crystallization of CoFeB layers and the improvement of the MgO barrier crystalline quality, which are key factors for having high TMR ratios. Furthermore, the magnetic field cooling through the Néel temperature of the antiferromagnet gives rise to the exchange bias used for pinning the magnetization of the bottom layer of the MTJ. However, excessively prolonged annealing times or too high annealing temperatures can damage or

destroy the sample. The main responsible for the deterioration of the sensor's properties (i.e exchange bias field or TMR value) with temperature treatments is the interdiffusion between layers which follows the Arrhenius law:

$$D = D_0 e^{-\frac{E_A}{RT}} \tag{3.3}$$

where D is the diffusion coefficient, T is the temperature, R is the gas constant and E_A is the activation energy for diffusion. For this reason it is crucial to design the annealing process accurately for finding a compromise between crystallization, exchange bias and interdiffusion.

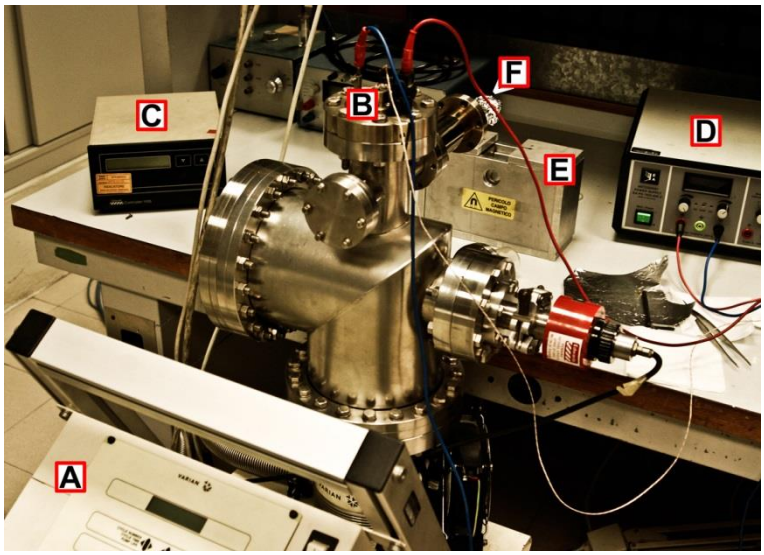

Fig. 3.8 Our high vacuum magnetic field annealing system. A is the turbopump; in B, the white wire is the thermocouple, and the blue and red cables are the filament electric connections; C is the vacuometer, D is the DC current generator, E is the permanent magnet; the cavity on the superior part is the lodging for the bulb; F is the sample holder.

Fig. 3.8 shows the high vacuum field annealing system. It consists of a vacuum chamber (pumped by a turbopump) which terminates with a transparent bulb. In the bulb, the sample is located upon a support in which it is heated by a resistive filament through Joule effect. The filament current, provided by a DC generator, is modulated by a PID controller connected to a thermocouple in thermal contact with the sample. The PID controller can be set for ramping from room temperature to a desired temperature (the top limit is about 500° C) simply setting the final temperature, the temperature rising rate (K/min), and how long to keep the final temperature. At the end of the process the slow cooling down is mainly achieved by irradiation through the transparent bulb, because there is no convection (vacuum) and the conduction through the sampleholder support is not significant. During the annealing process, the pressure must be always kept under control ($p < 10^{-4}$ mbar) in order to avoid contamination of the sample and to preserve the heating filament. The magnetic field is provided by a

permanent magnet which generates an approximatively uniform field of magnitude H ~ 2.5 kOe.

3.5 Magneto-optic Kerr effect

MOKE technique provides a powerful way for studying the magnetic properties of thin films by analyzing the light reflected from their surface. The incident light, which is usually generated by a laser diode, is polarized linearly before reaching the sample; the reflected light is analyzed through a polarizer (the *analyzer*) placed before a photodiode.

A linearly polarized electromagnetic wave can be decomposed in one right-handed (+) and one left-handed (-) circularly polarized components of equal amplitude. A magnetized material reflects the two components in a different way, introducing a difference between their amplitudes (which produces an ellipticity of the reflected wave) and phases (which cause a rotation of the major axis of the ellipse). It is possible to measure all the three components of the magnetization vector, varying conveniently the polarization of the incident light with respect to the sample and the angle of the analyzer (Fig. 3.9 (a)).

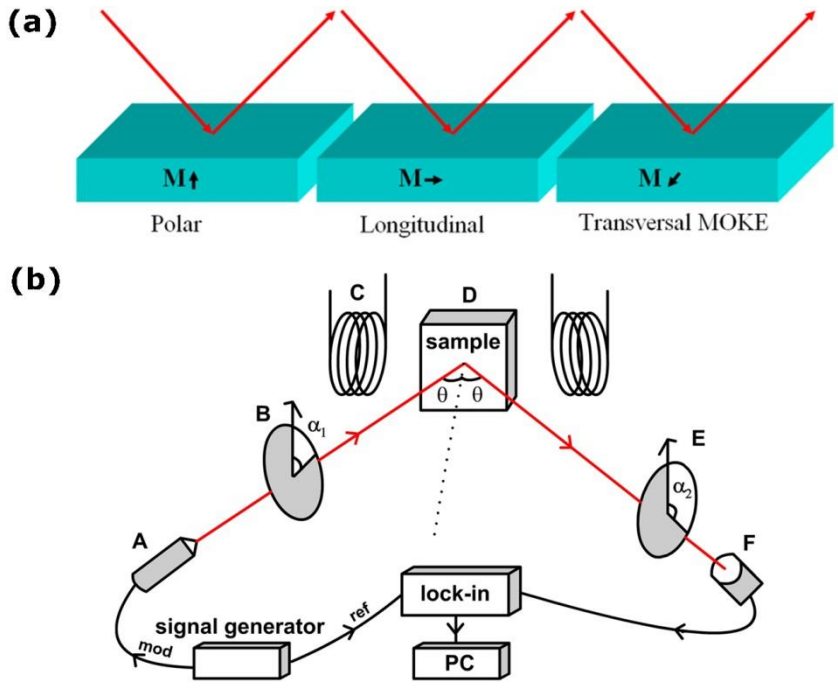

Fig. 3.9 (a) Schematic configurations of the sample magnetization for the polar, longitudinal, and transverse magneto-optical Kerr effects. (b) Sketch of our MOKE experimental setup.

Fig. 3.9 (b) shows the apparatus employed in this work. The sample D is located between the poles of an electromagnet C which generates the external magnetizing field H. The electromagnet is powered by a KEPCO generator which can be controlled remotely by the PC.

The light comes from a red λ = 635 nm laser diode A whose intensity is modulated by a signal generator in order to use afterwards a lock-in detector. The laser light impinging on the sample is linearly polarized by the polarizer B. The polarization angle α_1 can be either 0° (*s* configuration) or 90° (*p* configuration). The reflected light is analyzed by a second polarizer E whose axis is set perpendicularly to the first one (α_2=90° and α_1=0° for *s* and *p* configuration, respectively). Finally the light reaches the photodiode F where it is converted into a voltage signal which is subsequently demodulated by a lock-in amplifier. In an *s*-*p* configuration, the demodulated voltage signal is proportional to the longitudinal component of the film magnetization. The signal is then digitalized by a DAQ and sent to the PC where data are collected and analyzed in a Labview software. It is worth noting that MOKE measurement does not provide quantitative information about the magnetization vector, but gives an accurate picture of the hysteresis loops. Although MOKE is a surface-sensitive method, the probing depth is on the order of 10-20 nm thus, if the films are thin enough, one can also obtain information about the magnetization of the underlying layers. More details on MOKE technique can be found in Ref. [91].

3.6 Atomic Force Microscopy

Atomic force microscopy (AFM) is a high-resolution scanning probe microscopy, with demonstrated resolution below the nanometer. The AFM consists of a cantilever with a sharp tip (probe) at its end that is used to scan the specimen surface. The cantilever is typically made of silicon or silicon nitride, with a tip radius of curvature on the order of nanometers. When the tip is brought into proximity of a sample surface (few nanometers), forces between the tip and the sample lead to a deflection of the cantilever according to Hooke's law.[92] These deflections are measured using a laser beam, which reflects on the cantilever and is collected by a four sectors photodetector (Fig. 3.10 (a)). In most cases a feedback mechanism is employed to adjust the tip-to-sample distance to maintain a constant force between the tip and the sample. Traditionally, the sample is mounted on a piezoelectric system responsible for scanning in the *x*, *y* and *z* directions. The AFM can be operated in two different modes: static (also called contact) mode and dynamic (non-contact or "tapping") mode. In static mode, the cantilever is "dragged" across the surface of the sample in close contact with it and the contours of the surface are measured directly using the vertical deflection of the cantilever (which gives information about the surface topography), and the torsion of the cantilever (which is related with the friction forces between the tip and the sample). In the dynamic mode, the cantilever is externally oscillated at or close to its fundamental resonance frequency. The variation of the oscillation amplitude and phase with respect to the external reference oscillation provides information about the sample's characteristic.

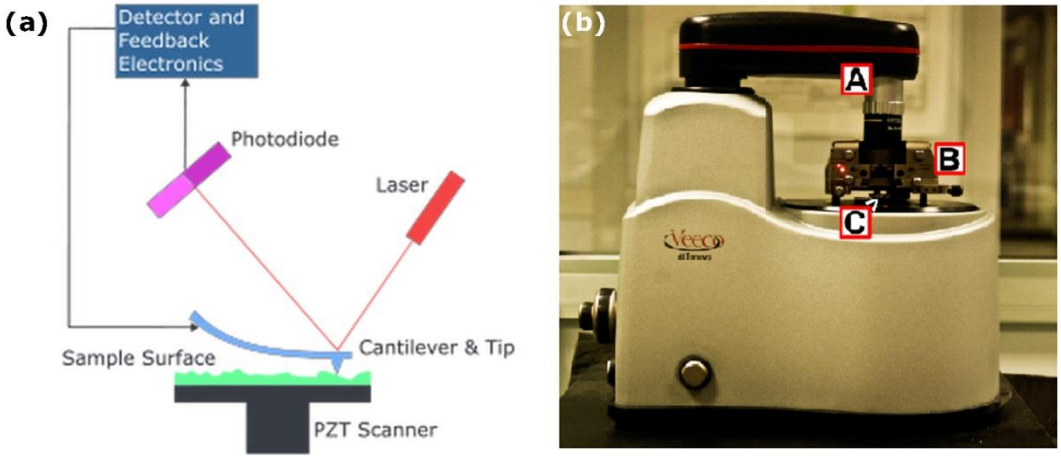

Fig. 3.10 (a) Sketch of an AFM measuring process; (b) Our Veeco AFM system, where A is the optical camera for centering the desired sample zone and B is the core of the AFM, which includes the AFM tip, the laser and the partioned photodiode; C is the sample holder.

The AFM measurements on magnetic multilayers were performed in a Veeco Innova® system (Fig. 3.10 (b)) in tapping mode, where the cantilever was driven to oscillate up and down near its resonance frequency and the amplitude of this oscillation typically ranges from 100 to 200 nm. A piezoelectric actuator was used to control the height of the cantilever above the sample. A tapping AFM image was therefore produced by imaging the force of the intermittent contacts of the tip with the sample surface. Tapping mode, compared to contact mode, combines an extremely high resolution with a significant reduction of tip-sample wear.

3.7 Electrical transport measurements

Electrical measurements in this work were used to study the *I-V* characteristic and magnetoresistive behavior of the tunneling junctions. In both cases, two-point or four-point probe measures can be performed. In the former case, referring to the experimental setup in Fig. 3.11 (a), each contact serves the double purpose of injecting the current in the device and measuring the resulting tension (or vice-versa). The intention is to determine the resistance R_{DUT} of the *device under test*. The total resistance is given by:

$$R_T = \frac{V}{I} = 2R_W + 2R_C + R_{\mathrm{DUT}} \tag{3.4}$$

where R_W is the resistance of the wire used for the connections, R_C is the contact resistance and R_{DUT} is the device resistance. Unless the condition $R_{DUT} >> R_W+R_C$ holds, it is impossible with a two-point probe system to measure R_{DUT} precisely. In case of tunneling junctions, the tunneling resistance can be high, thus the condition described above is valid.

The problem of parasitic resistances can be solved by using a four-point probe setup, whose circuital scheme is shown in Fig. 3.11 (b). The current path is the same, but the voltage drop across R_{DUT} is measured by a voltmeter on a parallel circuit. Even though also this circuit has wire and contact parasitic resistances, if the voltmeter input impedance is high enough (which typically is the case, since R_{IN}~10^{12} Ω, the current flowing will be negligible and consequently also the voltage drop across the resistances. As a result, the actual measured resistance will be R_{DUT}.

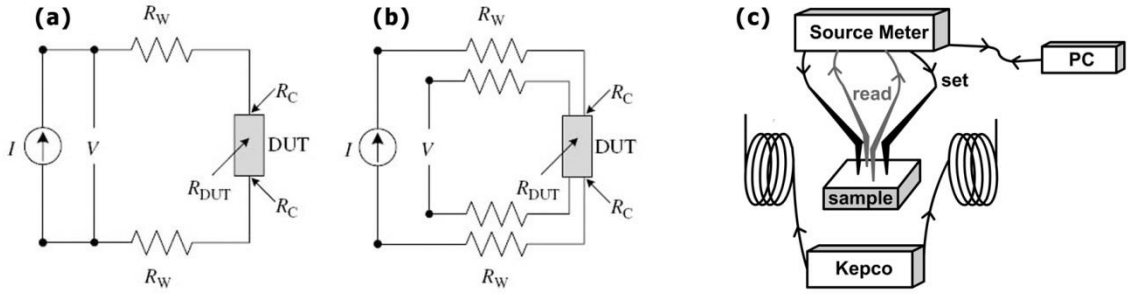

Fig. 3.11 Two-points probe (a) and four-point probe resistivity measurements (b). In (c), sketch of a four point system for TMR mesurements.

Fig. 3.11 (c) shows the sketch of a four point system for TMR measurements. In this case, coils for generating the magnetic field are used. The sample is located in the between the coils, whose current comes from a KEPCO bipolar generator controlled remotely by the PC. Then, a fixed junction voltage is set and the junction current is sensed for different values of applied magnetic field. Both the voltage generation and the current sensing are performed by the same instrument, a Keythley® 2601 source meter. The data are then sent for analysis to a Labview software.

3.8 Thermochemical Nanolithography (TCNL)

Thermochemical nanolithography (TCNL) is a scanning probe technique which employs heated nano-size tips to induce thermally activated chemical reactions and change the chemical functionality of a surface, or obtain new nanostructures. Examples of thermally activated reactions exploited for TCNL are the deprotection of functional groups, the reduction of oxides and the crystallization of amorphous materials.[93–96] TCNL offers the advantage of combining high speed, high resolution, material flexibility, potential towards parallelization, and the versatility of working under ambient conditions.

3.8.1 Instrumentation

TCNL was carried out at Georgia Institute of Technology, Atlanta GA, U.S. in Prof. Elisa Riedo's lab with a modified Agilent system. The system consists of an Agilent® 5500 SPM system (Fig. 3.12 (a)), a National Instruments® NI cDAQ-9178, and the PicoView control software running on a PC computer.

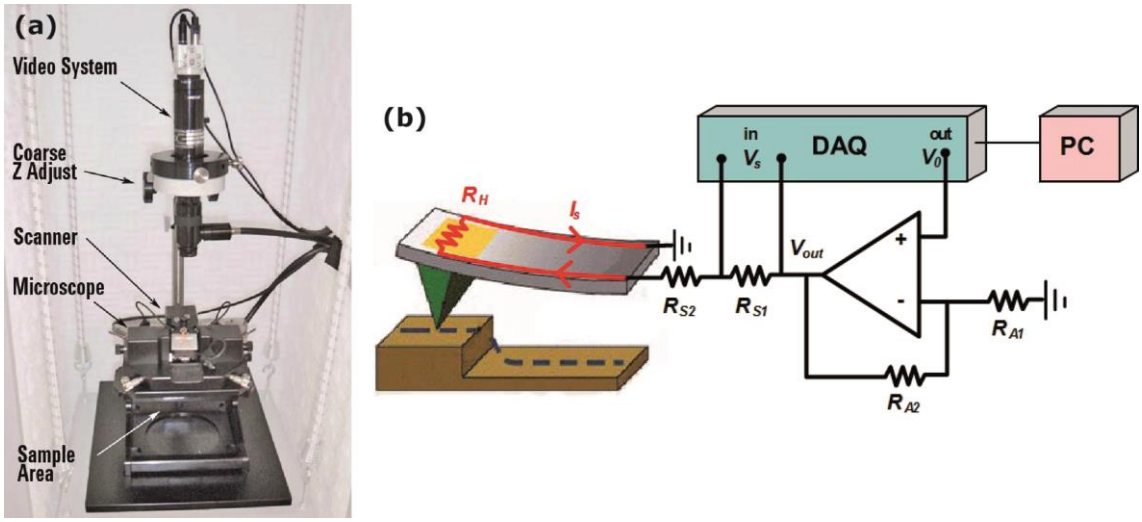

Fig. 3.12 (a) Components of the Agilent 5500 SPM. (b) Sketch of the TCNL system, comprising the AFM, the amplifying circuitry, the DAQ and the PC.

TCNL is able to achieve local chemical modification on surfaces by utilizing a silicon AFM cantilever integrated with a Joule-heating resistive heater (Fig. 3.13). These customized AFM cantilevers were provided by Prof. King's group.[97] They were made using a standard silicon-on-insulator (SOI) process following a documented fabrication process.[98] With the cantilever dimensions and temperature-dependent resistivity, the heater accounts for more than 90% of the electrical resistance of entire cantilever.

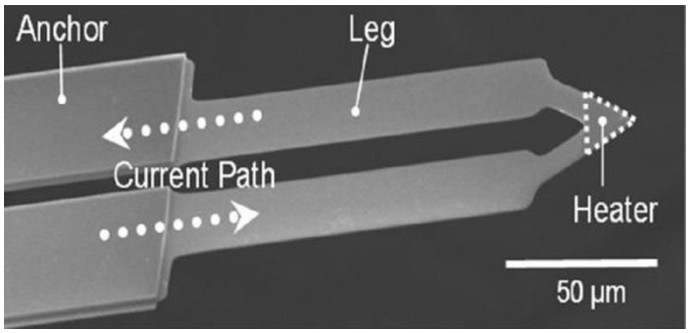

Fig. 3.13 SEM image of a thermal cantilever. From [99].

Fig. 3.12 (b) shows a schematic of TCNL system setup used to operate the heated AFM probe. The DAQ, controlled by the PC, was used both for setting the DC voltage for heating the tip (V_0)

and for sensing the current flowing in the cantilever (I_s). The amplifying circuit consists of a non-inverting operational amplifier, where $R_{A1} = R_{A2} = 10\ \mathrm{k\Omega}$. As a consequence, the output voltage is $V_{out} = 2V_0$. The electric circuit had two sense resistor, $R_{S1} = R_{S2} = 1\ \mathrm{k\Omega}$, connected to the cantilever in series to protect the probe by limiting the current at high power as well as to sense the current (I_s).

In order to pattern desired arbitrary two dimensional geometries, such as arrays lines, triangles or polygons, the PicoScript package was used to enable Matlab scripts in the Agilent PicoView software. The Matlab script was used also to monitor the TCNL process as well as record V_s and V_0. With this instrumentation, the cantilever electrical resistance and power dissipation can be obtained.

3.8.2 Model of thermal conduction

Since the local chemical changes are highly dependent on the activation temperature, precise calibration of heater temperature (T_H, in Fig. 3.14 (a)) is essential for controlling the surface reactions. The electrical resistance of the heater (R_H) varies nonlinearly with temperature and significant temperature gradients can exist in the whole cantilever.

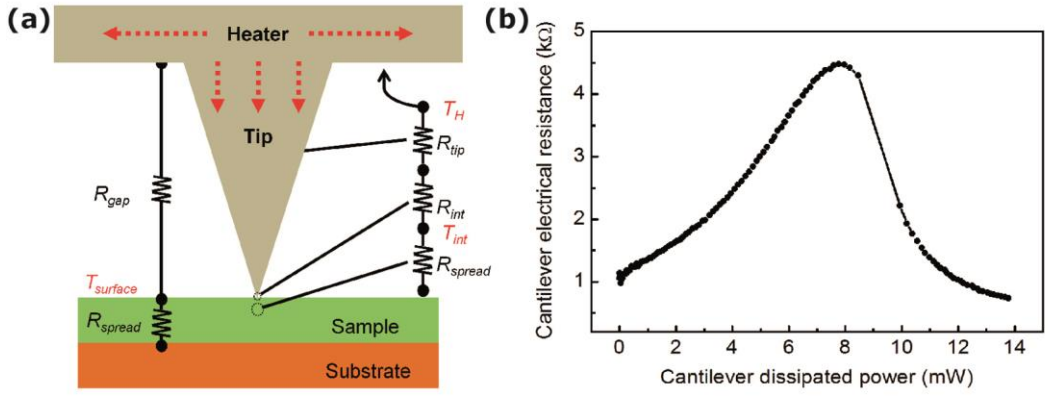

Fig. 3.14 (a) Thermal circuit for heat flow of a heated TCNL thermal cantilever, the tip, and the contact with sample. (b) Variation of the electrical resistance of a TCNL integrated heater as a function of dissipated power. Competition between increased electron scattering and intrinsic carrier generation at elevated temperatures results in a peak resistance of 4.5 kΩ at 550° C, where P_H = 7.9 mW. Adapted from [100].

The electrical resistivity of doped silicon is a strongly dependent on temperature. Fig. 3.14 (b) shows the variation of R_H with dissipated power of the heater (P_H) of a typical TCNL thermal cantilever. R_H and P_H values can be obtained by: $R_H = \frac{2R_{s1}}{V_s}(V_0 - V_s)$ and $P_H = \frac{2V_s}{R_s}(V_0 - V_s)$, where V_0 is the voltage generated by the DAQ, V_s and R_{s1} are the voltage drops and resistance of the sense resistor (Fig. 3.12 (b)). As shown in Fig. 3.14 (b), the cantilever had a room temperature resistance near 1.2 kΩ, which could increase with temperature to a peak resistance of 4.5 kΩ at 550° C, where P_H = 7.9 mW. Near room temperature, the cantilever

resistance increases with temperature, since the carrier mobility in the doped silicon cantilever decreases with temperature. However, the intrinsic carriers in the silicon increase with increasing temperature. At approximately 550° C (intrinsic temperature, T_i), the thermally generated intrinsic carriers become the dominant parameter affecting the cantilever resistance, and the resistance decreases sharply. This thermal runaway effect has been well studied for cantilever heating at steady state.[101,102] Due to the thermal runaway at higher power levels, the heated cantilever can have the same electrical resistance at two different heater temperatures, which precludes the use of resistance monitoring for temperature measurements. Therefore, using cantilever power as a measure of temperature has advantages over the resistance due to its one-to-one correspondence.

A linear relationship between the heater temperature T_H and the power P_H can be identified:[100]

$$T_H = RT + \frac{T_i - RT}{P_i} P_H \tag{3.5}$$

Where RT is the room temperature, P_i is the cantilever power at intrinsic temperature T_i. The cantilever temperature characteristic was calibrated before each TCNL operation.

During a TCNL thermal process, the temperature rise at the tip-sample-surface interface (T_{int}) is the critical parameter to consider. The difference between T_{int} and T_H depends on the thermal resistances of a number of components within the tip-sample system, as shown in Fig. 3.14 (a). The tip-sample thermal circuit system includes thermal resistances of the tip (R_{tip}), tip-surface interface (R_{int}), and sample spreading resistance (R_{spread}). Heat also flows directly from the cantilever heater to the substrate through the ambient air, with thermal resistance R_{gap}. The dominant mode of heat transfer is through the ambient air, as R_{gap} is approximately one order of magnitude smaller than the total thermal resistance through the tip. However, the temperature rise on the sample surface due to the heat transfer through air, $T_{surface}$, is controlled by the thermal conductivities of ambient air and sample, and thus $T_{surface} \ll T_{int}$. This makes the TCNL thermal cantilever-tip an attractive instrument for performing highly localized thermal processing.

Considering the thermal conductivities of the Si substrate/Polymeric material system which will be employed in this thesis (section 8), it is possible to calculate the heat efficiency parameter *c* defined as:

$$c = \frac{T_{int}}{T_H} = \frac{R_{spread}}{R_{tip} + R_{int} + R_{spread}} \sim 0.6 \tag{3.6}$$

For details on the calculation of the heating efficiency see Ref [100].

3.8.3 Controlling TCNL: writing kinetics model

Thermochemical nanolithography, in the work presented in chapter 8, was exploited for patterning protein gradients with sub-micron resolution. For doing so, a polymer synthesized by Professor Seth R. Marder's lab at Georgia Institute of Technology was used as a substrate in the TCNL process. Synthesis and chemical preparation of the polymer is described elsewhere.[95] The chemical structure of the polymer, (poly((tetrahydropyran-2-yl N-(2-methacryloxyethyl)carbamate)-co-(methyl 4-(3-methacryloyloxypropoxy)cinnamate))), is shown in Fig 3.15.

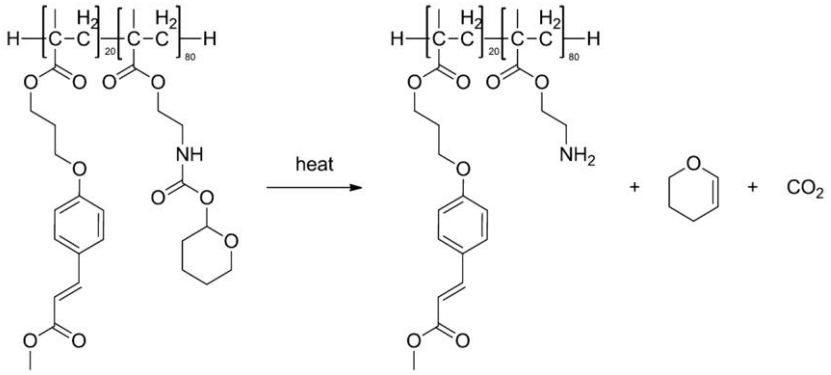

Fig 3.15 Thermal reaction for the Cinnamate Polymer. From [103].

The polymer has a protected functional amine group; when heated, the protection group dissociates, leaving behind an exposed functional group to which various complementary chemical groups can be attached.[95] The dissociated groups (gaseous CO_2 and dihydropyran) are volatile enough that more than likely they diffuse away.[104] To ensure the polymer substrate structure remains intact, the polymer's glass transition temperature is increased with an increased UV induced cross-linking between the polymer's cinnamate side chains.[95] This deprotection can be performed with a hot AFM tip maintained above T_d (between 150° C and 220°C), thus exposing amine groups.

It was demonstrated, both theoretically and experimentally, that it is possible to achieve a great degree of control over the concentration of the deprotected amines by tuning properly the TCNL parameters, such as the heater temperature and the tip scanning speed.[104] Such control can be used for patterning concentration gradients of exposed amines on the polymer, which can be then exploited for immobilizing properly functionalized biomolecules.

Fig. 3.16 (a) shows the fluorescence intensity of 5x5 μm^2 amine TCNL patterns realized with different heating power, incubated with amine reactive dye. Due to the low dye concentration, the fluorescence intensity is roughly proportional to the exposed amine density.[105] Fig. 3.16 (b) shows the fitting of the fluorescent intensity with a model which makes use of the Arrhenius

equation for expressing the temperature dependence of the deprotection reaction rate. For details on the model, see Ref [104].

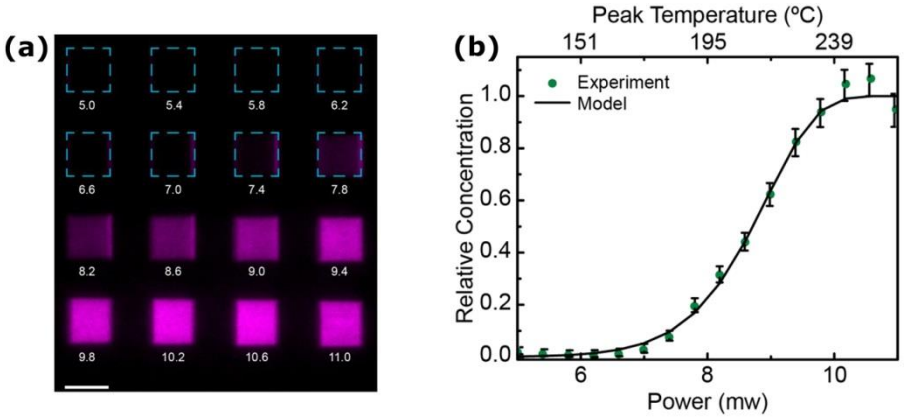

Fig. 3.16 (a) 5x5 μm^2 square patterns imaged by an amine reactive dye. For each patter, the heater dissipated power is indicated. (b) Fluorescence intensity and fit with the theoretical model. Adapted from [104].

4. Realization of an MTJ-based magnetic biosensing setup

In this section, the realization of a magnetic biosensing setup for detecting biomolecular recognition events is presented, starting from the optimization of the sputtering deposition of each functional layer of the sensor, up to the final integration of the devices in a microfluidic environment and electronics for data acquisition. All the steps of this work, which were carried out at the L-NESS center in Como, are listed below:

- Optimization of the sputtering deposition of each functional layer of the sensor.
- Deposition of the sensor stacks by magnetron sputtering.
- Microfabrication of the sensor arrays by optical lithography and ion beam etching, and deposition of the electrical contacts by electron beam evaporation.
- Thermal annealing and characterization of the sensors.
- Integration of the sensor arrays in a microfluidic system and the electronics for data acquisition.

4.1 Sensor Layout

In Fig. 4.1, the optimized sensor stack comprising 11 layers with different functionalities is sketched. Each one of the 4 functional elements is highlighted: buffer layers, exchange biased synthetic antiferromagnet, magnetic tunneling junction and capping layer.

Buffer and capping. The Ta/Ru/Ta buffer trilayer and the Ta/Ru capping are crucial for optimizing the crystallization of the CoFeB junction layers; in particular, a correct design of the buffer layer favors the crystallization of the bottom CoFeB layer, which is also influenced, other than by the texturation of the MgO barrier, by the crystalline structure of other underlying layers such as the pinning antiferromagnet.[106] Indeed, such a structure gives rise to a strong [111] texture of IrMn, which also induces an improvement of the exchange bias of CoFeB.[107] The capping layer, on the other side, promotes the top CoFeB layer crystallization.[108] Therefore, the optimization of thickness and deposition conditions of buffer and capping layers is crucial for having high TMR values.

Exchange Biased synthetic antiferromagnet. In conventional exchange biased MTJs, the bottom layer magnetization is pinned by exchange interaction with an antiferromagnet, so that it acts as a fixed reference in contrast with the top layer magnetization which is free to

follow the external field. In this system the pinning of the bottom layer is achieved through synthetic antiferromagnet (SAF); in fact CoFeB bottom layer is pinned antiferromagnetically to CoFe through a Ru spacer by bilinear coupling. The CoFe is in turn directly pinned by exchange bias with an antiferromagnet. IrMn is used as antiferromagnet because it provides both high exchange bias magnitudes and good thermal stability.[109] There are three major advantages for using a SAF pinned layer; first of all, it significantly reduces the stray field from the pinned layer, which acts as an undesirable extra external field on the free layer altering the response of the sensor; secondly, it enhances the pinning of the bottom layer and finally it improves the sensor's thermal stability because the Ru layer acts as a barrier against Mn interdiffusion.[110]

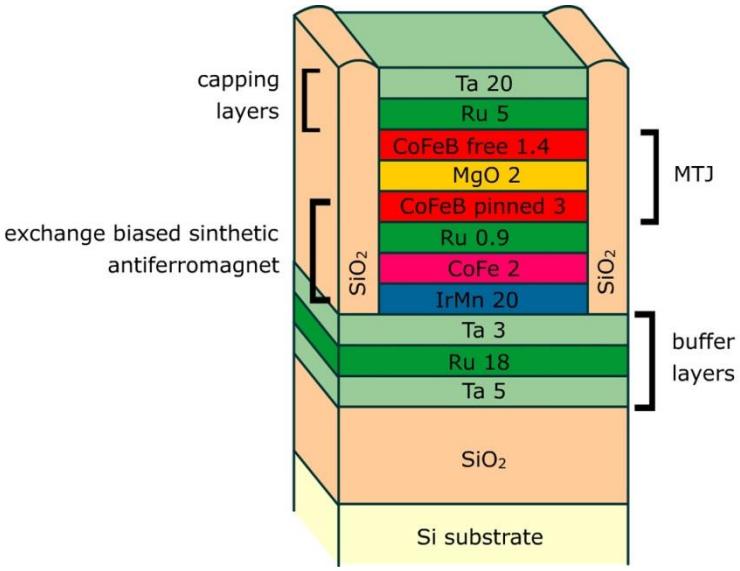

Fig. 4.1 Structure of the sputtered sensor stack after lithographic patterning, highlighting the functional elements. Thicknesses in nm.

MTJ element. As explained in chapter 2.2, CoFeB/MgO/CoFeB junctions give rise to the highest TMR at room temperature in sputtered systems due to the coherent tunneling transport across the junction. In such systems, post growth thermal annealing is crucial for enabling the correct crystallization of the junction.

4.2 Controlling the sensor response

One of the most important issues in designing TMR sensors is controlling the response of the sensor, i.e. the change in the resistance of the sensor $R(H)$ with respect to the external magnetic field H. Obviously, since the magnetization of the bottom magnetic layer is pinned and thus insensitive to the external magnetic field, this issue is strongly related to the magnetic response of the free layer.

In most cases, a linear sensor response with low hysteresis is favorable for sensing applications because it enables a straightforward relationship between changes in the external magnetic field and changes in the electric signal acquired from the sensor.

One way for achieving linearization is to exploit the superparamagnetic behavior of ultrathin magnetic layers. Indeed, the magnetic response of the free layer changes rapidly as its thickness decreases. In the case of CoFeB, a linear and hysteresis-free switching is obtained when the CoFeB free layer thickness is thinner than a critical thickness of 1.5 nm. The main drawback of using such thin free layers is the strong reduction of the total magnetic moment and of the TMR effect.[89] For this reason, an ultra-fine control of the layer thickness (around 1 Å) is crucial for choosing the best trade-off between linearity, coercivity and sensitivity.

Another way to achieve linearization, which we will treat theoretically in the following paragraphs, exploits the magnetocrystalline and shape anisotropy of the free layer.[111,112] In our experimental work, we will adopt a solution which combines the superparamagnetic behavior of thin CoFeB layer and shape anisotropy for controlling the sensor response.

Jullière-like model for non-collinear magnetizations. Let us consider a MTJ where the magnetizations of the two layers are not collinear, i.e. they form an angle $\theta \neq \pi$. In such systems, one can generalize Jullière's expression Eq. (2.5) for tunneling conductance to the case of non-collinear magnetizations:

$$G(\theta) = G_P + (G_{AP} - G_P)\sin^2\frac{\theta}{2} \tag{4.1}$$

Assuming small TMR ratios, one obtains the dependence of the junction resistance $R(\theta)$ on the angle θ between the magnetizations of the two layers:

$$R(\theta) \sim \frac{R_P + R_{AP}}{2} + \frac{R_P - R_{AP}}{2}\cos\theta = R_\perp + \frac{\Delta R}{2}\cos\theta \tag{4.2}$$

It is worth noting that the resistance is linear with respect to $\cos\theta$.

Through energy terms calculations, it is possible to study the dependence of the angle between the magnetizations on the external applied field. From Eq. (4.2), it is clear that a linear relation between $\cos\theta$ and the external field would imply a linear magnetic field response of the sensor. The magnetic response of the free layer in terms of magnetic energy contributions is described theoretically in the following paragraph.

Modeling the free layer. Let us consider the layer shape in Fig. 4.2, where both pinned and free layers have the easy axes induced by the magnetocrystalline anisotropy along the short edge of the rectangle. This is a condition often fulfilled in sputtered films, where it is possible

to control the magnetocrystalline anisotropy by applying a magnetic field during the growth; doing so, an easy axis is created along the magnetic field direction.

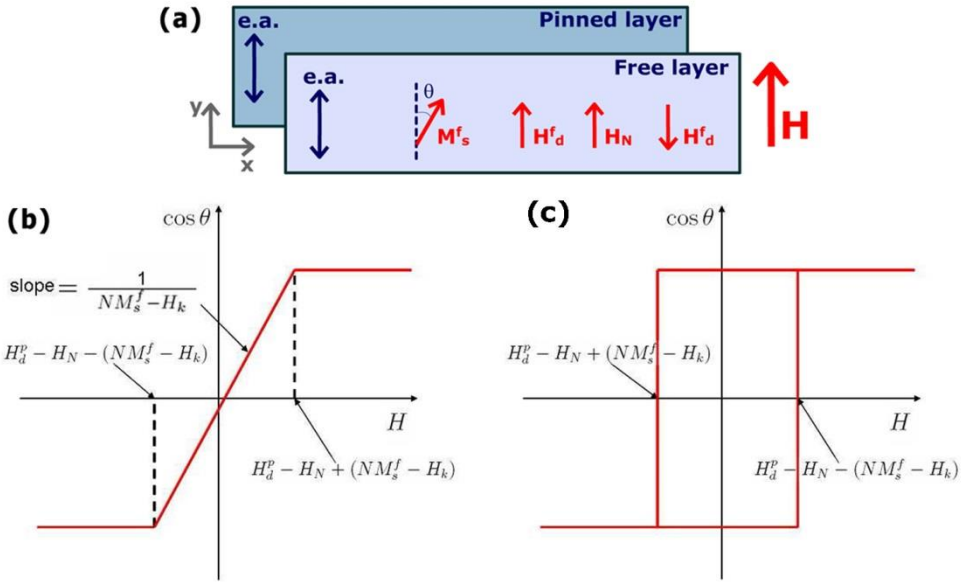

Fig. 4.2 (a) Sketch of rectangular-shaped pinned and free layers with parallel magnetocrystalline anisotropies. "e.a." indicates the easy axis directions. (b) free layer response curve if $H_k < N \cdot M_s^f$, the response is linear and shows no hysteresis; (c) if $H_k > N \cdot M_s^f$, the response is hysteretic. Adapted from [113].

The total energy of the free layer can be written as the sum of many contributions:

$$E_f \sim \underbrace{-\mu_0 \mathbf{H} \cdot \mathbf{M_s^f}}_{\text{Zeeman}} \quad \underbrace{+K \sin^2\theta}_{\text{magnetocrystalline anisotropy}} \quad \underbrace{-\frac{1}{2}\mu_0 \mathbf{H_d^f} \cdot \mathbf{M_s^f}}_{\text{demag. field of free layer}} \quad \underbrace{-\mu_0 \mathbf{H_d^p} \cdot \mathbf{M_s^f}}_{\text{demag. field of pinned layer}} \quad \underbrace{-\mu_0 \mathbf{H_N} \cdot \mathbf{M_s^f}}_{\text{Néel coupling}} \tag{4.3}$$

where $\mathbf{H}$ is the external applied field, $\mathbf{M_s^f}$ is the saturation magnetization of the free layer, $\mathbf{H_d^f} = N \cdot M_s^f \cos\theta\, \mathbf{j}$ is the demagnetizing field of the free layer, $\mathbf{H_d^p}$ is the demagnetizing field of the pinned layer, and $\mathbf{H_N}$ is the Néel coupling field. *K* is the magnetocrystalline anisotropy constant and is related to the anisotropic field by $H_k = 2K/(\mu_0 M_s^f)$.

The following minima in the energy and thus the stable magnetic configuration for each value of external field are obtained setting $\frac{\partial E_f}{\partial \theta} = 0$ and $\frac{\partial^2 E_f}{\partial \theta^2} > 0$:

$$\text{if} \quad H_k > N \cdot M_s^f \Rightarrow \begin{cases} \theta = 0, & H > H_0 \\ \theta = \pi, & H < H_\pi \end{cases}, \quad \text{hysteretic behaviour} \tag{4.4}$$

$$\text{if} \quad H_k < N \cdot M_s^f \Rightarrow \begin{cases} \theta = 0, & H > H_0 \\ \cos\theta = \frac{H - H_p^d + H_N}{N M_s^f - H_k}, & \text{linear behavior} \\ \theta = \pi, & H < H_\pi \end{cases} \tag{4.5}$$

Where $H_{\pi(0)} = H_d^p - H_N + (-)(N \cdot M_f^S - H_K)$. Fig. 4.2 shows the response curve is both linear (b) and hysteretic (c) cases. It is worth noting that the Néel field and the demagnetizing field of the pinned layer ($H_d^p - H_N$) shift the curve, while the competing effects of the shape anisotropy and the magnetocrystalline anisotropy ($N \cdot M_f^S - H_K$) determine the shape and the limits of the curve. In fact, the shape anisotropy favors an alignment parallel to the long edge of the rectangle, whereas the magnetocrystalline anisotropy induces an easy axis along the short edge.

In conclusion, it is possible to identify the conditions for linearity and to relate intuitively the magnetic properties of the pinned and free layer to the sensor's performances; in case of linear response, the dynamic range of the sensor is given by the distance between H_0 and H_π, while the sensitivity is related to the slope of the curve and to the value ΔR in Eq. (4.2).

The solutions are valid under the assumption that the free layer is a single magnetic domain and thus the magnetization rotates uniformly with the external field. In layers with small lateral dimensions (< 500 nm) this is a good assumption because the energy cost of domain formation is too high and the layers will be essentially "single domain". For larger areas, these results should be treated carefully, and integrated with specific micromagnetic simulations for providing more reliable results.

4.3 Fabrication of MTJ-based sensor arrays

Before growing the whole sensor stack, the deposition conditions of each functional layer were optimized in terms of low surface roughness and uniform topography. IrMn/CoFeB exchange biased bilayers and IrMn/CoFe/Ru/CoFeB synthetic antiferromagnet structures were subsequently studied for maximizing the magnetic coupling, optimizing the thickness of the functional layers and the field cooling process.

The AJA Orion8 magnetron sputtering system described in section 3.1 was used for depositing both the test and the sensor structures.

The Si/SiO_2 substrates were cleaned with acetone, IPA and Piranha solution (H_2O_2, H_2SO_4 7:1). Before depositing the sensor stack, the substrates underwent a soft etch in vacuum (10 minutes at 30W in RF mode, Argon pressure of 2mTorr) in the same sputtering system, for removing contamination from the exposition to air. After the deposition of the sensor stack,

the junctions were patterned by multiple steps of optical lithography and ion milling. The patterned sample was then provided with electrical contacts addressing independently each sensor, which consist of a Cr/Au bilayer deposited by evaporation in a Leybold system. Finally, the sensors underwent a thermal annealing process in a magnetic field, for allowing the correct crystallization of the layers and for setting the exchange bias direction in the synthetic antiferromagnet structure and pinning the magnetization of the bottom layer.

4.3.1 Sputtering growth and optimization of the functional elements

Growth conditions. The sensor layers were deposited with a $2 \cdot 10^{-9}$ Torr base pressure. CoFe and MgO layers were deposited in RF mode, while all other layers were deposited in DC mode. During deposition, a 30 mT magnetic field was applied in-plane with respect to the sensor surface, for determining the direction of the magnetocrystalline anisotropy in the CoFeB layers. The optimized sputtering growth conditions for each layer are summarized in Table 4.1. The RMS roughness values were calculated from a 1 µm x 1 µm AFM topography image of a single layer of the selected material grown on Si/SiO_2 substrate.

Table 4.1 Optimal sputtering growth conditions for each layer and RMS roughness values measured by AFM.

Layer	Ar pressure (mTorr)	Target Power (W)	Dep. Rate (Å/min)	RMS Roughness (Å)
Ta	3	100 DC	38.5	0.8
Ru	3	50 DC	21.5	0.8
IrMn	3	50 DC	16.8	1
CoFe	12	200 RF	19.5	-
CoFeB	3	58 DC	11.8	0.8
MgO	2	220 RF	1.6	2.5
SiO_2	2	200 RF	12.5	10
Al_2O_3	3	50 RF	4.84	-

After the optimization of the deposition of single layers, Ta 3/Ru 18/Ta 5 (thicknesses in nm from now on) buffer layers and CoFeB 3/MgO 2 bilayers were grown on Si/SiO_2 substrates and characterized by AFM as previously described. The surface resulted smooth and the RMS roughness (2.5 Å and 0.8 Å, respectively) was comparable to the one measured on the single layers. Low surface roughness and smooth interfaces are crucial requirements of the buffer layers for promoting the correct crystallization of the upper layers, and in the CoFeB/MgO layers for ensuring a high quality of the tunneling barrier and a low Néel coupling between the ferromagnetic electrodes of the junction. Fig. 4.3 (a) shows the AFM topography image of a 2 nm MgO layer grown on SiO_2. The smooth surface and low RMS roughness value (0.8 Å) are prerequisites for high quality and pinhole-free tunneling barriers.

Exchange bias. Exchange bias in IrMn/CoFeB and IrMn/CoFe bilayers was studied as a function of the IrMn thickness and field cool temperature aiming to maximize the exchange coupling and thermal stability. Samples with increasing IrMn thickness from 8 nm to 20 nm were grown on Ta/Ru/Ta buffer layers. The best condition in terms of exchange bias value and thermal stability was achieved in of Ta 5/Ru 18/Ta 3/IrMn 20/CoFe 2/Ru 1.3, where the shift in the hysteresis loop after 300°C field cooling is $\mu_0 H_{ex} \sim 33$ mT (inset of Fig. 4.3 (b), measured by MOKE in longitudinal configuration), which is sufficiently large for our applications.

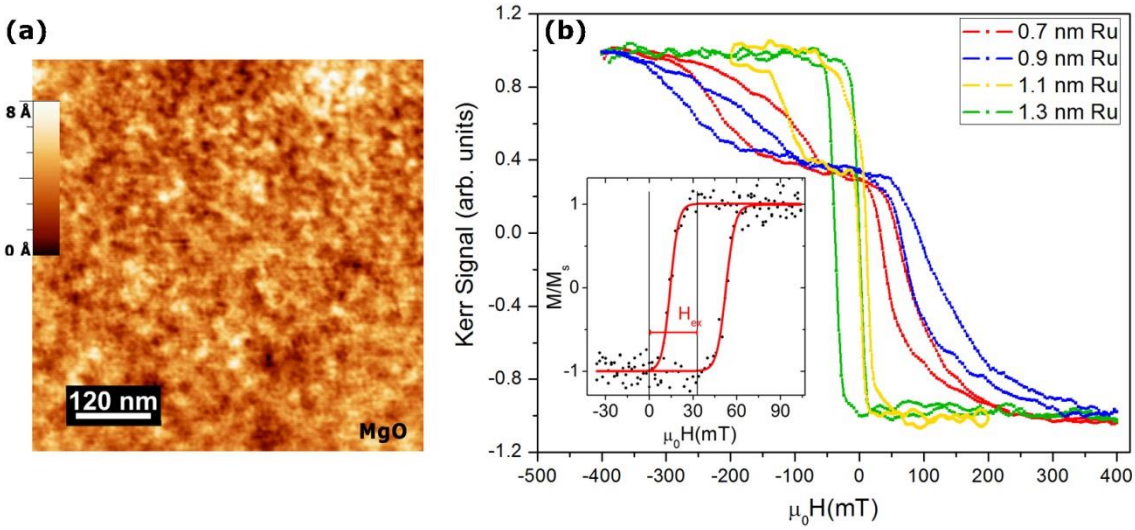

Fig. 4.3 (a) AFM topography image of a 2 nm MgO layer grown by sputtering in the optimized conditions (Table 4.1). (b) Hysteresis loops along the easy axis direction in Ta 5/Ru 18/Ta 3/IrMn 20/CoFe 2/Ru *x*/CoFeB 3 SAF heterostructures with different Ru thicknesses; the loop separation, proportional to the bilinear exchange coupling, is observed to be 100 mT in the structure with 0.9 nm Ru after a 300°C 1 h field cooling. In the inset, exchange biased hysteresis loop of the CoFe layer in a Ta 5/Ru 18/Ta 3/IrMn 20/CoFe 2 system after a 1 h field cooling starting from 300°C. The hysteresis loops were measured by MOKE in the longitudinal configuration.

Synthetic antiferromagnet. As pointed out before, maximizing the antiferromagnetic coupling between CoFe and CoFeB layers in the synthetic antiferromagnet (SAF) structure is fundamental for pinning the magnetization of the bottom layer of the junction, and for providing thermal stability to the structure during the thermal annealing process. The interlayer magnetic coupling between the CoFe and CoFeB layers was studied as a function of the Ru thickness and the field cooling temperature. Fig. 4.3 (b) shows the hysteresis loops of Ta 5/Ru 18/Ta 3/IrMn 20/CoFe 2/Ru *x*/CoFeB 3 heterostructures measured by MOKE in longitudinal configuration after a 300° C 1h thermal annealing in a 0.4 T magnetic field applied in the direction of the measurement; *x* corresponds to 7, 9, 11, 13 Å. The shift between the two loops is related to the bilinear coupling between the layers.[114] Increasing the Ru layer thickness, we observe a behavior compatible with the oscillatory nature of the coupling which is antiferromagnetic for t_{Ru} =7, 9, 11 Å, with a maximum shift around 100 mT for t_{Ru}=9 Å. For t_{Ru}

=13 Å, the coupling becomes ferromagnetic, as expected: thus we observe a single hysteresis loop. From this analysis it turns out that the strongest antiferromagnetic bilinear coupling is achieved for 0.9 nm of Ru.

4.3.2 Microfabrication of the sensor arrays

The microfabrication of the sensors is a multistep procedure which involves 3 opto-lithographic processes, 2 ion milling steps, a sputtering deposition and an electron beam evaporation process of the electrical contacts.

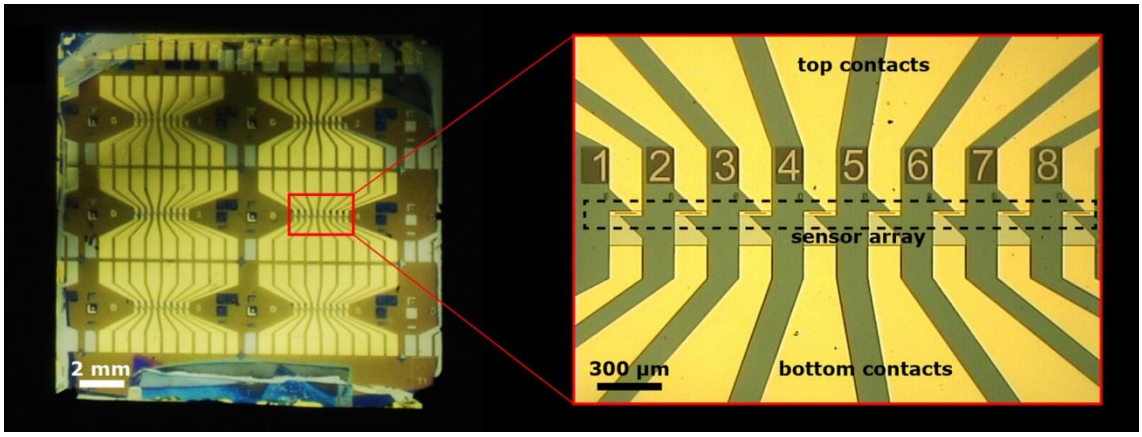

Fig. 4.4 Left panel: sensor chip after the microfabrication process. 6 sensor arrays with 8 sensors each are present. Right panel: an array of 8 MTJ sensors; top and bottom contact address independently each junction.

The final layout of the sensor chip is shown in Fig. 4.4. On a 2 cm x 2 cm Si/SiO_2 sample, 6 arrays with 8 MTJ-based sensors were fabricated. The top and bottom contacts address independently each sensor, for allowing independent measurements and/or the exclusion of any sensor from the measurement in case of malfunction. MTJs with different rectangular shapes with high aspect ratio were fabricated; the high aspect ratio allows to set a magnetic easy axis along the long edge of the junction. This shape anisotropy, combined with superparamagnetism due to the reduced thickness, is exploited for linearizing and reducing the hysteresis in the magnetic response of the free layer. The exchange bias direction is set along the short edge of the sensor.

In the next paragraphs the lithographic process will be described in detail.

After depositing the multilayer sensor stack on a Si/SiO_2 substrate, the steps for fabricating the sensor are the following:

- Definition of the MESA and of the bottom contacts (*mask 1*).
- Definition of the junction geometry (*mask 2*).
- Definition of the electrical contacts (*mask 3*) and contact deposition.

Definition of the MESA. The definition of the MESA (which consists in a structure in relief which includes the junction area and the bottom contacts area) involves a direct lithographic process and an ion milling. First, the sample is cleaned with Acetone and IPA. Then the photoresist is spin-coated on the sample and the sample is pre-baked on a hot plate. Subsequently, the sample is exposed with *mask 1* and it is developed. Then, the ion milling defines the MESA, etching until the SiO_2 substrate and finally the resist is stripped. Fig. 4.5 shows the mask and an optical microscope image of the lithographed structure. Two different widths of the bottom layer were tested: $x_M = 20, 40$ µm. In Table 4.2, the optimized parameters of this step are listed:

Table 4.2 Optimized parameter of the MESA definition step.

Step	Parameter
Spin coating & baking	AZ5214E resist 1.4 µm thick, baked at *T*=110° C, for 1'30"
Exposure (*mask 1*)	Exposure dose = 128 mJ/cm^2
Development	35" in pure AZ726MIF
Ion milling	V_{dis}=200 V, V_{acc}=600 V
Stripping	AZ100 remover at *T* = 100° C

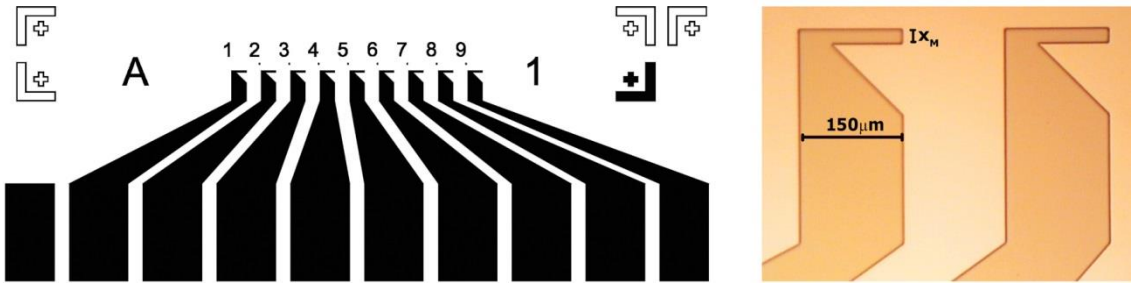

Fig. 4.5 MESA definition. Left panel: mask 1 is shown. Right panel: optical microscope images of 2 patterned structures. The bottom contact width $x_M = 20$ µm.

Definition of the junction geometry. In this step, the actual shape and area of the sensor is defined carving a pillar in the MESA. Rectangular junctions with different sizes were fabricated: 2x100 µm^2, 3x150 µm^2, 2.5x120 µm^2, 2.5x30 µm^2 and 2.5x50 µm^2. The process, which involves a direct lithography process, and a ion milling, is the following: after cleaning, spincoating and pre-baking, the sample is exposed with *mask 2* and is developed. The subsequent etching procedure is crucial for the sensor functionality. The pillar must be carved until the end of the IrMn layer; over- or under-etching can result in a too high resistance of the bottom contact or in shortcuts between the top and bottom contact, respectively.

Fig. 4.6 shows the mask and an optical microscope image of the lithographed junctions. In Table 4.3, the optimized parameters of this step are listed.

Table 4.3 Optimized parameters of the junction definition step.

Step	Parameter
Spin coating & baking	AZ5214E resist 1.4 µm thick, baked at *T*=110° C, for 1'30"
Exposure (*mask 2*)	Exposure dose = 128 mJ/cm^2
Development	40" in pure AZ726MIF
Ion milling	V_{dis}=200 V, V_{acc}=600 V
SiO_2 deposition	100 nm opt. cond. (Table 4.1)
Lift-off	AZ100 remover at *T* = 100° C

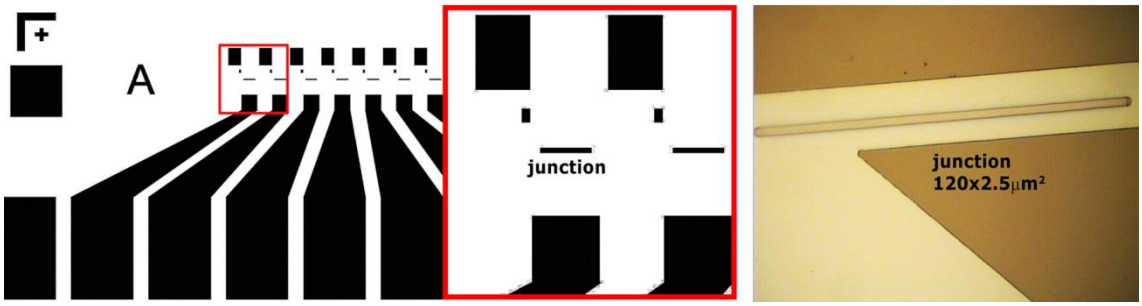

Fig. 4.6 Junction geometry definition. Left panel: mask 2 is shown. Right panel: optical microscope image of the resist pattern of a 2.5x120 µm^2 junction.

Ion beam etching, in this step, is performed tilting the sample at different angles (30° and subsequently 60° with respect to the beam direction), in order to avoid redeposition of the etched material and defining sharper sensor shapes.

After the etching, a 100 nm SiO_2 insulating layer is deposited around the junction (as shown in Fig. 4.1) by sputtering. The purpose is to electrically insulate the bottom contacts from the top contacts and to reduce the junction resistance acting against the surface defects and terminating the dangling bonds. When the resist is stripped, the bottom contacts and the junction area are exposed for the subsequent contact definition step.

Definition and deposition of the electrical contacts. In this step, the contact area for the subsequent evaporation of the metal contacts are defined. At the end of this last inverse lithographic process, the whole sample is covered by resist except for the contact areas. In inverse lithography, the primer is cast on the sample for promoting the resist adhesion. Before the contact deposition, the sample undergoes a 30' soft etching in vacuum for removing the residues of resist from the junction area. The Cr 7/Au 300 contact bilayers are e-beam evaporated in a Leybold system. The thin chromium layer favors the adhesion of Au to the

underlying surface. Fig. 4.7 shows *mask 3* used for defining the contact areas, and the patterned samples before evaporation. The optimized parameters are listed in Table 4.4:

Table 4.4 Optimized parameters of the contact definition step.

Step	Parameter
Primer coating & baking	2' at *T*=120° C
Resist coating & baking	AZ5214E resist 1.4 µm thick, 1'30'' *T*=110° C
Exposure (*mask 3*)	25.4 mJ/cm^2
Reversal baking	1'40'' *T*=117° C
Flood exposure	254 mJ/cm^2
Development	20'' in pure AZ726MIF
Contact evaporation	Cr 7/Au 300
Lift-off	AZ100 remover at *T*=100° C

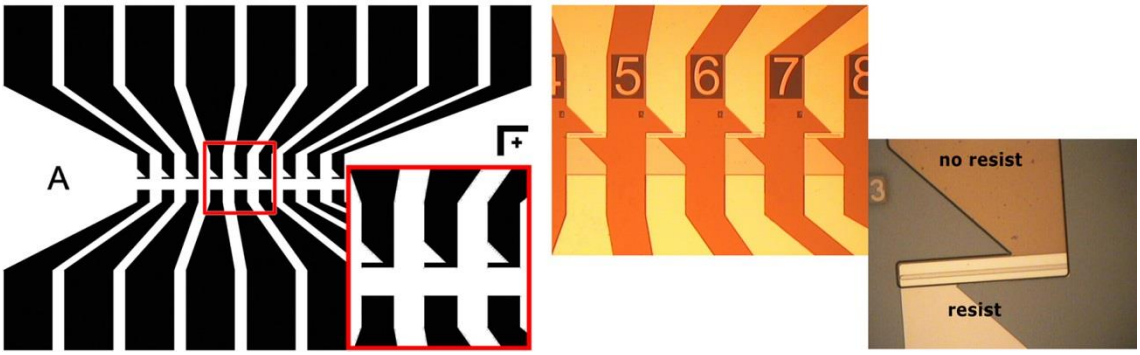

Fig. 4.7 Contact area definition. Left panel: mask 3 is shown. Right panel: optical microscope images of the patterned structures before the contact deposition.

Fig. 4.8 shows a 3D view of a sensor after the microfabrication process. The top pads are in ohmic contact with the top CoFeB electrode of the MTJ, while the bottom pads, deposited on the MESA, provide the contact with the bottom CoFeB electrode by tunneling through MgO. Because of its large area, the MESA structure is likely to have a larger number of defects with respect to the MTJ, thus the current finds conductive paths which make the bottom contact resistance negligible with respect to the junction one.

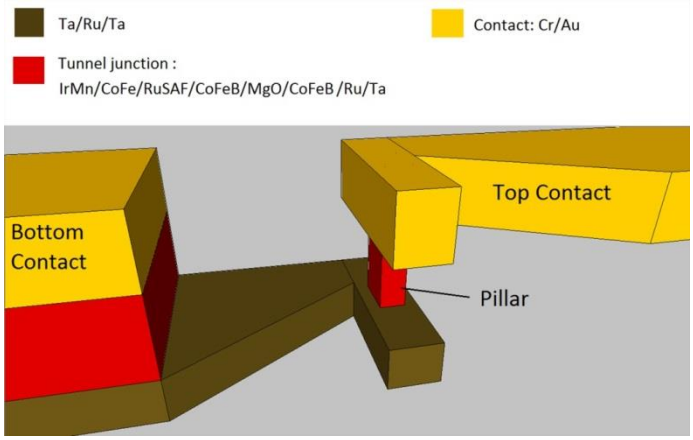

Fig. 4.8 3D image of a sensor after the contacts deposition.

4.3.3 Thermal annealing and sensor characterization

The last step in the sensor fabrication consisted in a 1 h thermal annealing in vacuum (~ 10^{-6} Torr) applying a 0.4 T static magnetic field in the system described in section 3.4. This ensures the crystallization of the junction layers, and in particular of the CoFeB electrodes, which leads to a significant increase of the TMR ratio. Furthermore, the exchange bias is set in the direction of the magnetic field during the field cooling. The following sensor structure was employed: Ta 5/Ru 18/ Ta 3/IrMn 20/CoFe 2/Ru 0.9/CoFeB 3/MgO t_{MgO}/CoFeB t_{fr}/Ru 5/Ta 20. Where t_{MgO} and t_{fr} are the thicknesses of the MgO barrier and the free CoFeB electrode, respectively. As shown in the next paragraph, by tuning properly these two parameters and the junction dimension, it is possible to control the junction resistance and the shape of its magnetoresistive curve, for matching the sensor performances to the specific experiment.

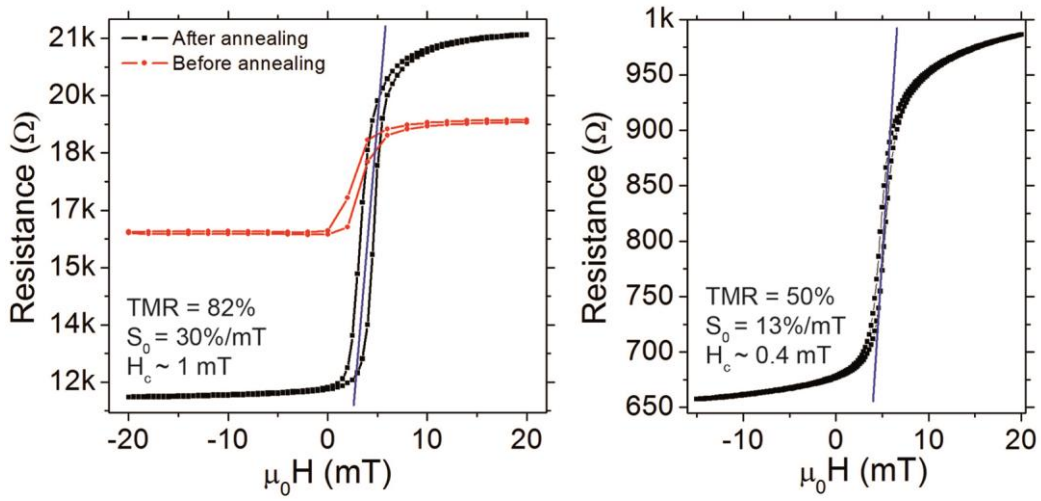

Fig. 4.9 Left panel: TMR curve of a 2.5x30 μm² junction with t_{MgO}=2 nm and t_{fr}=1.4 nm, before and after a 300°C thermal annealing.

Fig. 4.9 (a) shows the magnetoresistive curve of a 2.5x30 μm^2 junction with t_{MgO}=2 nm and t_{fr}=1.4 nm, before and after a 300°C thermal annealing. In this case, the sensor was optimized focusing on the sensor sensitivity. The TMR value increases from 18% to 82% after the thermal annealing. The curve is slightly hysteretic with a coercive field $H_C \sim 1\ \mathrm{mT}$. From the slope of the curve in the linear region, it is possible to define the *low-field sensitivity* $S_0 = \frac{1}{\mu_0 R}\frac{dR}{dH} \sim 30\ \frac{\%}{\mathrm{mT}}$, which is the percent variation of the resistance of the sensor per unit variation of external magnetic field, which is in line with current state of the art MTJ-based sensors.[26]

Fig. 4.9 (b) shows the magnetoresisive curve of a 2.5x120 μm^2 junction with t_{MgO}=2 nm and t_{fr}=1 nm after a 330°C thermal annealing. In this case the sensor was optimized focusing on linearity and low hysteresis; in fact, the superparamagnetism of the free layer, due to its reduced thickness, leads to a low coercivity $H_C \sim 0.4\ \mathrm{mT}$, a less steep curve, and a TMR $\sim 50\%$. The combination of these factors lead to a low-field sensitivity $S_0 = 13\ \frac{\%}{\mathrm{mT}}$.

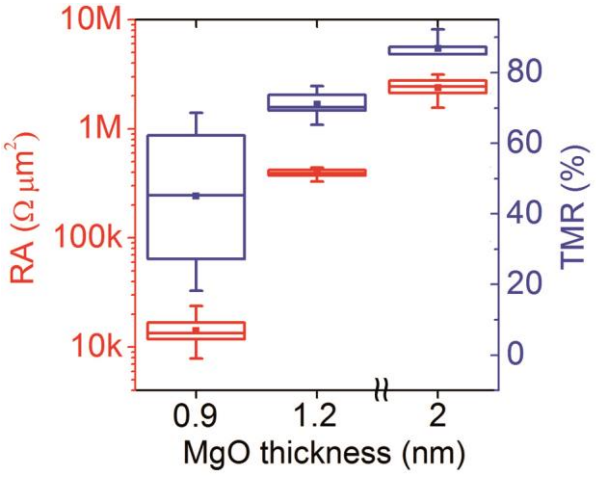

Fig. 4.10 statistical analysis of TMR and RA values for the junctions in sample A, B, C, with t_{MgO}=0.9, 1.2 e 2 nm, respectively. The box contains the 25/75 percentile of the values, the whiskers mark the maxima and minima. Right panel: TMR curve of a 2.5x120 μm^2 junction with t_{MgO}=2 nm and t_{fr}=1 nm, after a 330°C thermal annealing.

Fig. 4.10 (a) shows a statistical analysis of the TMR values and resistance per area product (RA) of the junctions in samples A, B and C with t_{fr} = 1.4 nm and different MgO thicknesses $t_{MgO\ A}$ = 0.9 nm, $t_{MgO\ B}$ = 1.2 nm and $t_{MgO\ C}$ = 2 nm respectively. Average TMR values of $86.6\% \pm 2.4\%$ and $70.8\% \pm 3.5\%$, and average RA values of $2.38\ \mathrm{M\Omega\mu m^2} \pm 19\%$ and $395\ \mathrm{k\Omega\mu m^2} \pm 7.8\%$ were measured for samples B and C, respectively, where the error is the standard deviation on the population. The low variability in the result both concerning RA values and TMR values, and the high yield (an average of 83% of working junctions in each sample) confirm the reproducibility of the sensor fabrication process and the high quality of the MgO barrier.

Sample A shows a higher variability both in the TMR ratio $(44\% \pm 16\%)$ and in the RA product, $(14.04\ \mathrm{k\Omega\mu m^2} \pm 29\%)$. This is due to the thinner MgO barrier, where the non-perfectly uniform barrier thickness and the presence of defects leads to a non-ideal tunneling behavior. As expected from the considerations in section 2.2, the sensor resistance is reduced decreasing the oxide thickness. RA product increases by a factor of 100 increasing the MgO barrier thickness from 0.9 nm to 2 nm. This change is quantitatively consistent with the values found in the literature,[115] revealing a good quality of the barrier and a good control over the MgO thickness.

For protecting the sensor surface and insulating the contacts from the solutions dispensed during the experiments, the active area of the sensor arrays is capped with a with a SiO_2 200 nm thick layer or with a SiO_2 50/Al_2O_3 60/SiO_2 180 trilayer grown by sputtering.

4.3.4 Noise measurements in MTJs

Noise measurements in magnetic tunnel junctions are crucial because they indicate the ultimate field resolution that can be achieved at any particular frequency.

Noise in MTJs is associated to various mechanism, in particular the main contributions are:[116–118]

- Shot noise at nonzero bias currents (P_{noise}/Hz= $2qi$), which is associated with the tunneling across the barrier and is caused by the quantization of charge carriers.
- Thermal or Johnson-Nyquist noise at zero bias currents (P_{noise}/Hz= $4K_bTR$), which corresponds to the random voltage caused by thermal fluctuations of the electric charge.
- 1/f noise (nonmagnetic 1/f noise and magnetic 1/f noise). The 1/f noise manifests itself as resistance fluctuations in the low frequency range, while the magnetic noise is produced by magnetization oscillations.

The noise measurements have been performed at the department of Electronics and Information of Politecnico di Milano by the research group led by Marco Sampietro, and by Chiara La Torre, in the framework of her master thesis.[119] The system used was a spectrum analyzer based on the cross-correlation technique between two different acquisition channels.[120]

First, the measurements were carried out without applying magnetic field, then a magnetic field generated by external permanent magnets was applied, in order to shift the operating point in the linear region of the transfer curve. This allowed the quantification of the magnetic contribution to the noise of the system and enabled a direct comparison with literature. From Fig. 4.9 it can be seen that, as an effect of the shifted loop of the sensing layer, at zero applied

field the magnetization is very close to saturation. As a result, in this configuration, the sensor is not heavily affected by magnetic noise. This situation, as explained in section 5.3, is comparable to the one adopted in our molecular recognition experiments.

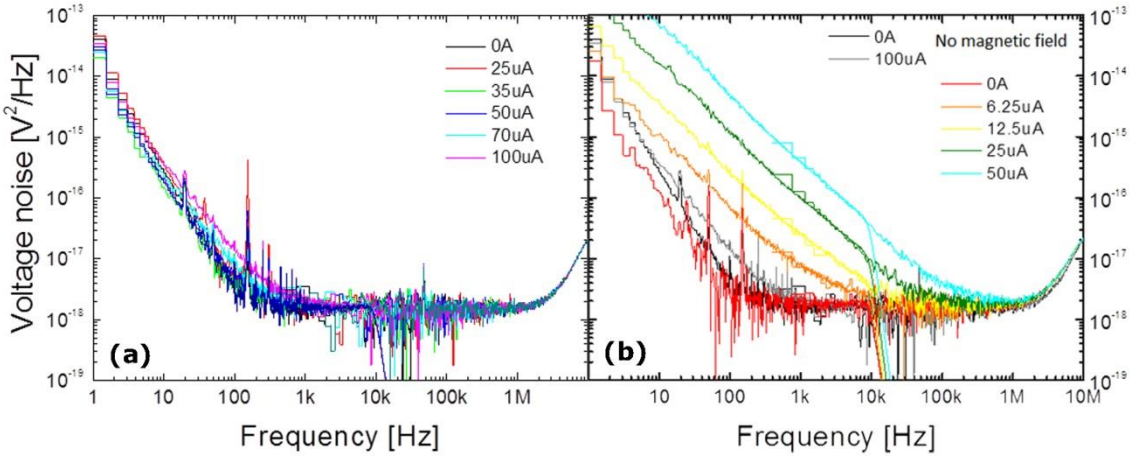

Fig. 4.11 Noise power density V^2/Hz varying the junction current: (a) without applying magnetic field and (b) applying magnetic field (linear region of the transfer curve). For a direct comparison the cases of 0 and 100 μA in absence of magnetic field have been shown (black and gray curves).

Fig. 4.11 (a) shows the noise spectra of sample A ($t_{MgO\ A}$ = 0.9 nm, R_{sens}~ 90 Ω) with no applied magnetic field. The current flowing through the sensor was varied from 0 to 100 μA. For each set of measurements it is possible to observe an instrumental noise at low frequencies, as can be noted observing the spectrum at zero current (in this condition the MTJ spectrum must be flat, thus any changes in the noise is due to the instrumentation) and at high frequencies, as can be noted observing the anomalous increase of the noise above 1MHz.

We observe a low thermal noise, around $5 \cdot 10^{-18}$ V^2/Hz, mainly due to the reduced resistance, and a corner frequency of the 1/*f* noise around 100 Hz. This is a good result considering that in biological experiments we apply an oscillatory junction current at the frequency *f* = 1.14 kHz (see section 4.4 and chapter 6), that is an order of magnitude higher than this corner frequency. Similar results in literature have been obtained by Freitas et al.[121] In Ref. [117] a higher 1/*f* contribution has been measured in a range of 100 and 1000 Hz for MgO based tunnel junctions with a comparable resistance, in the state of parallel magnetizations between free and pinned layer.

In Fig. 4.11 (b) noise spectra under an applied magnetic field are shown. In this case, the sensor is in the linear part of its characteristic. The effect of the magnetic field, as expected, is definitely clear in particular on the corner frequency of the the 1/*f* noise that has shifted towards higher frequencies, in agreement with other works.[117,121] According to Refs [122] and [118], the increase of noise is due to the fact that the external magnetic field has changed the magnetic configuration of the sensor, leading to a midway, unstable, condition between the

two saturations. It is worth to notice that the presence of the static magnetic field does not contribute to an increase of the noise background of the instrumentation, as checked by measurements on reference non-magnetic samples.

As it will be demonstrated in chapter 5, the optimal working point on the sensor characteristic during the biological experiments is close to the saturation, thus leading to negligible magnetic noise. In this configuration, our sensors display a "flat" frequency response and a low 1/*f* frequency corner noise (around 100 Hz).

4.4 Microfluidics and electronics

The microfluidic apparatus (Fig. 4.12 (a) and (b)) consists of a click-on cell comprising a Polycarbonate (PC) chip holder on top of which a microfluidic chamber is defined by a Polydimethylsiloxane (PDMS) gasket and a PC cover. The PC cover is equipped with holes for inserting the metal retractable tips for contacting the bottom and top electrodes of each sensor. The gasket, which defines the 12 mm^3 volume of the chamber on top of the sensor array, prevents the solution to come in contact with the tips and the pads. The syringe pump, used to inject the fluid at a controllable rate into the microfluidic cell, is a NE-1000 Multi-Phaser (New era pumps system, USA). The microfluidic cell is connected to the syringe pump by Tygon™ tubings and through adapters to the external syringes.

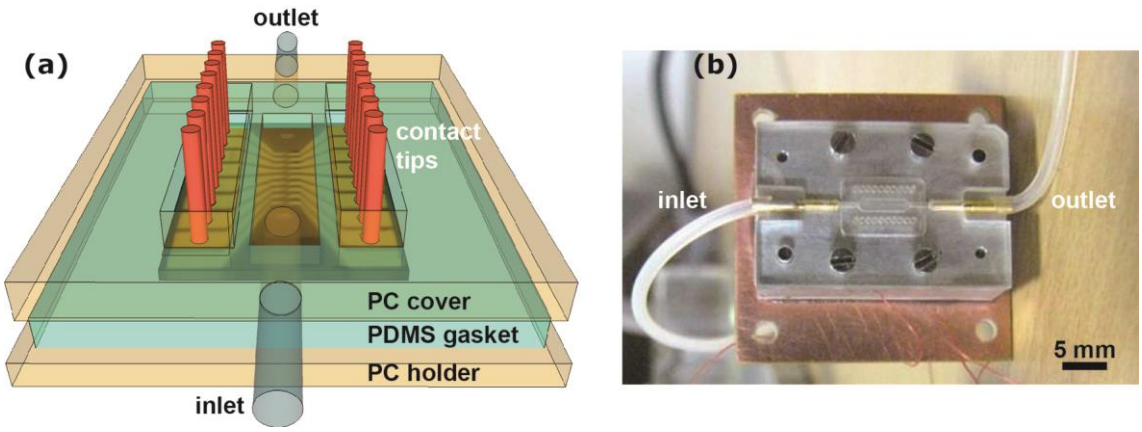

Fig. 4.12 (a) Sketch of the sensor array integrated in the microfluidic setup. 16 contact tips address independently the top and bottom electrodes of each sensor. From [P5]. (b) Picture of the microfluidic setup.

The signal acquisition is based on a double modulation technique, which involves a frequency modulation of both the junction voltage (frequency f_1) and the external magnetic field applied during the measurement (frequency f_2).[123] The sensor signal is demodulated by a lock-in amplifier which extracts the component at the sum frequency (f_1+f_2), which is related to the concentration of magnetic beads in proximity of the sensor area. As explained in chapter 5,

this allows an effective rejection of the $1/f$ noise and a significant improvement in the sensor sensitivity to the magnetic beads.

Fig. 4.13 (a) shows a sketch of the measurement setup. The microfluidic cell with the sample is located between the poles of a low-remanence electromagnet connected to a KEPCO bipolar generator controlled by a function generator (Tektronix AFG3022). This allows us to apply an external magnetic field $H_e(t) = H_{\mathrm{DC}} + H_{\mathrm{AC}}\cos(2\pi f_2 t)$, where H_{DC} is a biasing static field and H_{AC} is the amplitude of a sinusoidal magnetic field with frequency f_2.

As shown in Fig. 4.13 (b), the oscillatory junction voltage $V_{\mathrm{in}}(t) = V_s\cos(2\pi f_1 t)$, which is generated by the lock-in amplifier (a Zurich Instrument HF2LI), is applied to the sensors and the series of a fixed resistance $r = 1\ \mathrm{k\Omega}$. A multiplexing system is used to address the eight different sensors in such a way that, for stability purpose, the current permanently flows throughout all the junctions. External manual switches allow the selective exclusion of any sensor from the measurement. The readout from each sensor occurs sequentially with a switching rate controlled via software. The output voltage V_{out} is demodulated by the lock-in amplifier and acquired by the PC via a Labview software which also performs the output signal visualization and the data saving.

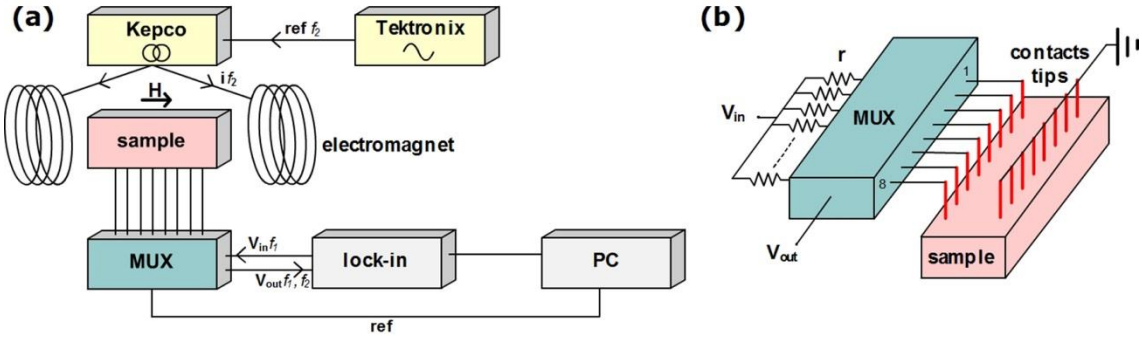

Fig. 4.13 (a) Circuit diagram of the instrumental apparatus used for the experiments of magnetic beads detection with a double modulation technique. (b) Sketch of the connections between the sample and the multiplexer. Each sensor has a r = 1kΩ resistance in series.

5. Conditions for efficient bead detection in magnetoresistive sensors

A commonly used figure of merit of magnetoresistive sensors employed to detect magnetic beads labeling biomolecules in lab-on-chip applications is the sensor sensitivity (S_0) to external magnetic fields in the linear region of the sensor. In this work we show that, in case of lock-in detection and bead excitation by a small AC magnetic field, S_0 is not the good figure of merit to optimize. Indeed, the highest sensitivity to the magnetic beads is achieved biasing the sensor in the region of its characteristic where the product between the DC bias field and the second derivative of the resistance with respect to the magnetic field is maximum. The validity of this criterion, derived from a phenomenological model of bead detection, is proved in case of magnetic tunneling junction sensors detecting magnetic beads with 250 nm diameter. This work paves the way to the development of a new generation of sensors properly designed to maximize the bead sensitivity.

5.1 Overview

Since the first pioneering work by the Naval Research Laboratory group in 1998,[124] magnetoresistive biosensors based on the detection of biological entities labeled with magnetic beads have emerged as a promising new platform technology for biosensing. As introduced in section 1.2.3, GMR, TMR and AMR-based sensors have been successfully applied to the detection of single magnetic particles[45,125,126,35] as well as to the focusing and detection of magnetic beads labeling target molecules in a biological sample.[37] In case of GMR devices, the detection of biomolecules with concentration down to the femtomolar[26] and zeptomolar[32] ranges has been achieved employing different techniques, without biochemical amplification.

The achievement of such extremely low limit of detection (LOD) essentially relies on three factors: (i) the optimization of the biochemistry connected to molecular recognition on the surface area, including the process of labeling with magnetic beads, (ii) the optimization of the sensor sensitivity to magnetic beads and (iii) the minimization of the sensor noise. In this section we will focus on the last two factors. In particular, we will provide a model for selecting the best operating conditions of magnetoresistive sensors for maximizing the sensitivity to magnetic beads in case of lock-in detection.

The sensor magnetic sensitivity is generally expressed as the maximum percentage variation of the sensor resistance (R) per unit change of the external field (H): $S_0 = \frac{1}{\mu_0 R}\frac{\mathrm{d}R}{\mathrm{d}H}$. Values of S_0 as high as 70%/mT have been reported[127] for TMR sensors used in biomolecular recognition applications, where the latter value represents the maximum of the derivative in the linear portion of the $R(H)$ characteristic. In practice, however, these sensors are not used in the linear regime, where S_0 is maximum, but with an external bias magnetic field shifting the operation point in the non-linear zone of the $R(H)$ curve, where S_0 is sizably smaller.[128,113] The reasons for such a counterintuitive choice have not been fully clarified in literature. The compensation of the stray fields coming from the free and pinned layers of the sensors, as well as the need for a DC field to magnetize the beads have been invoked to explain the need for this magnetic bias of the sensors[129] but a comprehensive and general explanation is still missing. In this work we present a theoretical model describing the operation of magnetoresistive sensors for the AC detection of magnetic beads, i.e. by exciting the beads with a small AC magnetic field and detecting the corresponding signal with a lock-in amplifier. As a general criterion for efficient bead detection we found that the sensors must be operated not in the linear regime, but properly biased, via an external DC magnetic field, at a point of their characteristic where the product between the DC bias field and the second derivative of the $R(H)$ curve is maximum. The validity of our approach is demonstrated using the MgO-based TMR sensor setup presented in section 4, whose sensitivity to magnetic bead sedimentation has been investigated as a function of the external DC bias field. This work sheds light on the choice of the best operating working point of magnetoresistive sensors for biochip applications, possibly paving the way to the development of new architectures for magnetoresistive sensors particularly suitable for efficient bead detection.

5.2 Experimental setup

Magnetic Tunneling Junctions (MTJ) stacks with the structure (thicknesses in nm) Si/SiO_2 1000 /Ta 5/Ru 18/Ta 3/$Ir_{22}Mn_{78}$ 20/$Co_{60}Fe_{40}$ 2/Ru 1.1/$Co_{40}Fe_{40}B_{20}$ 3/MgO 2/ $Co_{40}Fe_{40}B_{20}$ 1/Ru 5/Ta 5, were deposited by magnetron sputtering in the AJA system described in section 3.1. The optimized growth conditions used are listed in section 4.3.1.

After the deposition of the stack, arrays of 8 MTJ sensors (Fig. 5.1 A) were fabricated using optical lithography (section 4.3.2). The junction areas were defined by ion milling in the form of rectangles, 2.5×120 μm^2 wide, where the shorter side is parallel to the easy axis of the bottom layer of the junction, pinned by exchange bias, oriented along the y-axis in Fig. 5.1 B. After e-beam evaporation of Cr 7/Au 300 contacts, the samples were annealed in vacuum at 330° C at a pressure of 10^{-6} Torr for 1 hour in a magnetic field of 400 mT applied along the positive y-direction. Then, a 200 nm thick SiO_2 layer was deposited in RF mode from a SiO_2

target to electrically insulate the sensor stack and protect it against fluids dispensed on the chip via the microfluidic apparatus. The latter is described in detail in section 4.4. In Fig. 5.1 C, the sensor transfer curve $R(H)$ for a field applied in the y-direction is reported. The curve displays a tunneling magnetoresistance of 50% and a low-field sensitivity $S_0 = \frac{1}{\mu_0 R}\frac{\mathrm{d}R}{\mathrm{d}H} \sim 12 \frac{\%}{\mathrm{mT}}$ in the linear region. This sensitivity results from the combined effect of the shape anisotropy[112] and the superparamagnetic behavior of the top FeCoB layer,[127] leading to an easy axis of the top free layer perpendicularly aligned to that of the reference layer and to negligible hysteresis (for details, see section 4.2). The shift of the characteristic towards negative fields can instead be attributed to Néel or dipolar coupling between the top and bottom layers of the tunneling junction.

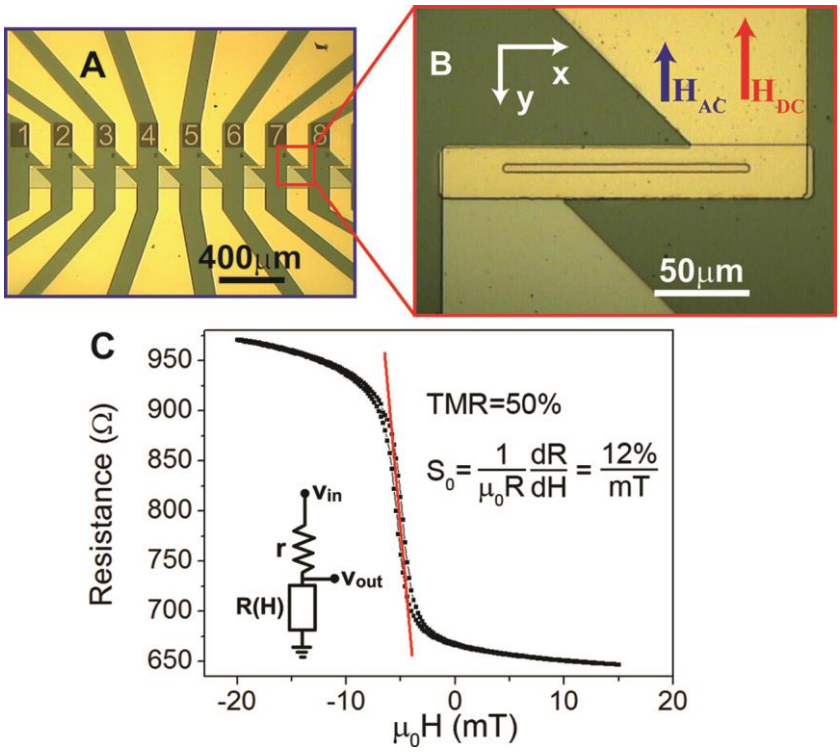

Fig. 5.1 (A) Optical image of the layout of the chip with 8 MTJs sensors. (B) Zoom on a single sensor showing the geometry of the applied magnetic fields. (C) Sensor resistance $R(H)$ measured applying a 10 mV voltage across the junction. In the inset, the sketch of the circuit used for AC detection is shown. From [P3].

The scheme of the circuit used for detection the AC signal in response to the applied AC magnetic field is reported for a single sensor in the inset of Fig. 5.1 C.

In order to improve the sensor sensitivity and minimize the $1/f$ noise,[123] the voltage applied to the series of a fixed resistance (r = 1 kΩ) and of the sensor resistance $R(H)$ is modulated at a frequency f_1 = 51 kHz ($V_{\mathrm{in}}(t) = V_s \cos(2\pi f_1 t)$, V_s = 250 mV), while an external magnetic field H_e is applied parallel to the sensing axis, which corresponds to the y-direction in Fig. 5.1 B. H_e is the sum of two contributions: a bias field H_{DC} and a small oscillating field

$H(t) = H_{DC} + H_{AC}\cos(2\pi f_2 t)$ used for exciting the beads, where h = 0.5 mT and f_2 = 39 Hz. Thanks to this double modulation, the response to H_{AC}, eventually depending on the concentration of beads above the sensor, appears in the output voltage (V_{out}) as a component at the frequency ($f_1 \pm f_2$), which can be easily extracted via a lock-in amplifier. The amplitude of the small oscillating field h = 0.5 mT has been chosen as the best compromise between two needs: (i) maximizing the excitation field of the beads and (ii) keeping its amplitude as small as possible in order to fully exploit the local non-linearity of the $R(H)$ sensor characteristic.

5.3 Detection of the sedimentation of magnetic beads

To investigate the sensitivity to the bead concentration in various operating conditions we monitored the output voltage during bead sedimentation. Upon injecting in the cell, at a rate of 150 µl/min, an aqueous suspension with fixed concentration (~ 4.9 x 10^{10} beads/ml) of Micromod nanomag® -D streptavidin nanoparticles with 250 nm diameter, we stopped the syringe pump and waited for 15 minutes, allowing for a full sedimentation of the beads. Then the bead suspension was washed output with de-ionized (DI) water at a rate of 450 µl/min, till the signal recovered the initial baseline.

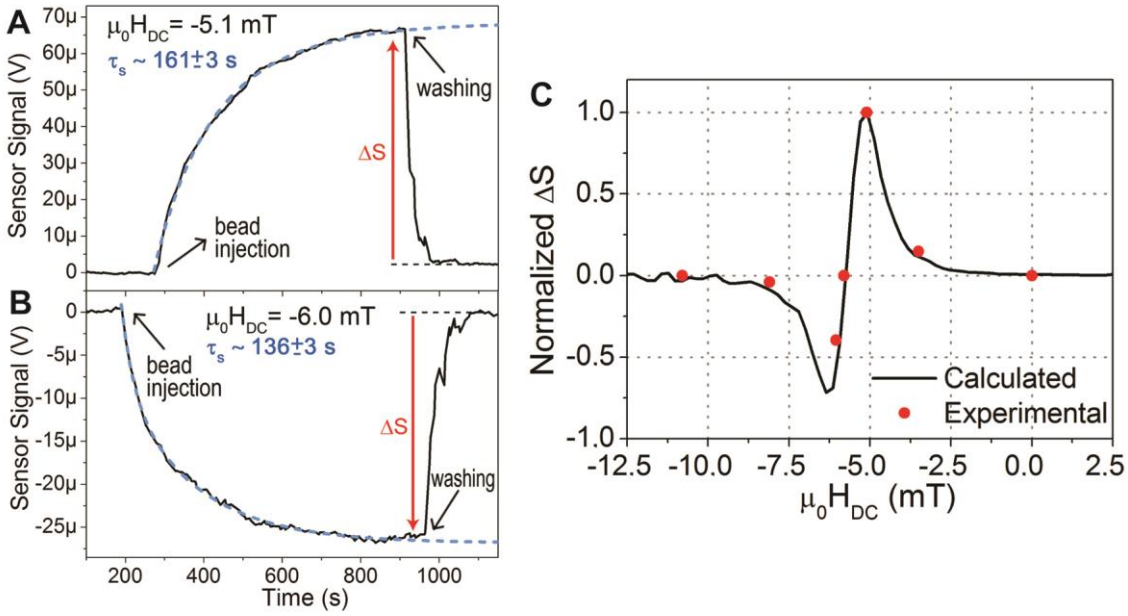

Fig. 5.2 (A,B) Bead sedimentation for different bias magnetic field H_{DC}; the blue dashed line is an exponential fit of the signal from which the sedimentation time constant τ_s is extracted. (C) ΔS signal normalized to its highest value (red dots) as a function of the applied magnetic field H_{DC}; the black line is a fit performed accordingly to Eq. (5.5). From [P3].

The signal acquired during sedimentation and subsequent washing is shown in Fig. 5.2 A and 2B for two different values of the bias field, namely -5.1 mT and -6.0 mT. Interestingly enough, the signal variation ΔS upon bead sedimentation changes sign for such a relatively small

variation of the bias fields. In Fig. 5.2 C we plotted with red dots the ΔS values measured for different DC bias, normalized to the maximum value obtained in these experiments (see Table 5.1). Apart from the null signal at high positive and negative fields, where the sensing layer is in saturation, the oscillating behavior of the sensitivity to beads seen in Fig. 5.2 C is particularly critical for the device operation. In fact, even a minor shift of the bias field from -5.0 mT, corresponding to the maximum bead sensitivity, to -5.8 mT, determines the complete suppression of the sensitivity to magnetic beads. Noteworthy, -5.8 mT corresponds to the point of the sensor characteristic where the sensor sensitivity to external magnetic fields (S_0) is maximum, pointing out that S_0 is definitely not a good figure of merit in case of magnetoresistive sensors employed for bead detection purposes.

Table 5.1 α_{DC} parameter, sedimentation signal (ΔS), baseline noise (N), signal to noise ratio ($|\Delta S|/N$) and sedimentation time constant (τ_s) as a function of the applied magnetic field H_{DC}. From [P3].

$\mu_0 H_{DC}$	α_{DC}	ΔS	N (μV)	$\lvert\Delta S\rvert/N$	τ_s
0	-	0	-	-	-
-3.0	$-1.45\cdot10^{-2}$	10	$-4.59\cdot10^{-2}$	218	224±1
-5.1	$-5.9\cdot10^{-3}$	66	$-2.04\cdot10^{-1}$	323	161±3
-5.8	-	0	$-1.58\cdot10^{-1}$	-	-
-6.0	$-4.85\cdot10^{-3}$	-25	$-1.60\cdot10^{-1}$	156	136±3
-8.1	$-1.12\cdot10^{-2}$	-2.7	$-3.99\cdot10^{-2}$	68	22±1
-10	-	0	-	-	-

The characteristic sedimentation time τ_s, the bead signal ΔS, the root mean square noise of our base-line signal N and the signal to noise ratio $|\Delta S|/N$ for each DC bias field tested in our experiment are reported in Table 5.1. As expected, the sedimentation time monotonically decreases when increasing the field H_{DC} due to the enhanced magnetic moment on the beads, at variance with the sensor sensitivity to beads which presents an oscillating behavior, thus indicating that spurious effects coming from the different focusing of beads on top of the sensor due to the stray field play a minor role. The estimated values of the coefficient α_{DC} (see Appendix A and the next paragraph for details), describing the overall capability of the beads to produce a change of the magnetic field on the sensing layer upon complete sedimentation, show indeed minor modifications as a function of the bias field. Noteworthy, α_{DC} is minimum where we found the maximum sensitivity to beads, clearly ruling out the possibility that the best operating condition corresponds to the optimum focusing of the beads during sedimentation. The stray field of the top CoFeB free layer can indeed have some impact on the determination of the best operating conditions. A more detailed analysis reported in Appendix A shows that the main effect could be only a minor shift of the position of the maxima in the curve of Fig. 5.2 C by less than 1 mT.

Let us finally discuss the influence of the bias on the signal to noise ratio, which is the ultimate figure of merit to be optimized. From Table 5.1 it is evident that the highest level of noise *N*, defined here as the standard deviation of the signal baseline before sedimentation, is found in the linear region of the sensor, while it decreases approaching the magnetic saturation of the free electrode, where magnetic fluctuations are suppressed. This implies that the signal to noise ratio, defined as the ratio $|\Delta S|/N$, has even more pronounced maxima in correspondence to the maxima of ΔS than ΔS itself.

5.4 Model of the sensor sensitivity to magnetic beads

In order to shed light on the physical mechanisms giving rise to such a dependence of the sensitivity and find out a general criterion for correctly choosing the bias field, we developed a phenomenological model of bead detection. For small *h* values, as compared with the width of the linear regime of the *R*(*H*) characteristic, the AC magnetic field used for exciting the beads can be considered as a perturbation superposed to the DC bias field so that, without beads above the sensor, we can write:

$$R(H_{\mathrm{DC}}+H_{\mathrm{AC}}) \approx R(H_{\mathrm{DC}}) + \left.\frac{\mathrm{d}R}{\mathrm{d}H}\right|_{H_{\mathrm{DC}}} \cdot h\cos(2\pi f_2 t) \tag{5.1}$$

The average DC and AC stray fields produced by the beads on the sensor free layer are instead $H_{b\mathrm{DC}} = \alpha_{\mathrm{DC}} H_{\mathrm{DC}}$ and $H_{b\mathrm{AC}} = \alpha_{\mathrm{AC}} H_{\mathrm{AC}}$ (see Appendix A for the discussion about the impact of demagnetizing fields coming from the sensor ferromagnetic layers and about the magnetic interaction between the two layers via Néel coupling). Here, the linear bead response is described by the coefficient $\alpha = \beta\chi V_b n$, where χ is the magnetic susceptibility of the beads (AC or DC), V_b their volume, *n* the number of beads per unit volume and β is a geometrical factor which depends on the beads size and distribution over the sensor area.[130,131] The stray field generated by magnetic beads then adds up to the external fields leading to:

$$R(H_{\mathrm{DC}}+H_{\mathrm{AC}}) \approx R\big(H_{\mathrm{DC}}\cdot(1+\alpha_{\mathrm{DC}})\big) + \left.\frac{\mathrm{d}R}{\mathrm{d}H}\right|_{H_{DC}(1+\alpha_{\mathrm{DC}})} \cdot h\cdot(1+\alpha_{\mathrm{AC}})\cdot\cos(2\pi f_2 t) \tag{5.2}$$

The sensor output voltage can then be written as:

$$V_{\mathrm{out}} = V_s\left\{\frac{R\big(H_{\mathrm{DC}}(1+\alpha_{\mathrm{DC}})\big)}{r+R\big(H_{\mathrm{DC}}(1+\alpha_{\mathrm{DC}})\big)}\cos(2\pi f_1 t) + \frac{1}{2}\frac{\mathrm{d}R}{\mathrm{d}H}h\cdot(1+\alpha_{\mathrm{AC}})\cdot\right. \tag{5.3}$$

$$\left.\cdot\frac{r}{\big[r+R\big(H_{\mathrm{DC}}(1+\alpha_{\mathrm{DC}})\big)\big]^2}[\cos(2\pi(f_1-f_2)t)+\cos(2\pi(f_1+f_2)t)]\right\}$$

The normalized signal S_v, demodulated by the lock-in at a frequency (f_1+f_2) results:

$$S_v = \frac{V_{\text{out}}}{V_s} = \left(\frac{1}{2} \frac{\mathrm{d}R}{\mathrm{d}H}\Big|_{H_{\text{DC}}(1+\alpha_{\text{DC}})} \cdot h \cdot (1 + \alpha_{\text{AC}}) \cdot \frac{r}{\left[r + R\big(H_{\text{DC}}(1 + \alpha_{\text{DC}})\big) \right]^2} \right) \tag{5.4}$$

Finally, the net signal ΔS (see Fig. 5.2 A and B) due to the sedimentation of the beads on the sensor surface can be calculated within the approximation $|\alpha_{\text{DC}}| \ll 1$ (See Appendix A for details), leading to:

$$\Delta S = S_v|_{\text{beads}} - S_v|_{\text{plain}} = \frac{1}{2} \frac{r}{[r + R(H_{\text{DC}})]^2} h \alpha_{\text{AC}} \left(\frac{\mathrm{d}R}{\mathrm{d}H}\Big|_{H_{\text{DC}}} + \frac{\mathrm{d}^2R}{\mathrm{d}H^2}\Big|_{H_{\text{DC}}} H_{\text{DC}} \right) \tag{5.5}$$

According to this expression, ΔS is not simply proportional to α_{AC}, but also to the sum of $\frac{\mathrm{d}R}{\mathrm{d}H}\Big|_{H_{\text{DC}}}$ and $\frac{\mathrm{d}^2R}{\mathrm{d}H^2}\Big|_{H_{\text{DC}}} \cdot H_{\text{DC}}$. The presence of the latter term explains why for the same bead concentration and distribution above the sensor resulting upon complete sedimentation (i.e. for similar values of the parameter α_{AC}) we can find different values of ΔS and even an inversion of its sign for different bias fields H_{DC}, as previously discussed. This is because the second derivative in the last term of Eq. (5.5) changes sign when sweeping the bias field. It is largely negative for -6.0 mT and becomes positive for -5.1 mT, while for a critical intermediate field a perfect compensation of the two terms containing the first and second derivative in the bracket takes place, eventually leading to $\Delta S = 0$. The soundness and reliability of our interpretation is confirmed by the nice fit (black continuous line in Fig. 5.2 C) of the experimental values for the normalized bead signal ΔS reported in Fig. 5.2 C, that we obtained using Eq. (5.5) with $\alpha_{\text{AC}} = -3.73 \cdot 10^{-3}$. Furthermore, the fitting procedure gives rise to a negative value of α and β, consistent with the simulations reported in Fig. 5.3.

Note also that the first term in the brackets of Eq. (5.5), which coincides with the first derivative, is typically smaller than the last term, containing the second derivative (see Appendix A). As a result, the entity of the first derivative essentially determines the critical bias field leading to zero sensitivity. To summarize, from our analysis it turns out that the maximum variation of the sensor signal due to the beads (ΔS) can be achieved not in the linear region of the sensor characteristics, but at some bias H_{DC} where the second derivative, multiplied by the bias field itself, is maximum. The above criterion for the choice of the best DC bias can be easily understood with reference to the mechanism used for AC detection. As pointed out in Eq. (5.4), the sensor output upon the lock-in demodulation is proportional to the first derivative of the sensor characteristic. Therefore, we can expect an increase of ΔS in a working point where the AC stray field from the beads can produce a significant change in the first derivative, i.e. where the second derivative is large. This is exactly the meaning of the second term in the brackets of Eq. (5.5), where the presence of the factor H_{DC} essentially indicates

that a static field is required in order to magnetize the beads whose corresponding DC stray field can then shift the working point of the sensor. Note that this is different from the case of DC detection of beads already discussed by Wang et al., in Ref [128]. As a matter of fact, in the latter paper, the authors show an oscillating behavior of the bead sensitivity vs. DC bias field very similar to the one shown in Fig. 5.2 C. In case of perfectly symmetric sensor characteristic, without shift due to magnetic coupling between layers, they correctly explain the maxima for non-zero bias as the result of the compromise between the sensor sensitivity and the need for non-zero bias field in order to get the beads magnetized. However, the case of AC detection is quite different, because a non-null bead signal can be achieved also without DC net bias field, as there is in any case an oscillating AC field exciting the beads and then producing a signal detectable by the lock-in. Indeed, Eq. (5.5) points out that in case $H_{\mathrm{DC}} = 0$ a net bead signal is still present. Our model clarifies that, in the AC detection mode, an external DC bias is needed not simply to magnetize the beads, but essentially in order to drive the sensor in a highly non-linear region of its characteristic where the sensitivity to the beads is maximum.

5.5 Calculation of the magnetic field generated by one bead on the sensor

Following previous works,[130,131] we calculated the average magnetic field on the sensor area from a single bead in suspension above the sensor, magnetized by the field in the *y*-direction as a function of the position of the bead itself (see Fig. 5.3). For a monolayer of beads, located 800 nm above the sensor (this is the overall thickness of the capping and contact layers of our devices), we can estimate the sign of β, and hence of α, by integrating the contributions arising from the single beads. In Fig. 5.3 A, the average $H_{b\mathrm{DC}}$ generated by a bead on the sensor is plotted as a function of the bead position along the *y*-axis, keeping the bead position along the *x*-axis fixed in the center of the sensor. The values are normalized to the modulus of the maximum average field H_{MAX}. The average field is negative when the bead is above the sensor area and positive when it is outside the sensor area. For a homogeneous bead distribution, the positive and negative contributions cancel each other, implying that in this case a monolayer of beads would not give a detectable sensor response. As shown in the optical image of Fig. 5.3 B, however, after sedimentation, beads are mainly concentrated above the sensor area due to the focusing action of the sensor stray field. In fact, the sensor area in Fig. 5.3 B is brown due to the bead accumulation, at variance with the case of absence of beads reported in Fig. 5.1 B, where the sensor and the surrounding area are the same color, i.e. pale brown. As a consequence, the overall sign of $H_{b\mathrm{DC}}$, and hence of α, is negative, in agreement with the values of alpha used in the fit.

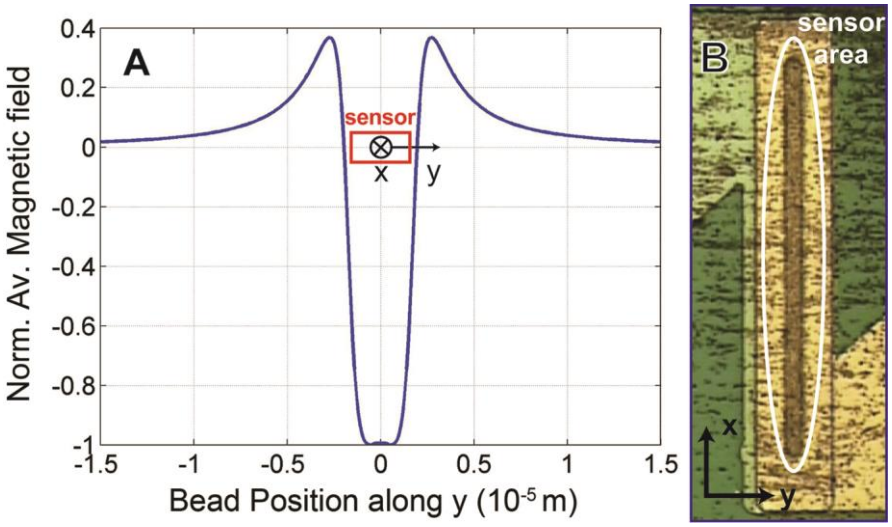

Fig. 5.3 (A) Average magnetic field H_{DC} produced by a single bead on the sensor as a function of the bead position along the y-direction with respect to the sensor. (B) Optical image of the sensor area after sedimentation: the bead distribution is concentrated upon the sensor area due to focusing action of the sensor stray field. From [P3].

5.6 Conclusions and perspectives

In conclusion, we have shown that the optimum working point for operating a magnetoresistive sensor in order to maximize its sensitivity to the beads does not correspond to the linear part of the *R(H)* characteristic where the sensitivity to the external field is maximum. The highest sensitivity to beads is instead achieved in the non-linear region, for a specific bias field H_{DC} which allows to maximize the product $\frac{d^2R}{dH^2}\Big|_{H_{DC}} \cdot H_{DC}$. This, in turn, reflects in the optimization of the sensitivity of the bioassays based on spintronic biosensors, as it will be shown in section 6 in case of DNA-DNA recognition experiments performed with our MTJ sensors. This work establishes a criterion for choosing the best operating conditions of magnetoresistive sensors for magnetic bead detection and could pave the way to the development of a new generation of sensors properly designed to maximize the bead sensitivity and minimize the limit of detection of related bioassays.

6. Photolithographic biopatterning of MTJ-based biosensors for molecular recognition

In this work we present a new, straightforward procedure to create patterns of bio-reactive polymer regions on the sensor's surface using optical lithography and a lift-off procedure. The effectiveness of the procedure in providing high specificity and improved sensor performance is demonstrated by calculations and experiments. The technique is employed for selectively functionalizing arrays of MTJ-based magnetoresistive sensors, which are then integrated in a microfluidic platform. On-chip biomolecular recognition assays demonstrate an enhanced sensitivity with respect to non-patterned sensors. More widely, our patterning method answers to the need for straightforward and high throughput techniques for creating micron-sized patterns of biological probes on the surface of biosensors and biochips.

This work was carried out in collaboration with the “Istituto di Chimica e riconoscimento molecolare” (ICRM-CNR) in Milan.

6.1 Overview

As we discussed in chapter 5, for achieving an extremely low limit of detection (LOD) in magnetoresistive biosensors, the maximization of the sensor sensitivity to the magnetic markers is crucial and not always straightforward. In chapter 5, we provided a model for maximizing such sensitivity by selecting the optimal operating point on the sensor characteristic. In this work, we addressed this problem focusing on the control of the position and size of the biologically active area (i.e. the region where the biological probes are immobilized) with respect to the sensor. As pointed out in section 5.5, the average magnetic field generated by the beads over the sensor area strongly depends on their position, changing even its sign if generated by a particle inside or outside the sensor.[131] This raises issues in quantifying the immobilized beads upon biomolecular recognition, and thus in determining a straightforward relationship between the sensor signal and the analyte concentration. For this reasons, controlling the beads distribution over the sensor, via selective patterning of probes, is critical for achieving a high and linear sensitivity to beads, which in turns ensures a low LOD.

Over the last decade, several methods for patterning biomolecules in micrometer size structures have been developed, such as micro contact printing,[132] capillary force lithography,[133] dip pen nanolithography[134] and nano-spotting.[135] A popular method for defining bio-active regions on magnetoresistive sensors is based on the selectiveness of thiol chemistry.[26] A gold layer is microfabricated and properly aligned over the sensor surface, and then selective gold functionalization is achieved thanks to spontaneous assembly of chemically reactive alkene thiols only on gold, thus leading to the formation of so called self-assembled monolayers (SAM).[136–138] However, the formation of a well-assembled monolayer is not always straightforward, as it strongly depends on the purity of the alkanethiol being used. The presence of even low levels of contaminants can result in a disordered, non-ideal monolayer.[139] Furthermore, the additional step consisting in the microfabrication of a gold overlayer can be critical in terms of cost and compatibility with the sensor layout. In the great majority of cases, the gold layer constitutes an additional layer above the insulating protecting layer which ensures biocompatibility and protects the sensor from the wet biological environment. This contributes to move the beads away from the active sensing layer, thus reducing the overall sensitivity. Alternative strategies, not requiring the physical deposition and patterning of gold, consist in the use of photo-activated esters derived from N-hydroxysuccinimide (NHS).[140] Patterning of aminohexyl modified DNA oligonucleotides is achieved through the selective photochemical reaction of a hydrogen-terminated silicon surface with alkenes functionalized with N-hydroxysuccinimide ester groups.[141] However, this technique is suitable only to silicon surfaces and the absence of a physical mask increases the risk of non-specific binding outside the patterned area.

An alternative, attractive solution is presented in this work. It consists in the direct photolithographic patterning of a coating layer suitable for probe immobilization. On one side, optical lithography is a widely accessible process available in all microfabrication facilities, providing sub-micron resolution and easy scale up to mass production. On the other hand, the use of functional polymeric coatings allows to achieve a high flexibility in the functionalization associated to the low cost of production inherent to wet processes. The effectiveness of the proposed bio-patterning technique is demonstrated in DNA recognition experiments run in the microfluidic system described in section 4.4.

6.2 Magnetic biosensing setup

The magnetic biosensing setup in this work is the same employed in chapter 5, and described in detail in chapter 4. The layout of the sensor array and the sensor characteristic are the same as in Fig. 5.1. Differently from chapter 5, we employed a SiO_2 50/Al_2O_3 80/SiO_2 200 multilayer as capping, in order to protect the sensor surface against the prolonged exposure to harsh

conditions during the patterning, hybridization and magnetic measurements. The size of the rectangular junction areas, measured after the lithographic process, is 3x120 μm^2.

6.3 Biopatterning, DNA probe immobilization and hybridization

In the method presented in this work, the photoresist pattern acts as a mask for a peculiar self-adsorbent bio-reactive polymer which binds only to the areas of the chip surface not covered by the photoresist upon development in the organic solvent. In this way, the subsequent DNA probe immobilization by spotting is effective only in the area coated by the polymer. The critical point of this approach is the need for organic solvents during the lithographic process, which can denature probes immobilized on the polymeric coating. In case of DNA probes, however, their high stability even in organic solvents allows to easily overcome this issue. Being the polymer stable in acetone, its bio-conjugation properties are not altered by the photoresist lift-off process which removes the photoresist while not affecting the DNA probe functionality for subsequent molecular recognition. In case labile probes are used, the spotting process can be performed after the lift-off procedure, so that any harsh chemical treatment on the probes is avoided. In principle this allows to extend this method to any kind of probe molecules. The main advantages of this approach are its simplicity, because it only requires a lift-off process, and its versatility, since the copoly binds not only to SiO_2 but also to other substrates such as titanium dioxide, silicon nitride and gold.

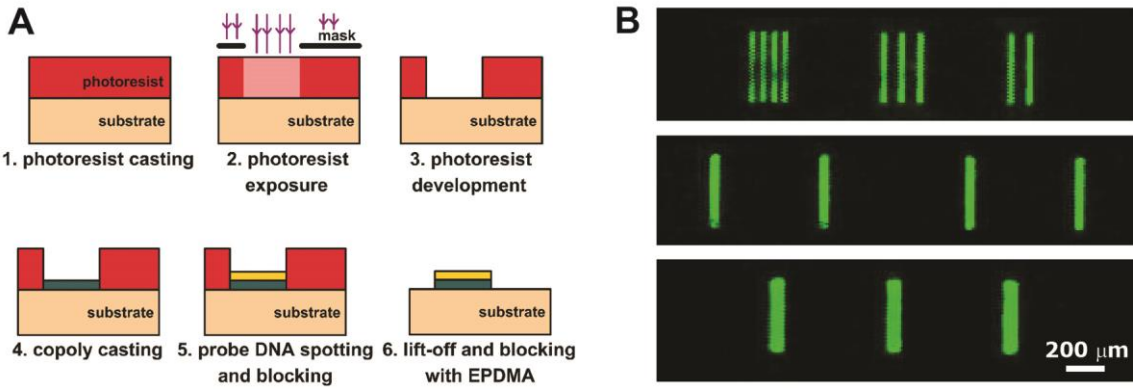

Fig. 6.1 (A) Sketch of the optolithographic process for the selective biofunctionalization. (B) Biopatterned rectangles with different sizes and spacing. 1 μM Cy3-fluorescent DNA target concentration was used. Adapted from [P5].

In Fig. 6.1 A the selective biofunctionalization process is sketched. After photoresist spinning (AZ 5214E) and soft bake, 6 x 120 μm^2 rectangles centered over the sensor areas were opened employing standard optical lithography (steps 1-3). The chips were then coated with a

functional copolymer (step 4) made of dimethylacrylamide (DMA), N-acryloyloxysuccinimide (NAS) and 3-(trimethoxysilyl) propyl methacrylate (MAPS), copoly(DMA-MAPS-NAS). This copolymer, introduced initially to immobilize oligonucleotides on the surface of microarray slides, suits the present application as (i) it forms a selective coating on the SiO_2 substrate by simple adsorption from an aqueous solution, not being affected by the photoresists proximity, (ii) it perfectly withstands lift-off in acetone. The copolymer synthesis procedure, first introduced by Pirri et al.,[142] was recently revised by Sola et al.[143] The coating provides active ester moieties suitable for immobilization of amino modified oligonucleotides and, at the same time, prevents non-specific adsorption of biological fluids components.

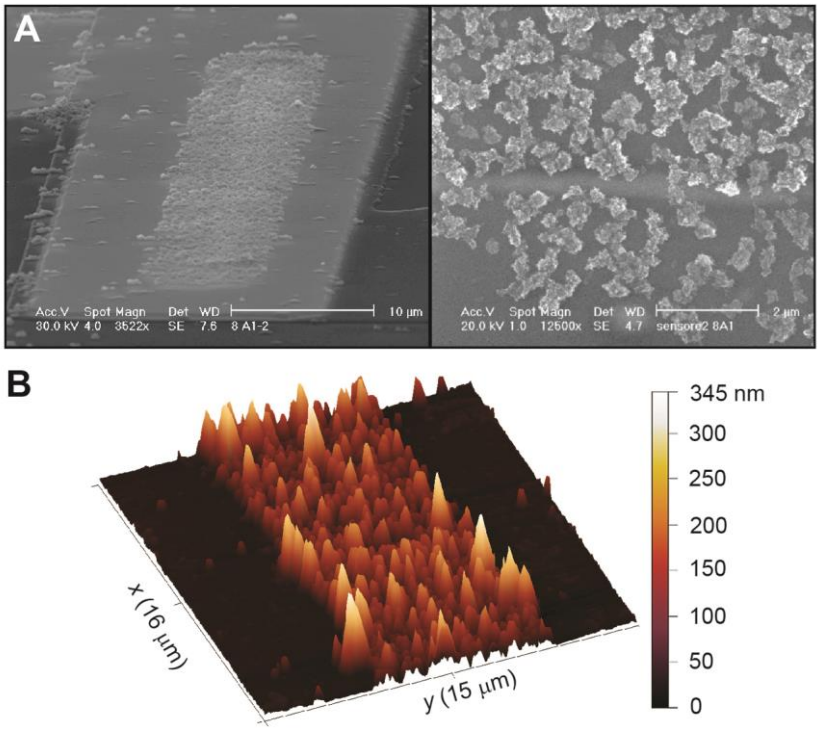

Fig. 6.2 (A) SEM images of the sensor after the biomolecular recognition. In this case a 1 µM DNA target concentration was used. The selectively functionalized area is covered by the nanoparticles immobilized on the surface through the streptavidin-biotin interaction. (B) AFM image of the sensor after biomolecular recognition the peaks from 100 nm to about 200 nm correspond to the nanoparticles that are fragmented after drying the chip. Adapted from [P5].

The chip was immersed for 30 minutes in a 1% w/v solution of copoly(DMA-MAPS-NAS) in an aqueous solution of ammonium sulfate at 20% saturation then rinsed with water and dried under vacuum at 80°C. The sensor area was then entirely spotted (step 5) with a 23- mer synthetic oligonucleotide with the following sequence: 5'-GCCCACCTATAAGGTAAAAGTGA-3', modified at the 5' end with C_6 amino linker, giving rise to about 10^{12} binding sites per cm^2 on the chip surface.[142] Six drops of the oligonucleotide were spotted at the center of the sensor area, immediately after the copolymer casting. Then the photoresist stripping was performed. The oligonucleotide was dissolved in 150 mM sodium phosphate buffer pH 8.5 at different

final concentrations (ranging from 1 μM to 1 pM) and spotted using a non-contact microarray spotter SCENION sci-FLEXARRAYER S5 assembled with a 80 μm nozzle. Spot volume of each drop, temperature and humidity were 400 pL, 22°C and 50% respectively. After overnight incubation in the humid chamber, allowing the oligonucleotide binding, the photoresist was stripped in acetone (step 6). Finally, the surface was blocked with a solution of bovine serum albumin (1% w/v) in phosphate saline buffer (PBS) for 1 hour. This treatment prevents unspecific binding of biomolecules outside the patterned area during the subsequent DNA hybridization phase.

The sensors were then incubated with a complementary oligonucleotide target of sequence 5'-TCACTTTTACCTTATAGGTGGGC-3', labeled with biotin at the 5' end. The sensor surface was fully covered for 2 hours with a 1 μM solution of the oligonucleotide target dissolved in the hybridization buffer (2X saline-sodium citrate –SSC-, 0.1% w/v sodium dodecylsulphate -SDS- and 0.2 mg/ml of BSA). Finally, the chip was washed for 5 minutes with the washing solution (2X SSC, 0.1% w/v SDS), rinsed in 0.2X and 0.1X SSC buffer and dried under a nitrogen stream. Reference sensors were spotted with an oligonucleotide having the same sequence of the target (5'-TCACTTTTACCTTATAGGTGGGC-3') but modified at the 5'end with a C_6 amino linker.

Fig. 6.1 B shows rectangular shapes on a Si/SiO_2 substrate, biopatterned following the same procedure employed for the sensors. After the blocking step, in this case the sample was incubated with complementary target DNA labeled with a Cy3 dye, which allows the visualization of the patterns through fluorescence.

6.4 Magnetic labeling and biosensing

Micromod® Nanomag®-D, 250nm diameter streptavidin coated magnetic beads (75–80% (w/w) magnetite in a matrix of dextran (40 kD)) were dispersed in phosphate buffer (PB)-Tween solution (~10^8 particles/μl) and injected into the microfluidic cell at a flow rate of 50 μl/min. After filling the cell, the pump was switched off and a 15 minutes waiting time allowed particle sedimentation and selective immobilization over the sensor surface where the target molecules expose biotin. Finally, the sensor was washed several times with PB/Tween20 to remove unspecific, weakly bound magnetic nanoparticles. For the biotin-streptavidin binding and washing, phosphate buffer (PB) 0.1 M pH 7.4 with 0.02% of Tween20® was used.

During all these operations the magnetoresistive response of the sensor was recorded. As it depends on the magnetic stray field from the beads, this allows to monitor the concentration of beads during the detection experiment and correlate it to the concentration of the target analyte.

The magnetoresistive signal was acquired employing the double modulation technique presented in section 4.4 in order to improve the sensor sensitivity and minimize the 1/*f* noise. The current through the sensors was modulated at a frequency f_1 = 1.101 kHz by applying an AC voltage to the series of a load resistance (2 kΩ in this case) and of the sensor connected to ground. The voltage drop across the sensor, proportional to the sensor resistance, was sent to the lock-in. An external magnetic field H_{ext} was applied parallel to the sensing axis, which corresponds to the *y*-direction in Fig. 5.1 B. H_{ext} was the sum of two contributions: a DC field to bias the sensor in the optimal point of its characteristic, and a small oscillating field at f_2=39 Hz to excite the magnetic beads. The sensor signal, related to the concentration of beads above the sensor, appears in the output voltage as a component at the frequency ($f_1 \pm f_2$), which can be easily extracted via a lock-in amplifier.

The multiplexer was used to sequentially address the eight different sensors while current was permanently flowing through all the junctions, in order to ensure a good thermal stabilization.

6.5 Calculation of the optimal biopatterning area

In order to assess the importance of the beads distribution on the sensor signal and identify the optimal area of the sensing surface, we simulated the magnetic field produced by beads at different positions over the sensor, refining the calculation presented in section 5.5 for considering the actual experimental sensor geometry. We calculated the average magnetic field generated in correspondence of the sensor free layer by a single magnetic bead (MNP) magnetized along the *y*-direction, in suspension at a distance *z* above the sensor surface. In Fig. 6.3 A, the average magnetic field, normalized to the magnitude of the maximum average field H_{max}, is plotted as a function of the MNP position with respect to the center of the sensor. It is worth noting that the average field has the same sign as the external magnetizing field when the MNP is outside the sensor area and opposite sign when the MNP is above the sensor area. Considering a homogeneous distribution of beads (e.g. an infinite monolayer of MNP) at the same height *z* above the sensor, the positive and negative contributions perfectly compensate each other, thus giving rise to a not detectable signal. However, in our case, the bead distribution is not planar, because outside the sensor area (3 μm wide) an additional SiO_2 layer (100 nm thick) is used to separate the electrical contacts from the sensor plane. This causes the beads immobilized over the sensor area to be closer to the sensor free layer and generate a higher signal than those outside, placed 100 nm above. In the simulations this is taken into account considering two different *z*-distances for beads outside (z_o = 700 nm) and upon the sensor area (z_u = 600 nm).

It is worth noting that, whereas the signal arising from the MNP above the sensor area is almost independent on the position, the contribution of MNPs outside the sensor area

strongly depends on the MNP location, thus hindering a straightforward quantitative analysis. This calculation makes clear the importance of a micrometric precision on the spatial control over the beads distribution both for maximizing the magnetic signal and for enabling accurate quantitative data analysis. For details on the calculation, see Appendix B.

Fig. 6.3 B shows the enhancement in the average magnetic field on the sensor due to the patterning (H_{bpat}/H_b), as a function of the width of the functionalization area. In particular, H_{bpat} is the average magnetic field generated on the sensor by a distribution of magnetic beads which is centered with respect to the sensor area, is infinite in the *x*-direction and has a limited width y_a along the *y*-direction. H_b is the average magnetic field generated on the sensor by an infinite distribution of beads (i.e. y_a approaches infinite). In our case, the maximum increase in the magnetic field (H_{bpat}/H_b ~ 5.2) is given by the width y_{amax} ~ 3.7. Increasing y_a, we start to pick up the opposite contribution arising from the beads outside the sensor area, until eventually we reach $H_{bpat}/H_b = 1$, when y_a approaches infinite.

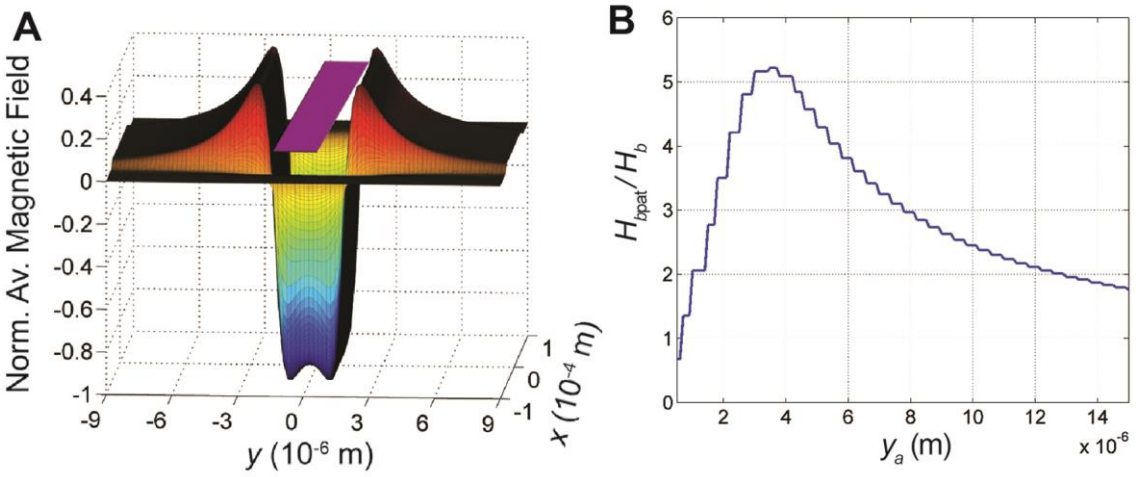

Fig. 6.3 (A) Average magnetic field H_{DC} produced by a single bead on the sensor as a function of the bead position in the *xy* plane with respect to the 3 x 120 μm² sensor area (in purple). For taking into account the actual geometry of the microfabricated sensor, we considered two different *z*-distances from the surface for beads outside (z_o = 700 nm) and upon the sensor area (z_u = 600 nm). From [P5]. (B) Enhancement in the average magnetic field on the sensor due to the patterning (H_{bpat}/H_b) as function of the width of the functionalization area y_a.

6.6 Experimental results and discussion

To experimentally validate these findings, DNA-DNA hybridization experiments were carried out using patterned magnetoresistive sensors coated and spotted according to the procedure described above. The morphology of the surface, after the molecular recognition assay, was assessed by Scanning Electron Microscopy (SEM). Fig. 6.2 A shows images taken at different magnifications of the sensor area. In the left panel, the whole biopatterned region (which is

located on top of the sensor area) is uniformly covered by the Nanomag®-D 250 nm diameter MNP used for labeling. It is worth noting the almost complete absence of MNP non-specifically bound to the surface outside the patterned area. In the right panel, a zoom-view of the functionalized area shows the single MNPs and MNPs fragments bound to the surface. The MNP fragmentation occurs after the drying of the chip due to the fact that the MNPs are not stable in dry environment. An Atomic Force Microscopy (Fig. 6.2 B) investigation shows peaks ranging from 50 nm up to 250 nm, confirming the uniform distribution of MNPs over the functionalized surface. The high specificity of the proposed method is confirmed by the low root mean square roughness (R_{RMS}) value of 4.26 nm calculated over a 5 x 5 μm^2 non-functionalized area, which is comparable to the one measured on the bare sample, before the functionalization process (figure not shown).

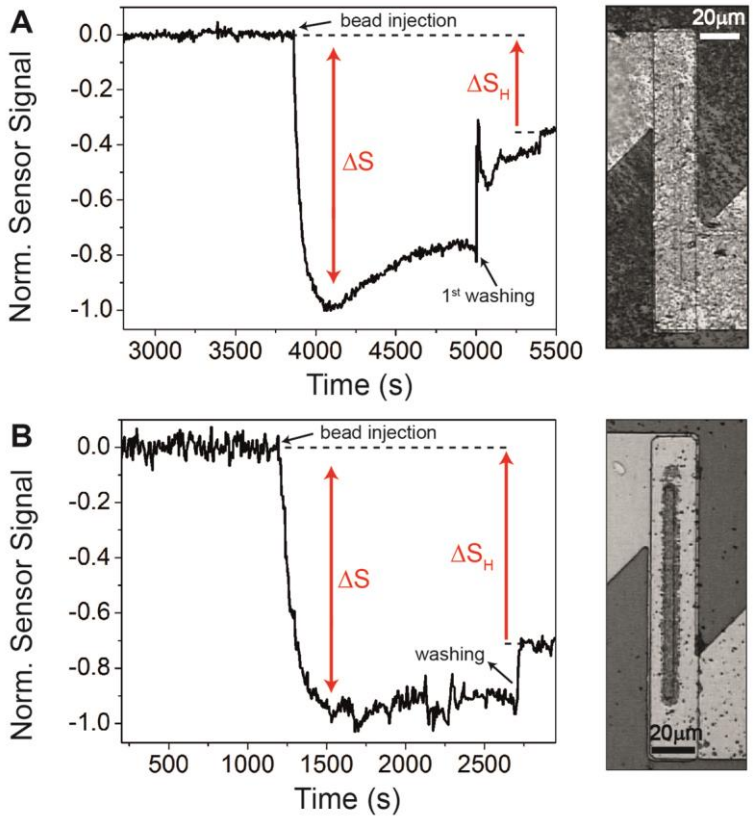

Fig. 6.4 Comparison between the signal from the spotted (A) and selectively functionalized (B) sensors during a biomolecular recognition experiment. The binding signal is ΔS_H. On the right: optical image of the sensor area after sedimentation. Adapted from [P5].

Examples of magnetic detection of biomolecular recognition events are shown in Fig. 6.4 and Fig. 6.5: a baseline signal from each sensor was initially acquired for 15–20 min and then the beads were injected. The flow was then arrested for allowing the sedimentation of the beads. In our experimental configuration, the bead sedimentation leads to a decrease in the voltage signal as described in chapter 5. After the saturation signal was achieved, we waited a 15 min

extra-time for letting them interact with the immobilized biotinylated target. Finally, the chip was washed until the signal of the reference sensor recovered its baseline and the final signal was stable over time. In particular, in Fig. 6.4, the detection of 1 μM of target concentration in case of conventional (panel A) and selective (panel B) functionalization is presented. A DC H_{ext} of 1.6 mT and -4.5 mT respectively is applied along the *y*-direction in order to bias the sensor of Fig. 6.4 A and B in their most sensitive point. On the right, the optical images of the two sensors after performing the hybridization and washing steps are shown. The immobilized beads cover either the entire spotted area extending all around the sensor (Fig. 6.4 A) or only a rectangular area above the sensor active area in case of localized functionalization (Fig. 6.4 B).

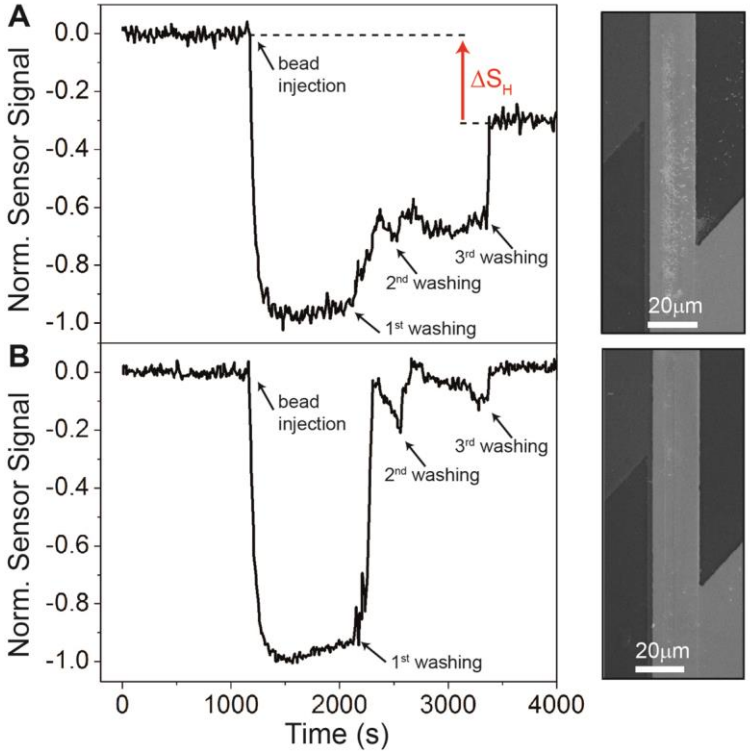

Fig. 6.5 Signal from the positive (A) and reference (B) sensors. A 1 pM DNA target concentration was used. In the reference sensor, the baseline was recovered after the washing steps, while in the positive one the binding signal ΔS_H is highlighted. On the right: SEM images of the two sensors after the experiment. Adapted from [P5].

In both experiments, A and B, the difference between the two baselines, before injecting the beads and after washing, gives the signal ΔS_H which is related to the concentration of target DNA immobilized on the sample surface. The absolute values of the signals, which are related to the same DNA target concentration, depend on the different sensor sensitivities arising from the intrinsic characteristic of each sensor. In order to allow a comparison, each ΔS_H signal is normalized to the bead sedimentation signal ΔS.

In case of conventional and selective functionalization, the $\Delta S_H/\Delta S$ ratios are 0.32±0.01 and 0.75±0.04 respectively, indicating a more than twofold increase in the binding signal on the

biopatterned sensor. This is in nice agreement with our simulation of the sensor response shown in Fig. 6.3, which takes into account the actual sensor geometry. First we must consider that, due to some technical limitations, in these experiments the selectively functionalized area has a width of about 6 μm. According to calculations presented in Fig. 6.3, we are thus exceeding the optimum width matching the flat negative part of the sensor response (which is about y_a=3.7 μm, given our sensor geometry) and partially capturing the opposite signal coming from beads outside the active sensor area. The fact that the bead distribution is non-planar, as pointed out in section 6.5, explains why we can detect a non-negligible signal in case of non-patterned samples: even though this condition resembles the uniform infinite distribution of beads giving a zero net magnetic signal on the sensor area, the beads outside contribute with a much lower signal than those upon the sensor area. The expected ratio between the signal from patterned and non-patterned sensors (proportional to H_{bpat}/H_b in Fig. 6.3 B) should be on the order of 3.6 for y_a=6 μm, which is in nice agreement with the experimental value of 2.7 if we consider that the bead distribution in both cases presents a sort of concentration on the sensor edges due to the stray field originating from the magnetic layers.

Apart from the sensitivity, it is worth noting another difference between the two signals. In case of non-patterned sensors (Fig. 6.4 A), the positive sensor presents an increase of the signal after the initial sedimentation (around 4000 s), which is not a measurement artifact, since no thermal or electrical drift affect the baselines recorded before and after the experiment. This signal rise is almost absent in the selectively functionalized sensors (Fig. 6.4 B for 1 μM and Fig. 6.5 A for 1pM analyte concentration) as well as in the reference sensors (figure not shown). This suggests that the signal rise can be ascribed to the rearrangement of the beads upon the sensor area due to the chemical interaction with the functionalized surface. The initial pronounced signal decrease during sedimentation is due to the focusing action of the stray field of the sensors which attracts the beads mainly upon its area, giving rise to a negative contribution to the total magnetic field sensed by the sensor. Once the beads are in close proximity to the surface, a second mechanism takes place, i.e. the immobilization of the beads upon the sensor surface due to the streptavidin-biotin interaction. This leads to a higher concentration of beads upon the functionalized area with respect to the non-functionalized one. Therefore, the rise after 4000 s in Fig. 6.4 A can be ascribed to the immobilization of beads outside the sensor area, which leads to an additional concentration of beads generating a positive contribution to the sensor signal. In the biopatterned sensor, this positive contribution, and thus the rise in the signal, is absent because the bead immobilization takes place only upon the sensor area, where the beads contribute negatively to the sensor signal. This signal increase is therefore a further confirmation that beads outside the sensor area contribute with opposite sign to the sensor signal with respect to the beads on top of the sensor, and that the beads sedimentate faster upon the sensor area than outside.

The slight increase of the signal in the patterned reference sensor (lower panel in Fig. 6.5), which can be observed about 300 s after the sedimentation drop, has a different origin. It is due to the fact that the sedimentation outside the sensor, giving rise to a positive signal (see Fig. 6.3), is slower than upon the sensor area, because of the absence of the focusing effect of the sensor stray field.

Fig. 6.5 shows the results obtained on a chip employing the same selective functionalization protocol described above, which demonstrates a limit of detection below 1 pM without pre-concentration of the target. The sensor and reference signals during the experiment are respectively represented in the upper and lower panel of Fig. 6.5 whereas, on the right, the SEM images after the experiment are reported. In this case the binding signal $\Delta S_H/\Delta S$ is 0.30±0.03 and is obtained after several washing steps, allowing a full recover of the baseline signal in the reference sensor. The absence of beads in the lower panel of Fig. 6.5 confirms that the multiple washes are effective in removing the non-specifically bound beads. By comparing the ΔS_H signals from the positive and reference sensors, after normalization to the sedimentation signal ΔS, it is possible to calculate the signal-to-background ratio that in this case, with a pM concentration of the analyte, is 23. This experiment clearly demonstrates that selective bio-patterning coupled to our MTJ based magnetoresistive sensors allows to achieve a limit of detection largely below 1 pM, i.e. in the fM range, without pre-concentration of the target.

6.7 Conclusions and perspectives

In this section we presented a straightforward photolithographic technique which allows the realization of micron-sized bio-patterned areas exploiting a lift-off resistant bioreactive polymer. Such technique was employed to selectively functionalize arrays of MTJ-based magnetoresistive biosensors. DNA detection bioassays were run in a controlled microfluidic environment, both with patterned and non-patterned sensors. A sizable enhancement of the magnetic biosensing platform performances, in terms of sensitivity and signal stability, can be achieved through the proper selection of the functionalized area. In particular we observed a more than twofold increase of the binding signal from selectively functionalized sensors with respect to the conventionally functionalized ones. Exploiting selective biopatterning a LOD below 1 pM has been demonstrated in case of DNA detection without target pre-concentration. This remarkable result indicates the relevance of our selective bio-patterning method for improving the quantification capabilities and LOD of magnetoresistive based biosensing platforms. Besides, the very same technology for biopatterning could be of high interest for many other biosensing approaches requiring on-chip probe immobilization over selected areas.

7. Towards a Lab-on-chip platform for detecting DNA pathogens

This work is carried out in the framework of the LOCSENS project, in collaboration with both companies and research groups from Lombardy Region, with the aim of developing a platform for the detection of chemical and biological health threats in food and in food processing environments. In particular, the project aims at the detection of two classes of pathogens of great agribusiness interest:

- Hepatitis E virus (HEV)
- Pathogenic bacteria *(Salmonella* and *Listeria monocytogenes*).

Hepatitis E is a viral disease mainly transmitted through contaminated water or food, which is particularly problematic in developing countries, where it is frequently epidemic. *Salmonella* and *Listeria monocytogenes* are pathogens widespread in nature and are among the main causes of food poisoning. Developing new point-of care methods for testing the presence of these pathogens is of strategic importance in the field of food production, for reducing the complexity and costs of the methods currently used, and thus allowing faster and more frequent analyses.

The classical diagnostic methods, such as bacterial DNA detection by PCR and electrophoresis, have the major drawback of being able to identify only one or a few bacteria in a single experiment. In contrast, combining microarrays technology and spintronic biosensors in a lab-on-chip system, it is possible to detect several different pathogens in parallel with a single multiplexed assay.

7.1 Layout of the platform and operation

The prototype of the diagnostic tool is shown in Fig. 7.1. It consists of a compact, handheld device combining the following four components:

1. Microchip with a 12 MTJ-sensors array
2. Electromagnet
3. Top cover: microfluidics and electrical contacts (click-on system)
4. Front-end electronics for read-out

Each component was designed for guaranteeing small dimensions and portability, and for allowing easy point-of-care testing by interfacing with a computer or smartphone. All the functionalities required for the assay will be integrated in the platform, apart from the PCR reaction, which will be performed in a dedicated modulus, and the pumping system, which will be external in the first release of the system. The whole experiment will be automatically controlled via software, except for the chip insertion and the fluids injection, which will be performed by the user.

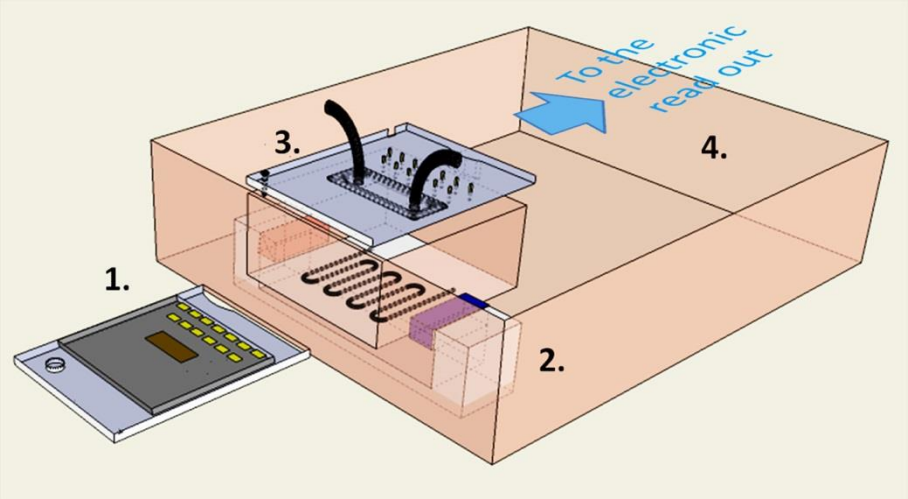

Fig. 7.1 Layout of the platform for magnetic biosensing including the microchip, electromagnet, microfluidics and front-end electronics.

The different phases of the pathogen detection assay are listed below:

Bio-functionalization of the sensors with probe DNA. The sensor chip will be functionalized with single strand probe DNA in correspondence of the sensors active area, in order to achieve higher sensitivity and quantification capabilities, following the procedure based on optolithographic biopatterning presented in chapter 6.

Preparation of the field test (by a food and agricultural industry). First, the sample preparation is performed: the target biological material is collected employing commercial DNA extraction kits, then amplified by means of PCR, and marked by magnetic nano-beads following a pre-hybridization approach. Then, the sensor microchip is positioned between the poles of the electromagnet and combined with the microfluidic system. Then, the calibration of each sensor is performed. This step has the double goal to identify and exclude the damaged sensors and to select the optimal working point of the device (see chapter 5). After the calibration, the experimental parameters are set: temperature (around 50° C), external magnetic field (AC+DC) and sensors bias current (AC). When the sensors output, acquired through the double modulation technique (see section 4.4), is constant in time, the experiment can start.

DNA hybridization. After the injection of the target DNA solution in the microfluidic cell, the flow is arrested for allowing the sedimentation of the magnetic beads and the hybridization between the immobilized probes and target. The magnetic label sedimentation is detected as a variation of the demodulated sensor signal (see sections 5 and 6) and visualized real-time on the computer/smartphone.

Washing. The non-bound target biomolecules are washed away until the control sensors recover their initial baseline. The binding signal from the positive sensors is related to the concentration of immobilized target biomolecules (see section 6.6).

In the framework of this project, ICRM (Istituto di Chimica del Riconoscimento Molecolare) and Dia.Pro (Diagnostic Bioprobes srl), deal with the realization and immobilization of the probes, and with the magnetic labeling of target DNA; the department of Electronics and Information of Politecnico di Milano is committed to the realization of the front-end electronics for the signal reading.

In the following section we present successful experiments of detection of natural HEV target DNA using our MTJ-based biosensing platform (described in section 4). In addition, concerning the lab-on-chip platform, we will focus on the design and realization of sensory part, from the definition of the architecture of the microchip, to the development and testing of the single components of the integrated device.

7.2 Surface functionalization with HEV

The first step consisted in demonstrating the detection of Hepatitis E virus, employing the magnetic biosensing system described in chapters 4 and 5, which was already employed successfully for detecting hybridization events of complementary synthetic 23-mer ssDNA molecules (chapter 6).

The main issue, when dealing with of natural DNA, is related to the length of the oligonucleotides (100-mer in the case of the Hepatitis E virus we employed in this study), which leads to a reduced hybridization efficiency due to steric effects. In fact, while short probes, such as synthetic ones, pack in extended configurations, long probes can assume more flexible, polymeric-like configurations, making the binding process between biotin and streptavidin less efficient (Fig. 7.2).

The procedure employed for performing the magnetic detection experiments was similar to the one described in chapter 6, i.e. the probe DNA immobilization and the subsequent hybridization with the biotinylated complementary target DNA were performed outside the microfluidic environment. The detection experiments weres run in our setup using Micromod®

Nanomag®-D, 250 nm diameter streptavidin coated magnetic beads as magnetic markers, and the double modulation technique presented in section 4.4. Before to perform the experiments, the probe immobilization and DNA-DNA hybridization process were tested on test SiO_2 surfaces employing fluorescent streptavidin as marker.

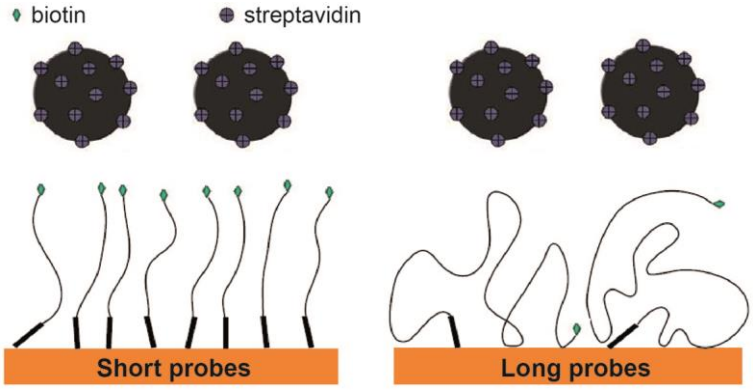

Fig. 7.2 DNA length and packing configuration influencing biotin-streptavidin binding.

The surface functionalization and hybridization procedure employed for both the test surfaces and the sensor arrays is the following:

- The surface was coated with the functional copolymer (DMA-NAS-MAPS).
- The probe oligonucleotides, modified with an amine group for allowing the covalent binding to the polymer, were massively spotted on the sample.
- The surface was incubated with a blocking buffer (ethanolamine, 50 mM in a Tris/HCl buffer 0.1 M, 50° C) in order to prevent nonspecific binding during the subsequent hybridization step.
- Biotinylated target DNA was amplified by means of PCR, and then incubated on the sample surface for enabling hybridization. This process first requires the denaturation of the amplified DNA, i.e. the separation of the two single strands, at a temperature of 95° C, and then the hybridization at a temperature of 40° C.

Fig. 7.3 shows the fluorescence image of a SiO_2 test surface functionalized with HEV virus following the procedure described above, on the left, and positive control consisting of biotinylated target DNA, on the right. A 20 µM probe DNA (100-mer) and a 275 nM amplified target DNA was used. The sample was then incubated with Cy3-streptavidin. The high intensity in the functionalized spots combined with the reduced fluorescence signal in the control let us conclude that the functionalization and the streptavidin-biotin binding were successful, and that the non-specific binding of biotinylated target-DNA to the non-functionalized surface is low.

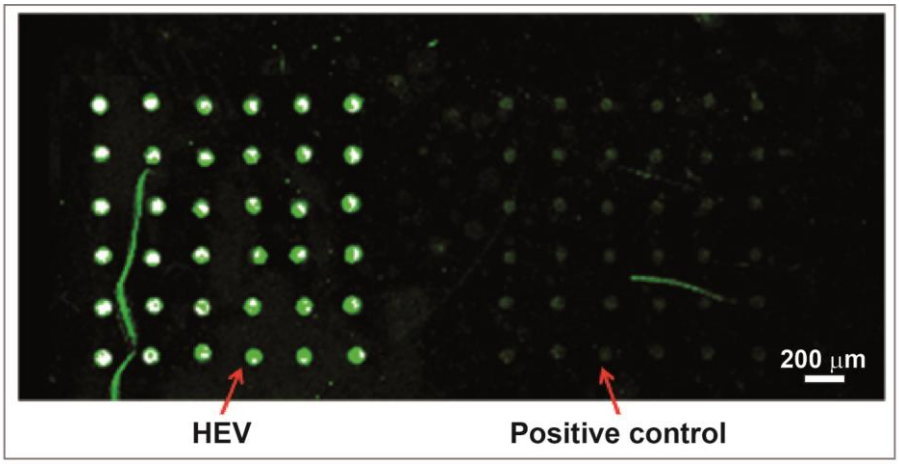

Fig. 7.3 Fluorescence image of the sample functionalized with HEV (left) and positive control (right).

7.3 Magnetic detection of HEV

The sensor array consists of 8 MTJ-based rectangular sensors with lateral dimensions 2.5x30 μm^2 and 40x150 μm^2 contacts area, with the same layout as in Fig. 4.4. The sputtered sensor stack is the same shown in Fig. 4.1. For enhancing the sensitivity of the sensor to the magnetic beads, in this work a SiO_2 50/Al_2O_3 60/SiO_2 180 capping layer was used, which is thinner than the one presented in previous works, in order to allow the beads to be closer to the sensor surface and thus generate a stronger magnetic field on the sensing layer.

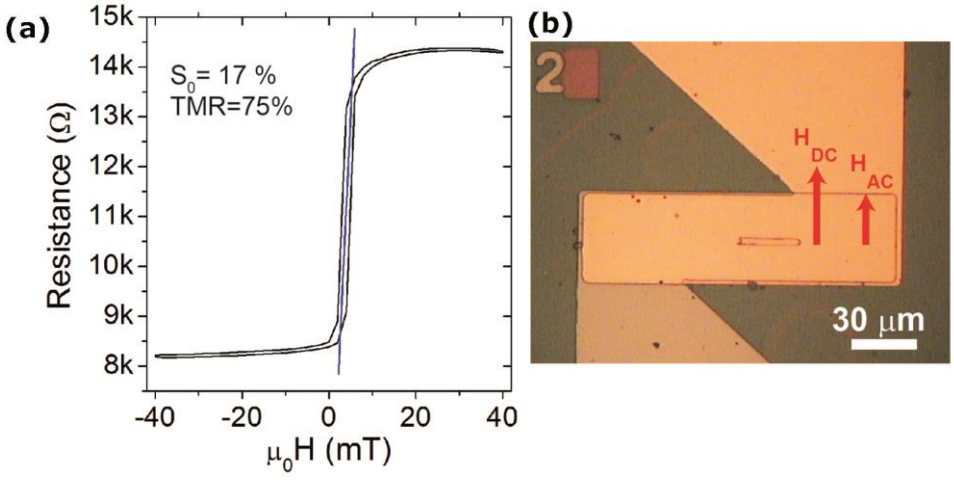

Fig. 7.4 (a) Sensor response to the external magnetic field $R(H)$. (b) Optical microscope image of the MTJ-based sensor, the sensing direction (i.e. the direction of the applied magnetic field) is shown.

The sensors surface was bio-functionalized using the procedure described above, with 100-mer 20 μM probe DNA and 275 nM of amplified target DNA. The spotting procedure involved only sensors 1-3, in order to use the other ones as controls. The transfer curve $R(H)$ of a sensor

is reported in Fig. 7.4: it shows a resistance of about 8 kΩ in the low state, a TMR value of 75% and a sensitivity S_0 = 17 %/mT in the linear region. The parameters set for the double modulation are (refer to section 4.4): V_S = 100 mV, modulated at frequency f_1 = 1.101 kHz, $\mu_0 H_{AC}$ = 0.7 mT, modulated at frequency f_2 = 39 Hz, $\mu_0 H_{DC}$ = 3.3 mT.

The results of the experiment are summarized in Fig. 7.5, showing the signals coming from a positive sensor (a) and a control sensor (b), as a function of time. The beads (3 mg/mL solution of magnetic beads, diluted in PB-Tween) were injected at a rate of 50 µL/min and, were washed after 25 mins at a rate of 450 µL/min, till the control signal recovered completely the baseline (Fig. 7.5 (b)). In Fig. 7.5 (a), the difference between the two baselines (before beads injection and after the washing step) gives rise to a signal ΔS_H ~ 40 µV, which is related to the concentration of target DNA immobilized on the sensor. After normalizing to the sedimentation signal ΔS, the binding signal $\Delta S_H/\Delta S$ results ~ 0.8 ± 0.01. The limit of detection, defined as 3 times the standard deviation of the signal coming from the reference sensor (LOD) was estimated to be 0.014.

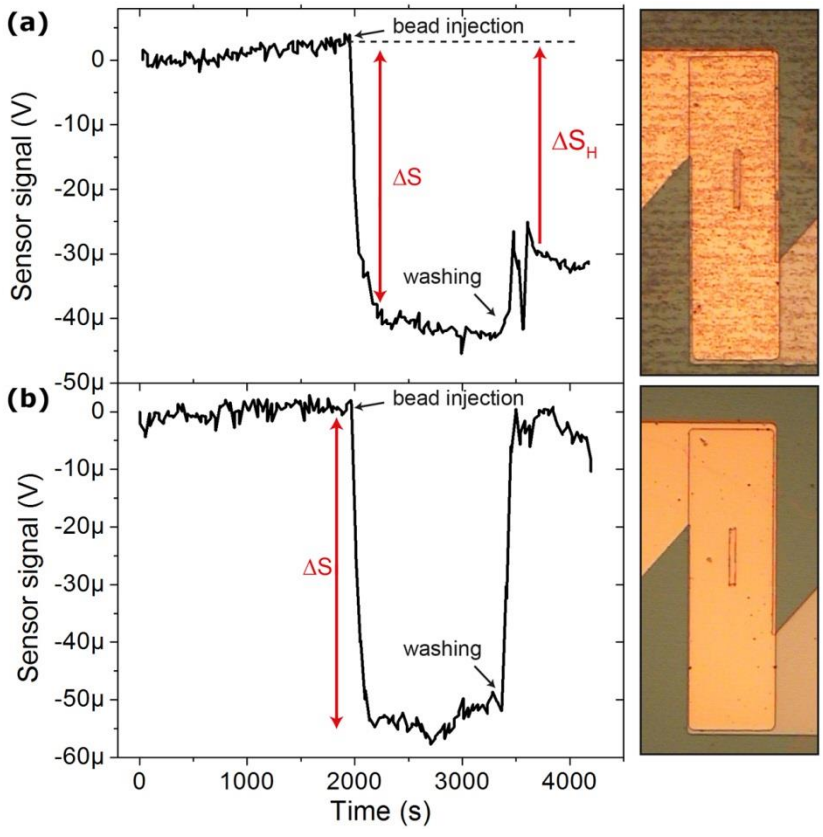

Fig. 7.5 (a), (b) Sensor and control signals, respectively, as a function of time: bead injection is around t = 2000 s, washing is around t = 3400 s. On the right, optical images of the sensor (a) and the control (b), after the washing step.

Fig. 7.5 shows the optical images of a sensor functionalized with HEV (a) and a control sensor (b), after the experiment. The beads are immobilized on the whole spotted area, i.e. both within and outside the sensor area, and form chained structures aligned with the direction of external magnetic field applied during the sedimentation. The absence of magnetic beads in the reference sensor confirms that the washing was effective in removing all the non-specifically bound beads from the sensor surface.

It is worth noting that, in the sensors employed for these experiments, the junction pillar results to be higher, compared to the previous cases (section 6). This results in a non-planar system which allows to reduce the fringe field produced by the markers immobilized outside of the sensor, enhancing the sensor overall signal (see section 6.5 for details).

The results here presented confirm that our MTJ-based biosensing platform is effective in detecting biomolecular recognition events in a real biological system i.e. employing natural target DNA. The next section presents the ongoing work on the integration of the whole experimental setup in a compact, portable platform for the on-chip detection of multiple pathogens.

7.4 Design of the microchip and sample holder

The microchip sketched in Fig. 7.6 consists of a silicon wafer of about 15x15 mm^2 where a matrix of 12 MTJ-based is defined for enabling the simultaneous detection of two different DNA sequences. The function of each sensor is the following:

- 3 sensors are employed for the detection of the first DNA sequence mode (HEV).
- 3 sensors are employed for the second sequence (*salmonella* and/or *listeria*).
- 3 sensors are available for the controls needed to identify false positives.
- 1 sensor is used for the microchip temperature control.
- The remaining 2 sensors are duplicates.

The sensors definition involves 3 lithographic processes after the sputtering deposition of the sensor stack (Fig. 4.1), as explained in section 4.3.2: the definition of the MESA, the definition of the sensor areas, and the patterning of contact areas and subsequent contact deposition. Each sensor has a rectangular shape and is provided with one top contact and one common bottom contact, as shown in

Fig. **7.6** (a).

The first step consists in the physical separation of the different sensors through the definition of MESA (Fig. 7.7 (MASK 1)).

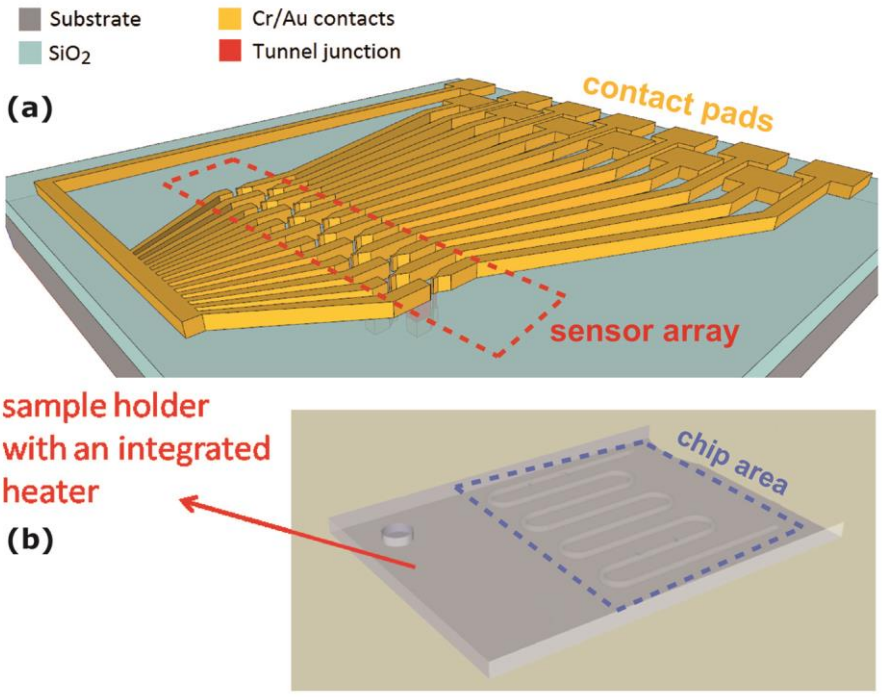

Fig. 7.6 (a) 3D view of the patterned sensor chip. (b) View of sample holder with the integrated heater.

In the second step, the actual shape and active area of each sensor is defined carving a pillar of 3x40 μm^2 in the MESA (Fig. 7.7 (MASK 2)). Such optimal junction size resulted from the need of a high aspect ratio for inducing an easy axis by shape anisotropy, a small junction area for reducing the barrier defects and a reasonably low junction resistance for reducing the MTJ noise (see section 4.3.4). Once defined the junction pillars, a SiO_2 film was deposited in order to electrically insulate the top and the bottom electrode and to prevent the pillars edge from further oxidization.

In the third step, the electrical contacts are defined (Fig. 7.7 (MASK 3)). The top pads are in ohmic contact with the top CoFeB electrode of the MTJ, while the bottom pads, deposited on the MESA, provide the contact with the bottom CoFeb electrode through the whole junction, as in section 4.3.2.

Fig. 7.6 (a), a 3D view of the patterned sensor chip is showed. The common bottom contacts is connected to ground, whereas the top contacts are independently addressable, allowing a multiplexed sequential reading from each sensor. The tracks were dimensioned for ensuring a negligible resistance compared to the junctions (~kΩ), and for avoiding large parasitic capacitances. The contact pads, which consist of squares with 800 µm sides, are easily contacted by the 500 µm diameter metallic retractable tips. The separation distance of 500 µm between contacts ensures no crosstalk between the signals.

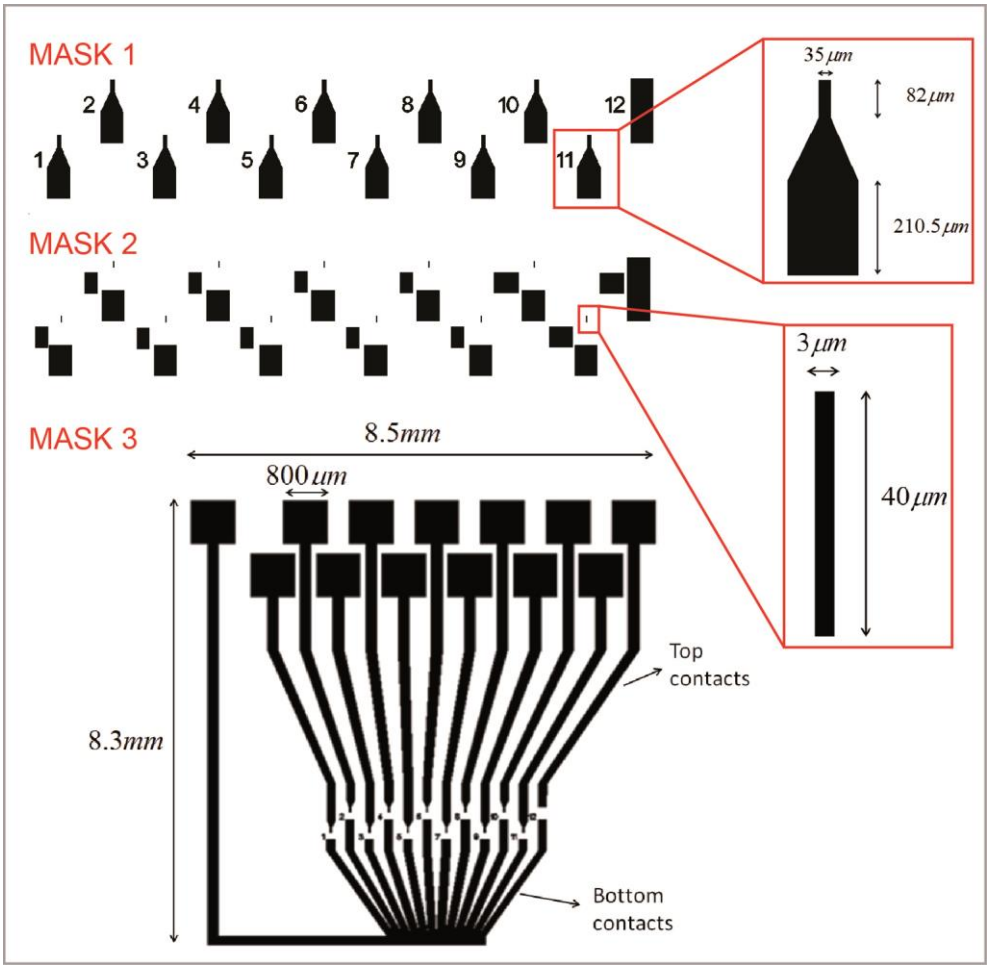

Fig. 7.7 MASK 1 (1st step) MESA definition for the 12 sensors. On the right: zoom of the mesa. MASK 2 (2nd step) Sensor areas definition, for the sensor number 12, designed for the microchip's temperature control, this step is a reply of the first one. On the right: zoom of the junction structure. MASK 3 (3rd step) Contacts definition.

A temperature control is needed to keep the chip around 50° C, which is the temperature required for a typical hybridization process. For this purpose, the chip will be mounted on a sample holder with an integrated heater (Fig. 7.7 (b)). The heater, namely a flexible silicone heatermate with etched foil heating elements, will be controlled by a PID system and a thermocouple in thermal contact with the sample holder. Sensor number 12 is designed with an extremely large sensor area, specifically for addressing the microchip temperature control. In fact, due to its large area, the sensor behaves as an ohmic resistance whose changes can be related to changes in the temperature of the system. The signal from such sensor will then be used in a feedback loop for controlling the heater. A uniform temperature profile throughout the whole chip is ensured by the use of a silicon substrate, which has a high thermal conductivity, and by a suitable choice of the sample holder material, which can be aluminum or an appropriate ceramic (i.e. Macor).

7.5 Electromagnet and microfluidics

The horseshoe stainless steel electromagnet was designed for allowing an easy insertion of the chip holder between the poles (see Fig. 7.1), and for ensuring a sufficiently uniform magnetic field in correspondence of the sensor array (Fig. 7.8). The DC magnetic field required for biasing the sensors in their most sensitive point (see chapter 5) is $H_{DC} \sim 50$ Oe. One of the main goals of the design optimization was to reduce the current required below 500 mA, for minimizing the power dissipation and the heating by Joule effect. Fig. 7.8 (a) (bottom panel) shows the uniform distribution of the intensity of the magnetic field *H* on the sensor area, calculated using FEMM software (Finite Element Method Magnetics) by Andrea Fogliani in the framework of his bachelor thesis.[144]

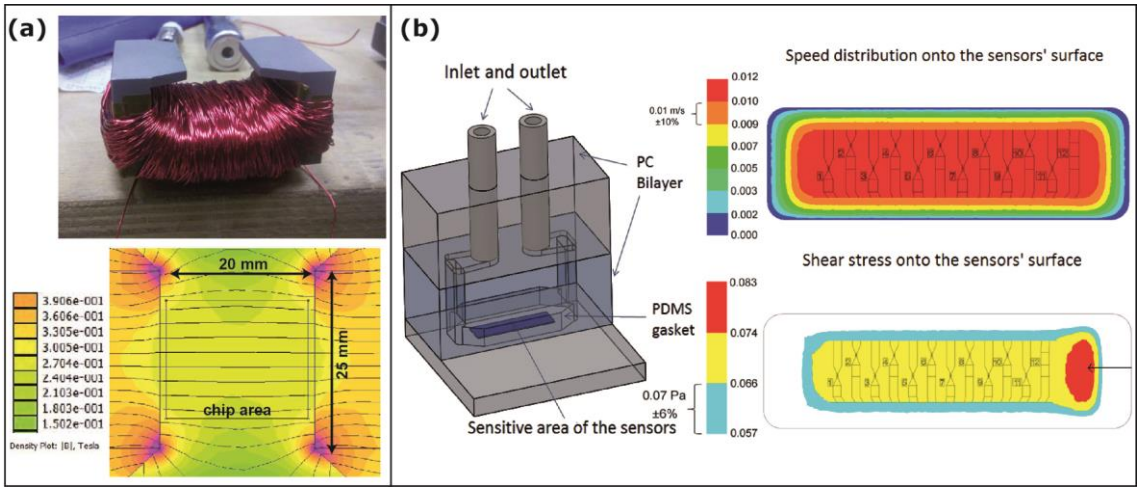

Fig. 7.8 (a) Picture of the electromagnet and top view of the distribution of the intensity of the magnetic field H on the sensor area calculated by FEMM. (b) On the left, microfluidic system with the two chambers in polycarbonate. On the right, color map of the velocity and of the shear stress onto the sensors surface (Courtesy of E. Bianchi, F. Nason and G. Dubini (CMIC)).

The microfluidic platform will be realized in collaboration with the Department of Chemistry, Materials and Chemical Engineering of Politecnico di Milano. It is designed specifically to improve the stability of the immobilized beads. Only two components of the microfluidic cell will be "disposable": the inlet and outlet tubes and the microfluidic chamber, defined by a PDMS gasket. The bearing structure of the system, showed in Fig. 7.8 (b), consists of two separate parts in polycarbonate (PC). The first layer works as a buffer chamber which enables the stabilization of the flow for obtaining a reduced and uniform velocity on the sensor area, especially during the washing step. A uniform washing flow across the whole microfluidic cell is crucial for ensuring reproducibility and a low variability of the results. The color maps in Fig. 7.8 (b) show a rather homogeneous velocity (±10%) on the sensor area, as well as a homogenous shear stress on the surface (±6%).

7.6 Electronic platform and preliminary tests

The electronic platform was designed specifically for addressing the following issues: (i) generating the AC and DC signals for driving the sensing microchip and the power supply for the electromagnet; (ii) providing the multiplexing circuitry for performing independent measurements from each sensor (iii) performing real-time signal processing; (iv) providing the interface to a smartphone or a laptop computer; (v) realizing a portable system characterized by low power consumption, reduced size and weight.

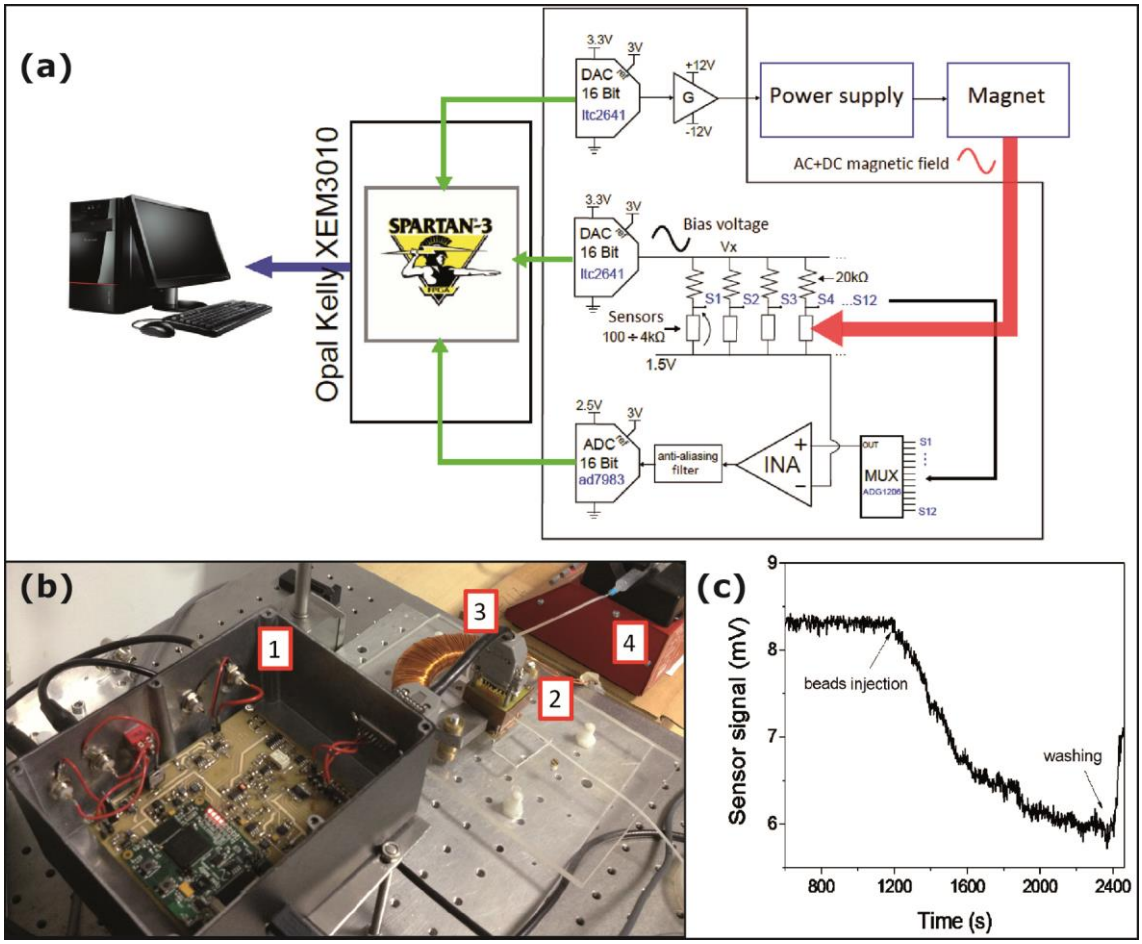

Fig. 7.9 (a) Schematic diagram of the electronic platform. (b) Picture of the final electronic platform connected with our instrumental apparatus: 1 is the electronic platform, 2 is the microfluidic system with the magnetic chip inserted between the poles of the electromagnet, 3 is the multiplexer, 4 the syringe pump. (b) Preliminary experiment of detection of bead sedimentation (similar to section 5) demonstrating the operation of the electronic platform.

Fig. 7.9 (a) shows the circuital scheme of the complete electronic platform. It includes the generation of the AC voltage signal for biasing the sensors (center of the image), the generation of the driving signal for the power supply connected to the electromagnet (top part), and the signal acquisition (bottom part). The signal acquisition is based on the double

modulation technique described in section 4.4. The demodulation process is performed by an integrated lock-in amplifier. The circuit is then connected to a control board (XEM3010) which integrates an FPGA Spartan-3 board for providing the interface to a PC or smartbox. Detailed circuitry design can be found in [145]. Fig. 7.9 (b) shows the picture of the electronic platform integrated with our conventional microfluidic setup. In order to demonstrate the operation of the platform, preliminary experiments of detection of bead sedimentation were performed connecting the platform to our microfluidic system, in the same configuration as in chapter 5 (Fig. 7.9 (c)).

7.7 Conclusions and perspectives

The final goal of this work is to deliver a compact, portable biosensing system for performing multiplexed point-of-care assays of detection of pathogens in the agrifood industry. Remarkably, we demonstrated the use of MTJ based sensors in experiments of detection of biomolecular recognition with natural pathogen DNA (HEV virus, 275 nM). The future perspectives are related to the fine optimization of the system in order to obtain multi-target analyses, and the subsequent integration of the sensors in the lab-on-chip platform. The final step will consist in carrying out point-of-care analysis in labs and factories for demonstrating effectiveness of our platform in detecting and quantifying pathogens in actual on-field tests.

8. Thermochemical nanolithography of protein gradients for neuronal guidance

This work was carried out in the framework of a larger project, which involves the development of a non-conventional "magnetic" approach to nanotechnology-based platforms for the in-vitro investigation of neuronal functions, from single neuronal cell to network levels. The idea is to employ arrays of ultrasensitive MTJ-based magnetic transducers to locally measure the magnetic field generated by the ionic currents associated to the firing of action potentials in neurons.

The main advantages of magnetic detection with respect to the current detection methods such as patch clamp,[146,147] multi-electrode arrays[148,149] or, more recently, nanosized field effect transistors,[150,151] are: (i) non-invasiveness and (ii) high spatial resolution due to the inherent localization of magnetic fields generated by neuronal currents, thus allowing in principle to discriminate signals coming from different subcellular compartments.

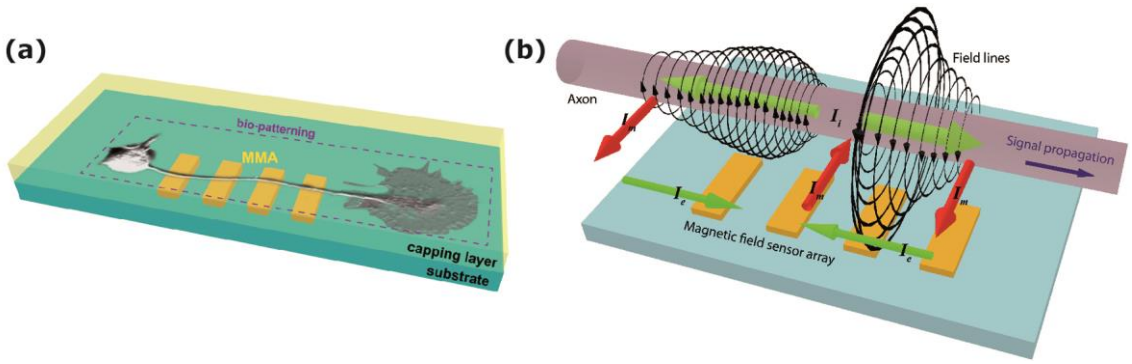

Fig. 8.1 (a) Sketch of a possible measurement configuration: the chip comprises of an array of 4 magnetoresistive sensors. The biopatterning of the active area of the sensor for controlling the orientation of the neuron with respect to the sensors is crucial for enhancing the sensitivity of the experiment. (b) Sketch of the magnetic field lines and ionic currents associated to the propagation of an action potential along the axon.

A possible layout of the chip is schematically illustrated in Fig. 8.1 (a), where a neuron is grown properly aligned to a dense array of magnetic field sensors (MMA). Fig. 8.1 (b) shows the distribution of the ionic currents and the associated magnetic field during the propagation of an action potential in an axon. MTJ-based sensors such as the ones described in section 4, are sensitive only to the component of the external field which is perpendicular to the easy axis of the free layer (*y*-direction in Fig. 5.1 B); this is an advantage when it comes to the study of the

geometry of the magnetic field generated during an action potential; on the other hand a precise orientation of the axon with respect to the sensors is required for maximizing the sensitivity of the experiment.

In this context, the work described in the next sections is focused on employing thermochemical nanolithography (TCNL) (see section 3.8) for creating concentration gradients of extracellular matrix proteins (ECM), such as laminin, with extremely high spatial resolution, for controlling neuronal adhesion and growth.

Apart from our interest in such a technique for patterning neuronal networks on top of arrays magnetic field sensors, the combination of extremely high spatial resolution (around 40 nm[95]) and fine control of the concentration[104] of ECM molecules is not easily achievable with other techniques. Nano-sized protein gradients patterned with TCNL, with dimensions comparable with the cell growth cones or below, could be exploited also in the framework of nano-engineering surfaces for promoting cell development or in fundamental studies on the mechanisms through which the cells interact with the external environment at a subcellular level.

The work, still in progress, was carried out at Georgia Institute of Technology, Atlanta GA, U.S. in Prof. Elisa Riedo's lab, and in Prof. Jennifer Curtis' lab.

8.1 Overview

ECM is a mixture of proteins and polysaccharides that occupies the interstitial space in biological tissues. The crucial role of ECM is evident during the development of the nervous system, where the ECM promotes and regulates cell migration and differentiation, and guides the growth and extension of new axons.[152] It is well known that ECM proteins such as laminin and fibronectin play crucial roles in cell adhesion, growth and tissue remodeling.[153] When specific cell-adhesive peptides or proteins are patterned in a spatially controlled fashion, it is possible to limit the neurite outgrowth only to those areas.[154–156] Furthermore, if concentration gradients of these proteins or peptides are present, neurites are guided towards the higher end of the concentration gradient.[157,158]

Several techniques during the past decades have been developed for creating patterns of ECM proteins for neural guidance, ranging from ink-jet techniques and microfluidic systems,[159] optical lithography,[160] photochemical patterning.[161,162] Nowadays, the most used technique is microcontact printing,[163] which involves the creation of a stamp by soft-lithography from a microfabricated mold, and the subsequent transfer of molecules from the stamp to the final substrate with a fast and inexpensive printing process.

While, as shown, a great number of techniques were developed for creating micrometer-size patterns of ECM proteins, the accurate control over the concentration of the immobilized molecules for creating gradients is still an open challenge, especially in nano-sized patterns.

A wide variety of microfluidic devices also in combination with grayscale soft-lithographic techniques were employed for generating protein gradients,[164,165] but their resolution and versatility are limited and their complexity usually prevents them to be widely used. Laser assisted photobleaching was employed successfully for creating gradients of ECM proteins,[166] but its resolution is limited by the diffraction of the laser beam. Nano-shaving, an AFM-based technique was also used for defining protein patterns;[167] however, it does not allow a straightforward control over the concentration of the immobilized molecules.

TCNL, as explained in section 3.8, is based on the use of a heated AFM cantilever to locally induce thermochemical reactions for exposing amine groups on a polymeric film. Varying the tip temperature, scanning speed, and tip load it is possible to control with extreme precision both the localization and the concentration of the reactive amine groups on the substrate.

8.2 TCNL patterning

TCNL patterning was performed on polymer coated Si substrates. The polymer used, described in section 3.8.3, has a protected functional amine group, which is exposed when the polymer is heated over the deprotection temperature T_d, which is between 150°C and 220°C. Before each pattern, a calibration of the thermal cantilever was performed, for recording the heater resistance and the dissipated heater power (R_H and P_H in Fig. 3.12 (b)) as a function of the applied voltage (V_{out}), as explained in section 3.8.2. Fig. 8.2 shows the calibration curves of the thermal cantilever used for patterning. In panel A, the heater resistance and the heater temperature are plotted as a function of the applied voltage V_{out}. The temperature dependence is calculated applying Eq. (3.5), where the thermal runaway temperature is T_i = 550°C and P_i is the heater power at the thermal runaway. Considering the heat efficiency parameter c defined in Eq. (3.6), it is possible to retrieve the interfacial temperature T_{int}. It is worth noting that both before and after the thermal runaway, the dependence of the temperature on the applied voltage is monotonic and roughly linear in a reasonable voltage range; this allows a fine control over the heating process during TCNL. Fig. 8.2 B shows the dependence of the heater resistance on the heater dissipated power.

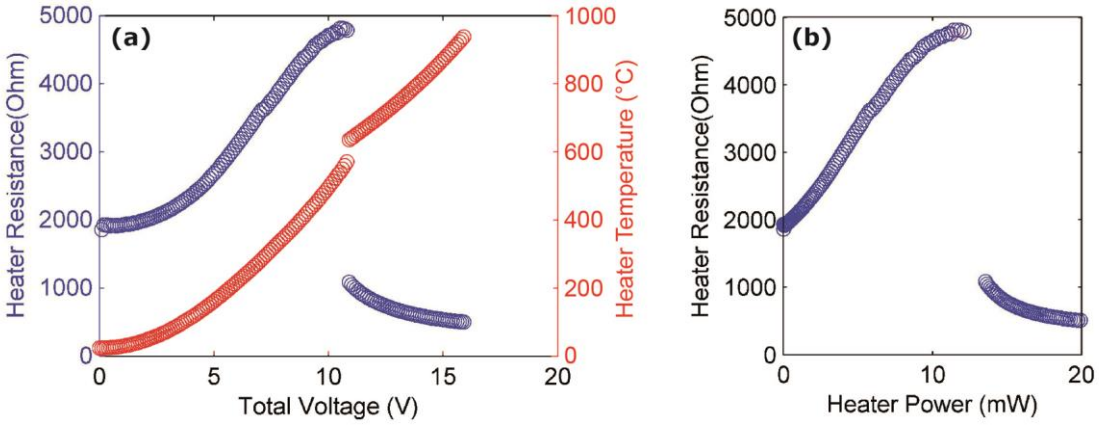

Fig. 8.2 (a) Heater resistance and temperature as a function of the total applied voltage V_{out} for the cantilever used in this work. The discontinuity in the profile marks the thermal runaway point at T_i~550°C. (b) Heater resistance as a function of the heater dissipated power.

Fig. 8.3 shows the topography (panel (a)) and the friction (panel (b)) images taken by AFM in contact mode after the TCNL patterning of a 3x4 array of 5x5 μm^2 squares. Each square was patterned at a fixed V_{out} (different for each square), scanning the tip in the zig-zag fashion shown in Fig. 8.3 (c), with a linear speed of 12 µm/s, keeping a 125 nm distance between each line. At the end of each line, the tip was lifted from the surface and a V_{out} = 16 V was applied for burning the residues of the polymer. During patterning, the heater power P_H was recorded for each square (values in mW plotted in Fig. 8.3 (a)). Due to the relatively low temperature needed to thermally deprotect the amine groups, and due to the better control achievable, all the patterns were realized with temperatures below the thermal runaway point.

The patterns are visible both in the topography and in the friction image. In the first case, the height of the square pattern is related to the quantity of polymer removed due to the chemical deprotection process, which is related to the heating temperature, as explained in section 3.8.3. In the second case, the amine groups exposed produce an increase in the hydrophilicity of the polymer which, in turn, produces larger friction forces at the nanoscale due to larger capillary forces.[95]

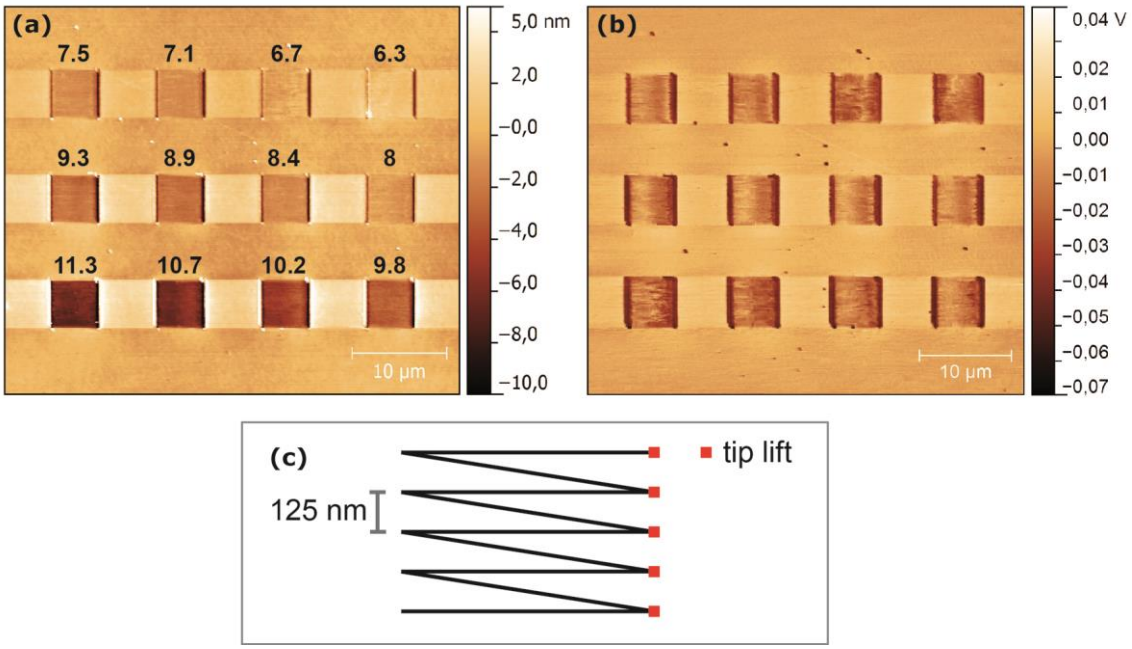

Fig. 8.3 (a) Topography image of the polymer surface after patterning a 3x4 array of 5x5 µm² at different temperatures. The heater power in mW is indicated for each square. (b) Friction image of the same array. (c) Scanning path of the thermal tip during TCNL patterning. At the end of each line, the tip is lifted and the polymer residues are burnt.

8.3 Immobilization of laminin on TCNL gradients

For immobilizing laminin on the TCNL patterns, the high affinity and specificity of the biotin-streptavidin interaction was used in the bridge configuration shown in Fig. 8.4 (b), this allows us to use low concentrations of reagents and short reaction times, which in turn give rise to a lower non-specific binding and a more precise control over the binding process. Using streptavidin as a bridge between two biotinylated compounds is made possible by the fact that each streptavidin molecule exposes 4-binding sites for biotin. Such method is widely employed protein immobilization and separation/purification purposes.[166,168,169]

The **first step** involves the binding of biotin modified with an NHS ester to the TCNL patterns. NHS-activated biotins react efficiently with primary amino groups (-NH2) on the patterned surface in alkaline buffers to form stable amide bonds. The patterned surface was incubated for 1 h with a 1 µM NHS-biotin solution in Dimethyl-Sulfoxide (DMSO). After incubation, the surface was washed repeatedly with DI-H_2O and Phosphate Buffer Solution (PBS) 0.01 M and with a pH of 7.4. The PBS buffer used for washing is the same used in the following incubation steps. The last washing step was performed with PBS for matching the buffer solution of the following incubation step.

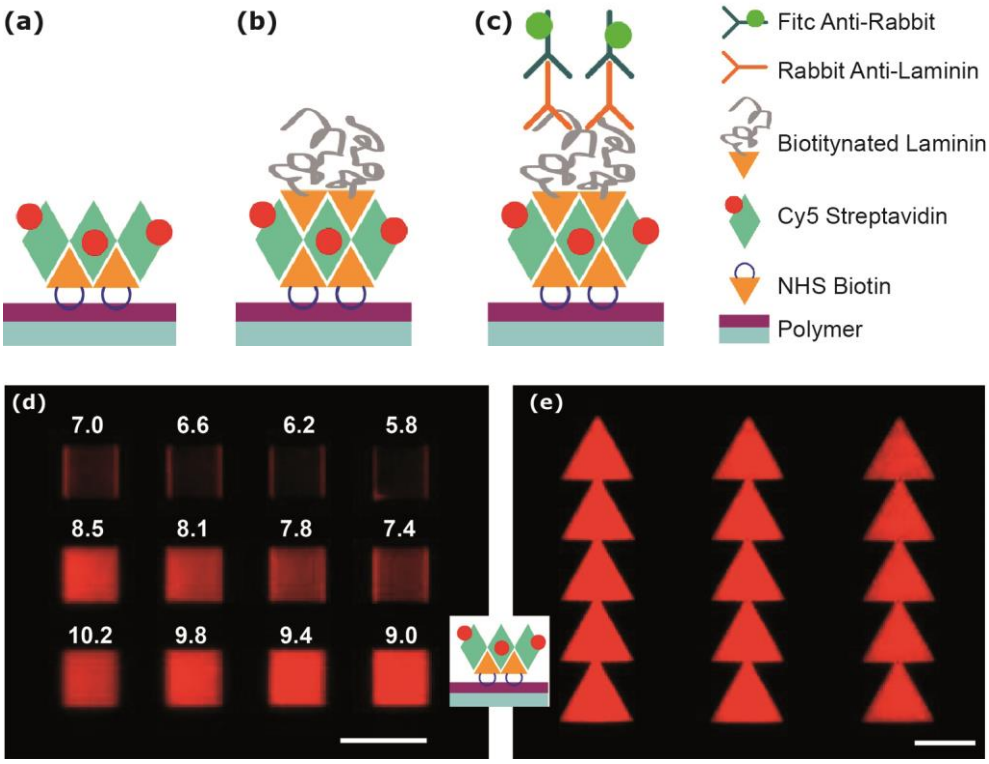

Fig. 8.4 The top panels show sketches of the immobilized biomolecules after the streptavidin immobilization step (a), the laminin immobilization step (b), and the antibodies immobilization steps (c). The lower panels show the fluorescence image of DyLight® 633-streptavidin immobilized upon an array of squares (d) patterned at different heating powers (in mW), and triangular shapes (e) patterned at the heating power corresponding to the maximum intensity of fluorescent signal in (d). Scale bars = 10 μm.

In the **second step**, a 100 nM DyLight® 633-streptavidin solution in PBS was incubated for 30 min. The DyLight® 633 fluorophore, which emits in the red, allows visualization of the streptavidin patterns by fluorescence microscopy. After incubation, the surface was washed repeatedly with DI-H_2O and PBS, starting and finishing with PBS. Fig. 8.4 (a) shows a sketch of the immobilized biomolecules.

Fig. 8.4 (d) and (e) show the streptavidin patterns visualized by fluorescence microscopy. A Nikon Eclipse inverted microscope with an oil immersion 40x objective was used for acquiring the images. In panel (c), a 3x4 array of 6x6 μm^2 squares is shown. For each square, the heater power in mW used for patterning is indicated. The low dye concentration ensures an approximately linear relationship between the fluorescence intensity and the concentration of immobilized streptavidin.[103] The fluorescence intensity increases monotonically with the heater power (i.e. with the interface temperature), as expected by the consideration in section 3.8.3, reaching a maximum around 9.6 mW. If higher temperatures are applied, the polymer starts to show signs of decomposition, and thus a decrease in intensity signal due to the reduced binding is observed, consistently with what observed in Ref. [103] in the case of amine-

reactive dye. Fig. 8.4 (d) shows the fluorescence intensity of arrays of triangular shapes patterned at the heating power corresponding to the maximum fluorescent signal in (e).

In the **third step**, a 40 nM solution of biotinylated-laminin solution in PBS was incubated for 30 min. The Laminin-1 from Engelbreth-Holm-Swarm (EHS) mouse tumor tissue (MW ~ 850 kDa), already biotinylated, was purchased by Cytoskeleton, Inc. ®. After the incubation, the surface was washed repeatedly with DI-H_2O and PBS. Fig. 8.4 (b) shows a sketch of the immobilized laminin using streptavidin as a bridge.

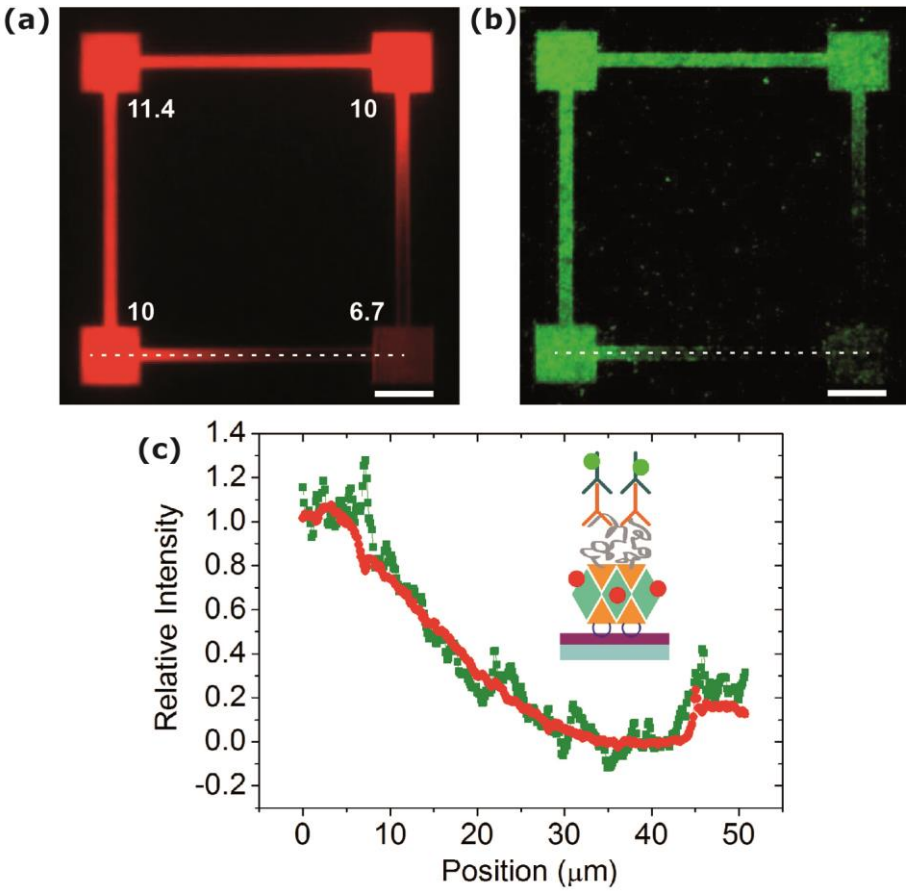

Fig. 8.5 (a) Fluorescence image from the DyLight® 633-streptavidin and heater power of the squares in mW. (b) Fluorescence image from laminin, visualized through the FITC-Sigma Anti-Rabbit secondary antibody. The heating voltage is constant in the squares, and varied linearly in the connections giving rise to a concentration gradient in the exposed amines. (c) Intensity profiles along the dashed line in panels (a) and (b). Scale bars = 10 μm.

After this step, they underwent the following 2 incubation steps for visualizing the laminin patterns through fluorescent antibodies.

In the **fourth step**, the samples were incubated with Sigma Rabbit Anti-Laminin primary antibody (1:160 dilution in PBS, 1% BSA) for 1 h. After incubation, the surface was washed repeatedly with DI-H_2O and PBS, starting and finishing with PBS.

In the **fifth step**, the samples were incubated with Sigma Anti-Rabbit FITC conjugated secondary antibody (1:50 dilution in PBS, 1% BSA), for 45 min. Fluorescein Isothiocyanate (FITC) emits in the green. Since the DyLight® 633 fluorophore conjugated with streptavidin and the FITC emission and absorption spectra do not overlap, it is possible to observe separately the fluorescence intensity arising from the streptavidin and the antibody, which is proportional to the concentration of immobilized laminin. (Fig. 8.4 (c)).

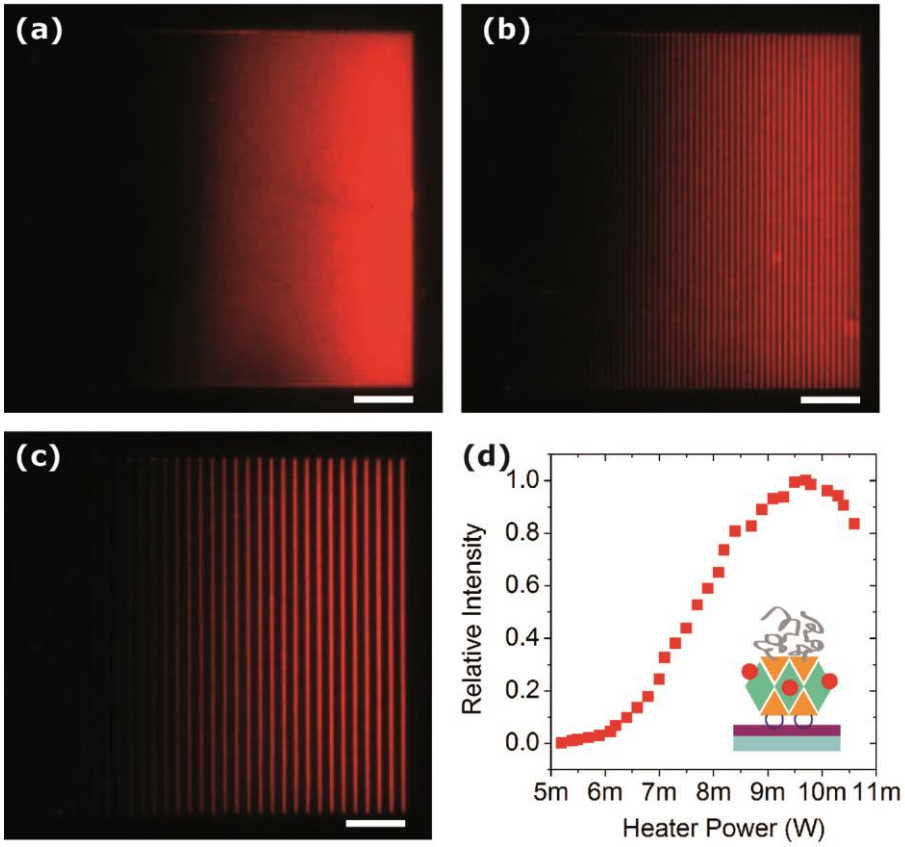

Fig. 8.6 (a), (b), (c) Fluorescent images from the DyLight® 633-streptavidin in patterns of 60 μm long lines with separation of 500 nm, 1 μm, 2 μm, respectively. The heater voltage was increased linearly from right to left. (d) Fluorescent intensity profile from panel (c) as a function of the heater power. Scale bars = 10 μm.

Fig. 8.5 (a) and (b) shows the fluorescence images of a TCNL pattern consisting of four 10x10 μm^2 squares connected by 2 μm width stripes. The heater voltage was varied linearly in the connections, so that a gradient in the exposed amines was created. Panel (a) shows the red fluorescence of the streptavidin, whereas panel (b) shows the green fluorescence of the secondary antibody. Panel (c) shows the profile of the two intensities (dashed line in panels (a) and (b) plotted as a function of distance. The intensities were normalized to the average of their values at the apex (around position 0 μm) and at the bottom (around position 42 μm). It is evident that the two profiles overlap in the gradient area, showing that the concentration of immobilized streptavidin is reflected in the concentration of the immobilized laminin. This demonstrates that using TCNL generated amine gradients it is possible control in a

straightforward way the final concentration of immobilized proteins even after multiple incubation steps.

Fig. 8.6 shows the streptavidin fluorescence intensity of extensive TCNL patterns produced by 60 µm long single vertical lines separated by 500 nm (a), 1 µm (b), 2 µm (c). The heater voltage was kept constant along the vertical lines and increased linearly from right to left, producing the intensity gradient shown. Panel (d) shows the plot intensity profile of (c) as a function of the heater power. The curve obtained is consistent with the one obtained in Ref. [104] in case of the exposed amines, confirming the high degree of control over the concentration of immobilized proteins obtainable with this technique. The uniformity in the fluorescent intensity along the vertical direction in panel (a), (b) and (c) shows that it is possible achieve a remarkable degree of control even in large scale patterns.

8.4 Conclusions

In conclusion, we demonstrated that it is possible to exploit the extremely high resolution and the degree of control over the concentration of the exposed amines in TCNL patterns for generating micro- and nano-sized ECM protein gradients. Further work will focus on the reduction of the non-specific binding of ECM proteins on the non-patterned surface of the polymer, for enhancing the contrast between the concentration of proteins in the patterned and non-patterned areas and improving the efficiency of neuronal guidance. ECM proteins TCNL patterning will be used for controlling the growth and orientation of single neurons and neuronal networks on the surface of magnetic field sensors, for allowing the study of neural activity through the magnetic fields generated by the ionic currents during action potentials.

Nano-sized ECM protein gradients patterned by TCNL also open up new possibilities in fundamental studies on the interaction of cells with nano-engineered surface cues, with possible application both in the field of neurotechnology and tissue engineering.

9. Storing magnetic information in IrMn/MgO/Ta tunnel junctions via field cooling

In this work, we demonstrate that in Ta/MgO/IrMn tunneling junctions, containing no ferromagnetic elements, distinct metastable resistance states can be set by field cooling the devices from above the Néel temperature (T_N) along different orientations. Variations of the resistance up to 10% are found upon field cooling in applied fields, in-plane or out-of-plane. Well below T_N, these metastable states are insensitive to magnetic fields up to 2 T, thus constituting robust memory states. Our work provides the demonstration of an electrically readable magnetic memory device, which contains no ferromagnetic elements and stores the information in an antiferromagnetic active layer. Fig. 9.1 shows a 3D sketch of the working principle of the proposed device.

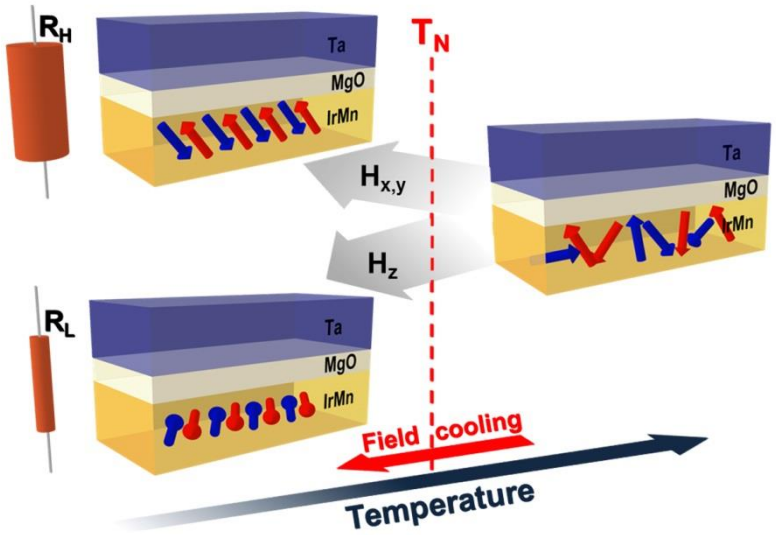

Fig. 9.1 3D sketch showing the working principle of the device: two different metastable resistance states in the IrMn/MgO/Ta junction are achieved by field cooling with different directions of the applied magnetic field.

This work was carried out in collaboration with Dr. X. Marti and Prof. T. Jungwirth (Institute of Physics ASCR, Praha, Czech Republic).

9.1 Overview

Magnetic tunnel junctions used in modern hard-drive read heads and magnetic random access memories comprise two ferromagnetic electrodes whose relative magnetization orientations can be switched between parallel and antiparallel configurations, yielding the tunneling magnetoresistance effect.[171] Recently, large magnetoresistance signals have been observed on NiFe/IrMn/MgO/Pt stacks with an antiferromagnet (AFM) on one side and a non-magnetic metal on the other side of the tunnel barrier.[68,172] In these devices, ferromagnetic moments in NiFe are reversed by external magnetic field and the exchange-spring effect of NiFe on IrMn induces the rotation of the AFM moments in IrMn (Fig. 9.2). This is then electrically detected via the measurement of the AFM tunneling anisotropic magnetoresistance (TAMR). The work has experimentally demonstrated the feasibility of a spintronic concept[64,173] in which the device transport characteristic are governed by an AFM.

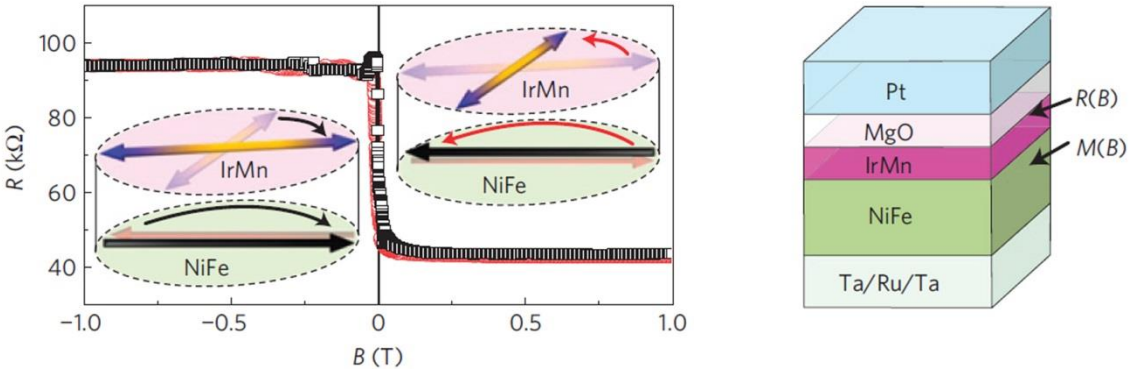

Fig. 9.2 Magnetoresistance signal recorded at T=4 K on a tunneling device fabricated in the depicted multilayer structure with the NiFe/IrMn 1.5 nm/MgO/Pt tunnel junction. The insets illustrate the rotation of AFMmoments in IrMn through the exchange-spring effect of the adjacent NiFe ferromagnet. The external magnetic field is sensed by the NiFe ferromagnet whereas the tunneling transport is governed by the IrMn antiferromagnet. Adapted from [68].

The lack of magnetic stray fields and the relative insensitivity to external magnetic fields make AFM materials potentially fruitful complements to ferromagnets in the design of spintronic devices. The zero net moment of compensated AFMs, however, also implies that weak magnetic fields of the order of the typical magnetic anisotropy fields in magnets cannot be directly applied to rotate the AFM moments. In the devices reported in Refs.[68,172] the problem was circumvented by coupling a ferromagnet to the AFM electrode to form an exchange-spring.[69] This method, however, limits the thickness of the AFM layer to values not exceeding the domain wall width in the AFM. Since the exchange spring triggers rotation of the AFM moments at the opposite interface to the AFM/tunnel-barrier interface, the AFM TAMR effect can be observed only in AFM films which are thinner than the domain wall width in the AFM. Recent experiments in [Pt/Co]/IrMn/AlOx/Pt stacks[174] have demonstrated that room-

temperature AFM TAMR can be achieved in exchange-spring tunnel junctions only in a narrow window of AFM thickness. A subtle balance is required between a thin enough AFM to allow for the exchange-spring rotation of AFM moments across the entire width of the AFM and a thick enough AFM to avoid the decrease of the Néel temperature T_N below room temperature by the size effects. We also point out that, as a memory element, the exchange-spring AFM tunnel junctions can be disturbed by weak magnetic field perturbations as they still contain a ferromagnetic element.

To fully exploit the potential robustness of the AFM based spintronic device against magnetic fields, we have fabricated magnetic tunnel junctions analogous to those in Refs. [68,172], but without the auxiliary ferromagnetic NiFe layer. In these antiferromagnetic tunnel junctions (ATJs) we show that metastable states can be set by cooling the sample and crossing the Néel temperature in external magnetic fields with different orientations. These metastable states can be detected electrically, due to an analogous effect to the AFM TAMR reported in Refs.[68,172,174]. Since our field-cooling approach for writing does not require any ferromagnetic layer, the limitation on the AFM thickness is removed in our devices. Our work provides the demonstration of an electrically readable magnetic memory device which contains no ferromagnetic elements and which stores the information in an AFM.

9.2 Fabrication of IrMn/MgO/Ta tunneling junctions on STO substrates

Prior deposition, the $SrTiO_3$ (STO) single crystal substrates underwent ultrasonic treatment in ethanol for removing surface contamination; then they were annealed in oxygen for reducing the surface roughness, which was measured by AFM and resulted R_{RMS}=1.5 Å. STO was chosen as a suitable insulating substrate with limited impact on the device behavior because our measurements are performed above 100 K, i.e., in a temperature range where STO does not present structural transitions.

The Ta 20/Ru 18/Ta 2/$Ir_{0.2}Mn_{0.8}$ 2-8/MgO 2.5/Ta 20 (layer thicknesses are in nm) stacks for the fabrication of the tunneling junctions used in this study (Fig. 9.3 (a)) were deposited by magnetron sputtering in an AJA ATC Orion 8 system described in section 3.1. The metallic layers have been deposited in DC mode, while MgO in RF mode in the optimized deposition conditions listed in Table 4.1. In order to reproduce the experimental conditions optimized for the fabrication of MgO based tunneling junctions, a magnetic field of 30 mT was applied along the STO [100] direction during the stack growth. A post growth annealing of 250° C was performed in a dedicated system (see section 3.4) with an external magnetic field of 400 mT applied along the same STO [100] direction and with a field cooling until reaching room

temperature (without crossing the Néel Temperature of IrMn). The core of the stack employed for the fabrication of our devices is the $Ir_{0.2}Mn_{0.8}$ 2-8/MgO 2.5/Ta 20 ATJ where the IrMn layer is in direct contact with the insulating barrier. In this way, modifications of its spin-orbit coupled band structure for different AFM configurations can yield the TAMR (see section 2.3).

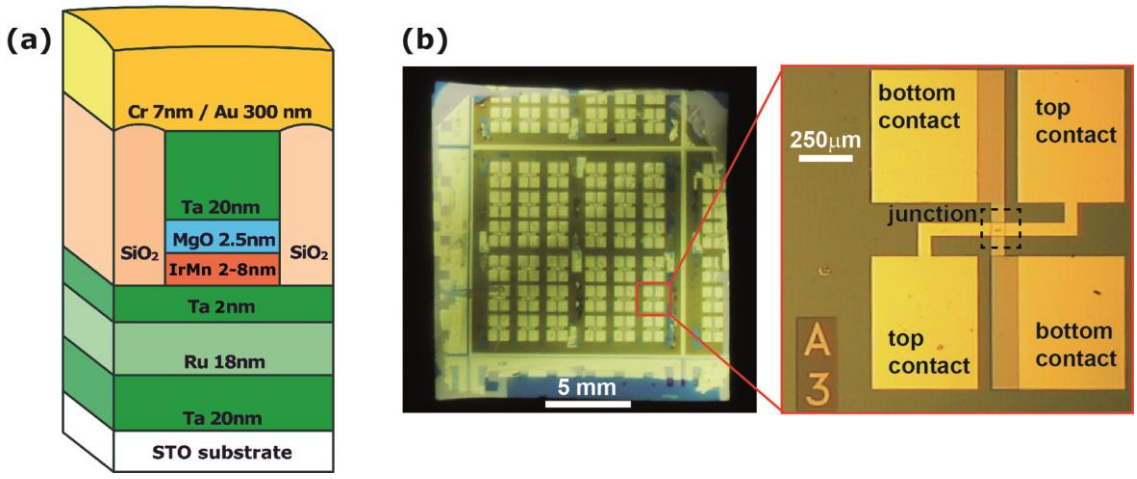

Fig. 9.3 (a) Sketch of the structure of the tunnel junction. (b) Optical images showing the layout used for the microfabrication and zoom on 1 tunnel junction. Each junction is provided with 2 top contacts and 2 bottom contacts.

Tunnel junctions were patterned with a multiple-step process employing optical lithography and ion milling techniques, similarly to what explained in section 4.3.2 for the fabrication of the MTJ-based sensors. Cr 80 /Au 300 contacts were deposited by e-beam evaporation. The final structure, shown in Fig. 9.3 (b), enables electrical access to the top and bottom junction electrodes for 4-point probe measurements. The junctions are rectangularly-shaped with different aspect ratios and areas ranging from 4 μm^2 to 100 μm^2.

9.3 Characterization of the ATJs

The high structural quality of our heterostructures is evident from Fig. 9.4, where we show STEM images taken on a sample with a 8 nm thick IrMn film. In particular, the top panel shows the continuity of the MgO barrier over long distances, which is crucial for the realization of macroscopic tunneling junctions. The expected high quality of the MgO layers on IrMn was one of the reasons for choosing this material for the stack. While the concept shown in this work could in principle be demonstrated using other insulating barriers, such as AlO_x which have been already used in TAMR devices,[174,175] the investigation of different materials for the insulating barrier is beyond our scope. A Nion UltraSTEM operated at 100 kV and equipped with a Nion aberration corrector was used. Low and high resolution STEM Z contrast images show that the stacking comprises continuous films over large distances. This is consistent with

atomic force microscopy analyses at intermediate growth steps, which revealed that each new layer preserved an RMS roughness of less than 1 nm (Table 4.1). Fig. 9.4 (c) highlights the recrystallization of MgO after annealing at 250° C for 1 h. The MgO insulating barrier is highly textured along the out-of-plane [001] direction, parallel to the IrMn [111] texturation, as found in preceding works.[68] STEM images were acquired by M. Varela (Oak Ridge National Laboratory, Oak Ridge TN, USA).

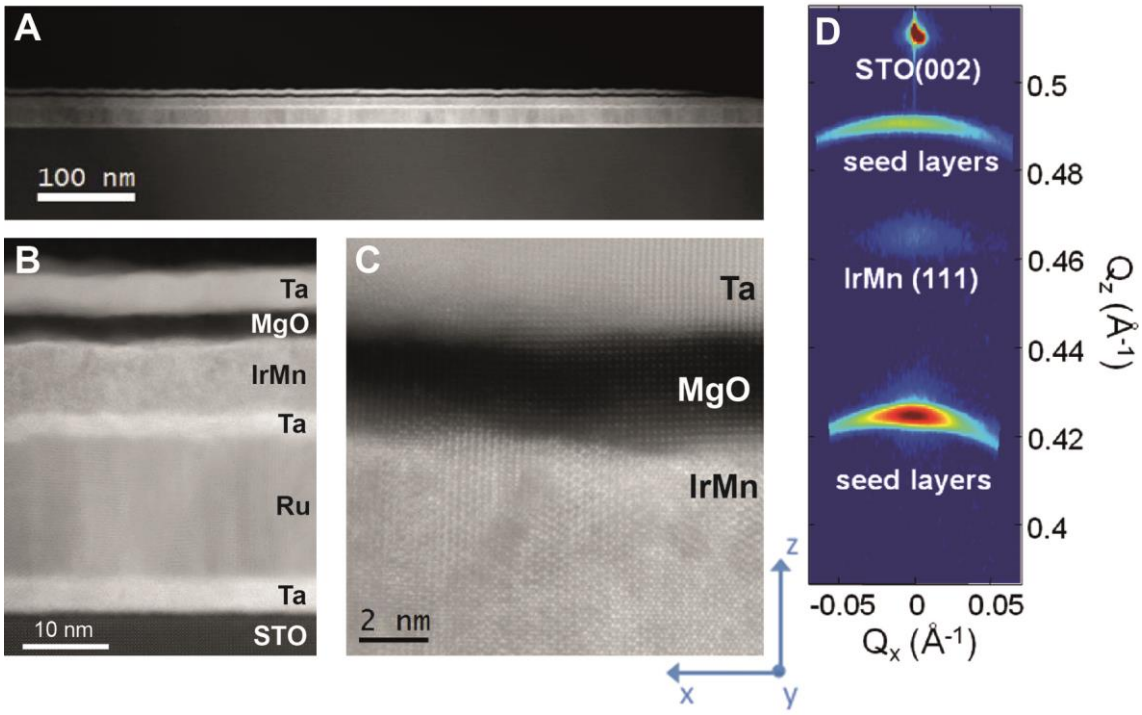

Fig. 9.4 (a), (b), (c) High resolution Z contrast image of the heterostructure studied here. On the inset a high resolution image of the Ta/MgO/IrMn tunneling junction is shown. The reference system reported on the right is that used for indexing the magnetic fields during field cooling. (Top): TEM image showing the continuity of the layers over large lateral distances. Adapted from [P2]. (d) X-ray diffraction coplanar reciprocal space maps. The reflection found at Q ~ 0.46 Å^{-1} is well textured out-of-plane and clearly consistent with the 8 nm thick IrMn(111) oriented layer.

X-ray diffraction measurements shown in Fig. 9.4 (d) have been obtained using a Panalytical's Material Research Diffractometer around the substrate's $SrTiO_3$(002) reflection using Cu K-alpha radiation. Spectra show intense Debye-rings corresponding to the thicker metallic Ta and Ru seed layers in space groups 229 and 194, respectively. On the other hand, the reflection found at Q ~ 0.46 Å^{-1} is well textured out-of-plane and clearly not related to the mentioned polycrystalline rings. Instead, it is consistent with the 8 nm thick IrMn(111) oriented layer. We note that the MgO(002) reflection is placed at a close location but it is too thin to be detected. X-ray diffraction images were acquired by X. Marti (Institute of Physics ASCR, Praha, Czech Republic).

I(*V*) curves of a 2 nm IrMn tunnel junction with an MgO barrier of 2.5 nm were measured in the four-probe configuration with the system described in section 3.7. The *I*(*V*) characteristic (Fig. 9.5 (a)) shows cubic behavior consistent with tunneling, with resistance per area product (RA) on the order of $2.5 \cdot 10^5$ Ω μm^2 at 100 mV and 300 K which is compatible with what expected for a 2.5 nm thick MgO barrier.[61] The top and bottom electrodes show an ohmic behavior with resistance in the order of 30 and 90 Ω, respectively.

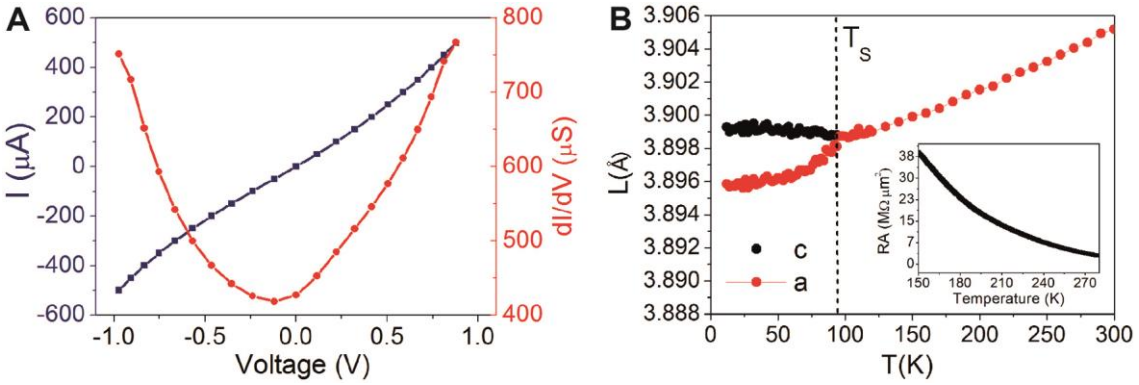

Fig. 9.5 (a) Cubic I-V curve of a 80 μm² area rectangularly shaped junction at 300 K. (b) Temperature dependent X-Ray diffraction measurement of the lattice parameter of the STO substrate showing the cubic to tetragonal transition around 100 K. In the inset, the temperature increase of the junction resistance for decreasing temperature, in the 150 K- 280 K range, is consistent with tunneling transport.

In Fig. 9.5 (b), a complementary X-ray diffraction characterization on the substrate from the very same stack used for device fabrication is shown in order to investigate the phase transitions of $SrTiO_3$ as a function of temperature. As expected, above 100 K the STO substrate presents only a slight decrease of the lattice parameter, while the cubic to tetragonal phase transition (T_s) takes place at 95 K. In the inset of Fig. 9.5 (b), the junction resistance at 100 mV as a function of temperature is plotted for a temperature range going from room temperature down to 150 K, i.e. where $SrTiO_3$ does not present any phase transition. Along with the fact that the device characteristic remains cubic (data not shown), an increase of the junction resistance below room temperature is observed, proving that tunneling is the main transport mechanism also in the temperature range of the present work.

9.4 Results and discussion

As calorimetry measurements showed that T_N of a 2 nm thick IrMn is reduced to ~ 173 K (see Fig. 9.7 and discussion thereafter), we performed the field cooling procedure from room temperature down to 120 K, thus covering a sufficiently large temperature range around T_N. In the case of data reported in the main panel of Fig. 9.6, we applied an external field $\mu_0 H_z$ of ±2 T oriented perpendicular to the sample surface (scattered and red curves) and $\mu_0 H_x$=+2 T

oriented in the plane of the sample, along the [100] axis of the STO substrate (thick green curve). The *RA* product (measured at a fixed bias of 20 mV) is identical for the three field orientations in the temperature interval from 300 K to approximately 170 K, while below this temperature the RA traces for out-of-plane and in-plane field orientations split. At 120 K, the difference is more than 10%. Remarkably, these states are metastable at temperatures sufficiently below T_N, as illustrated in the inset of Fig. 9.6. In the measurement, the higher resistance state was prepared by in-plane field cooling and then the temperature was stabilized at 120 K. The *RA* product (at 20mV bias) was then monitored while continuously sweeping the magnetic field in the out-of-plane direction (H_z) and also in the two orthogonal in-plane directions (H_x and H_y) between +2 T and -2 T for 10 h. No changes in the tunneling resistance are observed within the experimental noise, which is much smaller than the difference between the higher and lower resistance states observed in the main panel of Fig. 9.6.

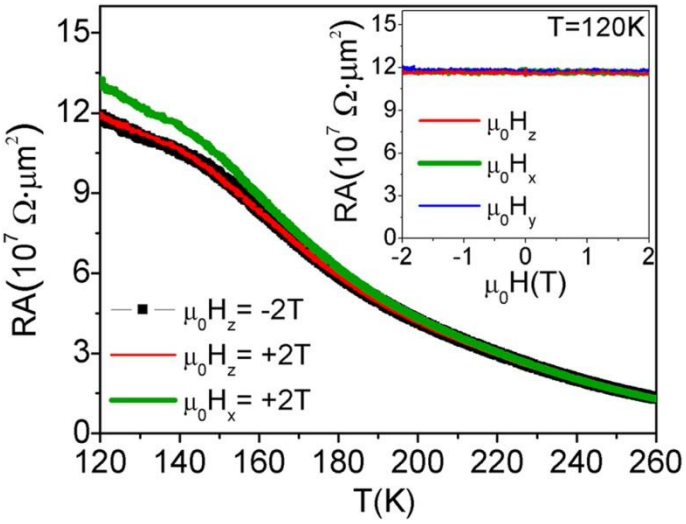

Fig. 9.6 Tunnel resistance data for field-cooling along positive and negative out-of-plane *z*-directions of the field and for the in-plane *x*-direction. The splitting of the two resistance traces, corresponding to the non-zero anisotropic magnetoresistance, is observed near T_N. Inset shows the stability of the state realized by field-cooling in the out-of-plane field. Below T_N, at $T \sim 120$ K, the resistance remains constant when sweeping the magnetic field between +2 and -2 T along out-of-plane (z) or orthogonal in-plane (x,y) directions. From [P2].

This demonstrates that the state prepared by field cooling is metastable and insensitive to relatively large external magnetic fields. Note that metastable states showing different tunneling resistances at zero magnetic field were also observed in Ref. [68], where the configuration of the AFM moments in IrMn was controlled below T_N using the exchange-spring effect of a ferromagnet. Noteworthy, the observed field-cool induced magnetotransport effect shows the key signatures of an anisotropic magnetoresistance. In Fig. 9.6, while the temperature-dependent resistance traces for the in-plane and out-of-plane fields split below

T_N, we observe no difference between field-cool measurements performed at fields with the opposite polarity.

In Fig. 9.7, we highlight that the onset of the splitting of the *RA* traces for cooling in fields with different directions coincides with the transition to the ordered AFM state in the 2 nm IrMn film. Side by side we plot in the figure the normalized variation of the tunneling resistance $[R(H_x) - R(H_z)]/R(H_z)$ in one of our 2 nm IrMn pillar devices and the differential specific heat of a 2 nm IrMn layer as a function of temperature.

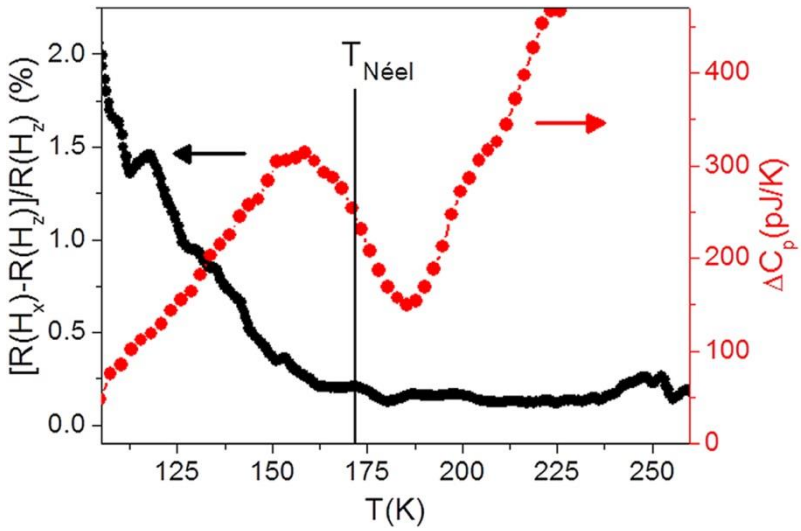

Fig. 9.7 Red scattered curve: differential specific heat measurements of the 2 nm IrMn samples indicating $T_N \sim$ 173 K. Data were obtained on samples with a 2 nm thick IrMn layer, by averaging 1000 consecutive scans. Black curve: temperature dependence of the tunneling magnetoresistance corresponding to the relative difference between field-cool resistance measurements in 2 T fields applied along the out-of-plane (z) and in-plane (x) directions. The onset of a non-zero anisotropic magnetoresistance is observed when crossing T_N. From [P2].

Quasiadiabatic nanocalorimetry (QAnC) is an ideal technique for investigating the Néel temperature of thin IrMn films. This technique allows for a direct measurement of the specific heat of the sample, enabling the observation of the critical behavior in the specific heat near T_N. Identical multilayers to those used in the tunnel junctions were sputtered onto self-standing silicon nitride membranes that form the nanocalorimetric cells. A twin calorimeter loaded with a reference multilayer sample without IrMn was used for differential measurements of the specific heat. The Néel temperature inferred from the inflexion point of the specific heat singularity[176] is approximately 173 K, i.e., it is significantly reduced in the 2 nm IrMn film as compared to the bulk IrMn, having T_N > 1000 K. This is in agreement with previous observations in case of other AFMs, e.g., CoO. The reproducibility of the specific heat method has been confirmed in different samples prepared in separate growth runs under the same growth conditions. Moreover, the correspondence between T_N and the onset of the field-cool AFM TAMR has been confirmed by independent measurements using the PPMS and the vector

magnet cryostat, and studying different ATJs with the same nominal layer structure. All samples show a negligible magnetoresistance in the paramagnetic phase and a reproducible splitting of the RA traces when continuing the field-cooling below T_N with in-plane and out-of-plane magnetic fields. The percentage difference between the two metastable resistance states obtained at 120 K varies from 2% to 10% in different ATJ samples. Higher values were found in devices with larger *RA*, thus indicating that tunneling is the origin of the observed magnetoresistance. The last one simply decreases in devices with thinner barriers, where defects can create parallel conductive paths partially masking the effect of anisotropic tunneling. QAnC measurements were performed by M. Molina-Ruiz and A. F. Lopeandia (Departament de Fìsica, Universitat Autonoma de Barcelona, Bellaterra, Spain).

We point out that the observed magnetoresistance cannot be ascribed to magnetization-independent tunneling transport phenomena due, e.g., to Lorentz force effects of the magnetic fields applied along different directions with respect to the tunneling current direction. These types of phenomena can be excluded since the field-cooling magnetoresistance disappears above T_N and since we observe a negligible resistance variation upon application of external fields when the temperature is stabilized below T_N, as shown in the inset of Fig. 9.6. For the same reason, we exclude that possible Mn interdiffusion within the oxide layer is responsible for the observed metastable magnetic states. The coincidence between the Néel temperature and the onset of the resistance splitting is a strong evidence for the linking of the observed phenomena to the antiferromagnetism of the IrMn layer and not to the magnetic behavior of some Mn atoms dispersed in the tunneling barrier. We also note that the microscopic mechanism which yields the field-cool TAMR in IrMn is distinct from the high-field magnetotransport effects previously observed in iron pnictide AFMs.[177] In the latter materials, the phenomenon has been ascribed to field-induced selection of structural crystal twin domains.[175] IrMn does not undergo a crystal phase change near T_N and we therefore ascribe the distinct metastable states realized by field-cooling purely to distinct AFM configurations of uniform IrMn film. The precise microscopic identification of these states requires a detailed study, which is beyond the proof-of-concept demonstration presented in this work. Here, we recall the theoretical study[178] on IrMn which for $Ir_{20}Mn_{80}$ identified two non-collinear AFM phases 2Q and 3Q (confining the magnetic spins in the plane or yielding an out-of-plane component, respectively) with an energy difference of only ~ 0.25 mRy/atom, and a collinear phase whose energy is ~1.25 mRy/atom higher. We surmise that depending on the direction and strength of the applied field, the field-cooling procedure starting from temperatures above T_N can favor spin configurations with different proportion of these distinct metastable AFM phases. Finally, we remark that in the previously studied NiFe/IrMn exchange-spring AFM tunnel junctions,[172,68] the formation of the distinct magnetic configurations affecting the tunnel transport could be ascribed to bulk properties of the AFM or to the interface effects with the ferromagnet. From this perspective, our present experiments

provide valuable complementary evidence showing that the interface with another magnetic layer is not required for stabilizing distinct states in the IrMn AFM.

9.5 Conclusions

To summarize, we have demonstrated the storage of information in an AFM/insulator/normal-metal tunneling device comprising no ferromagnetic elements. Different metastable configurations, yielding the high and low resistance states of the ATJ, can be set by cooling the AFM from above T_N in magnetic fields with different orientations. By increasing the AFM layer thickness, the Néel temperature of the AFM film is expected to increase, virtually allowing setting the T_N above room temperature. The absence of stray fields and the robustness against magnetic field perturbations are the key features of these devices, which hold potential for the development of spintronic devices without ferromagnets. Note that this work corresponds to the first demonstration of a spintronic device without ferromagnets, i.e. purely based on active antiferromagnetic materials.

10. Conclusion and perspectives

The conclusion of each chapter of the thesis illustrate the results and implications of the work presented. This section is intended to give an outlook on the contribution of this thesis in terms of technological impact and possible future developments.

Magnetoresistive biosensing, in particular employing MTJs and spin-valves, has demonstrated in the past few years huge potentials due to its extremely high sensitivity and ease of integration in LOC platforms. In this context, the study and optimization of the measurement configurations is of capital importance for maximizing the sensor sensitivity to the magnetic markers and thus improving the overall performance of the platform in terms of LOD and quantification capabilities. In this thesis, this issue is extensively investigated both experimentally and by means of calculations. The model proposed for selecting the optimal working point on the magnetoresistive curve of the sensors can be effectively used, other than for maximizing the sensitivity in biological experiments, for realizing novel improved sensors starting from the design of their magnetic response.

Our work on the optolithographic biopatterning of biosensors arrays goes in the direction of improving the sensor performances by controlling the spatial distribution of the probe biomolecules immobilized on the array. In contrast with other biopatterning techniques commonly employed with magnetoresistive sensors, our straightforward method does not require any physical deposition step and is based on a widely accessible process available in all microfabrication facilities, providing sub-micron resolution and easy scale up to mass production. The significant increase in the binding signal achieved in DNA-DNA hybridization experiments on biopatterned sensors, which is consistent with the calculations, proves the effectiveness of combining our biopatterning method and magnetoresistive biosensing platforms. More generally, our approach, based on optical lithography combined with dip polymeric coating, provides an easy and effective solution to the present technological need of highly controlled immobilization of biomolecules in micron-sized areas of biochips, biosensors, LOC devices and for tissue engineering purposes.

The development of compact, easy-to-use lab-on-a chip devices for performing rapid and inexpensive point-of-care analysis is one of the major technological goals of our time joining efforts from both academy and industry. In this context, our final goal is to realize a LOC platform for detecting pathogens in the agrifood industry employing the MTJ-based biosensing technology. The stages of the work, still in progress in collaboration with other groups at Politecnico di Milano and biotechnological companies, consist in the realization and

integration of all the components of the on-chip platform, and the final demonstration of the effectiveness of the device in point-of-care testing. In our preliminary results, we showed the detection of natural *Hepatitis E* virus DNA with our conventional platform, which is remarkably one of the first demonstrations of the use of MTJ-based platforms for detecting the hybridization of natural DNA.

Recently, it has been proposed that the extremely high sensitivity of MTJ sensors to weak magnetic fields could be exploited for studying the activity of neural cells *in-vitro* with unprecedented spatial resolution. In this application, it is fundamental to control the axonal orientation with respect to the sensors, for maximizing the sensitivity of the experiments. In this context, thermochemical nanolithography (TCNL) was successfully used for patterning gradients of extracellular matrix proteins, demonstrating an extremely high degree of control over the concentration of the immobilized proteins, combined with a nanometric resolution. The realization of nanometric extracellular matrix protein gradients, can also pave to way to fundamental studies on the biological length scales related to the cellular guidance and differentiation.

The second part of the thesis is related to the demonstration of novel spintronics devices based on tunneling junctions. In this context, the discovery of tunneling anisotropic magnetoresistance (TAMR) and the fact that large TAMR effects were predicted in antiferromagnetic alloys such as IrMn, led to the development of a new class of spintronic devices whose properties are controlled by antiferromagnets. Following the demonstration of the first antiferromagnet-based device, we demonstrated that it is possible to store magnetic information via field cooling in a IrMn/MgO/Ta tunnel junction comprising no ferromagnetic materials. Further work in this field will concern the demonstration of the room temperature feasibility of this concept, which can be the prelude to the realization of a new type of thermally assisted random access memories (TA-RAM) based on TAMR in antiferromagnets.

Appendix A

Extraction of α_{DC} values from the DC component of the magnetic signal

According to Eq. (5.3), the signal demodulated at frequency f_1, which depends only on the DC component of the magnetic field on the free layer, is:

$$V_{\mathrm{outDC}} = V_s \frac{R\big(H_{\mathrm{DC}}(1+\alpha_{\mathrm{DC}})\big)}{r + R\big(H_{\mathrm{DC}}(1+\alpha_{\mathrm{DC}})\big)} \tag{A.1}$$

Then the signal variation upon bead sedimentation is:

$$\Delta V_{\mathrm{outDC}} = V_s \left(\frac{R\big(H_{\mathrm{DC}}(1+\alpha_{\mathrm{DC}})\big)}{r + R\big(H_{\mathrm{DC}}(1+\alpha_{\mathrm{DC}})\big)} - \frac{R(H_{\mathrm{DC}})}{r + R(H_{\mathrm{DC}})} \right) \tag{A.2}$$

Using this equation and sedimentation data like those shown in Fig. 5.2 B, recorded during the experiments upon signal demodulation at f_1, the values of $\alpha_{\mathrm{DC}} = \beta \chi_{\mathrm{DC}} V_b n$ reported in Table 5.1 were extracted.

Noteworthy, these values are lower than $1.5 \cdot 10^{-2}$ so that the approximation $|\alpha_{\mathrm{DC}}| \ll 1$ used in order to obtain Eq. (5.5) from Eq. (5.4) is largely acceptable.

Refined model including the Néel and stray fields contributions

In real devices, the total magnetic field sensed by the free layer H_{sens} is the sum of contributions coming from the external field H_e, the Néel H_N and demagnetizing fields H_{dp} arising from the pinned layer, and eventually of the contribution from the beads, the latter depending also on the demagnetizing field from the free layer itself H_{df} via the coefficients α introduced in the text. The demagnetizing field from the pinned layer is assumed to be constant, so that it can be included as a bias in the external DC field $H_{e\mathrm{DC}}$. We can then write:

$$H_{\mathrm{sens}} = H_N + H_{e\mathrm{DC}}(1+\alpha_{\mathrm{DC}}) + H_{df\mathrm{DC}}\alpha_{\mathrm{DC}} + h_e(1+\alpha_{\mathrm{AC}}) + h_{df}\alpha_{\mathrm{AC}} \tag{A.3}$$

It is worth to note that H_N is a phenomenological way to describe a tendency to ferromagnetic

coupling of the two FeCoB layers due to the well-known "orange-peel" effect arising from interface roughness (see section 2.6). In this sense, H_N is not a physical field sensed by the beads, and indeed it does not produce any bead magnetization. It is simply responsible for the shift of the *R(H)* curve of the sensor with respect to the applied external field.

The net signal variation at frequency (f_1+f_2) upon sedimentation can be worked out within the approximation $|\alpha_{\mathrm{DC}}|$<<1, thus leading to:

$$\Delta S = S_v|_{\mathrm{beads}} - S_v|_{\mathrm{plain}} =$$

$$= \frac{1}{2}\frac{r}{[r + R(H_{e\mathrm{DC}})]^2} h + h_{df}\alpha_{\mathrm{AC}}\left(\left.\frac{\mathrm{d}R}{\mathrm{d}H}\right|_{H_{e\mathrm{DC}}} + \left.\frac{\mathrm{d}^2R}{\mathrm{d}H^2}\right|_{H_{e\mathrm{DC}}} \left(H_{e\mathrm{DC}} + H_{df\mathrm{DC}}\right)\right) \tag{A.4}$$

From micromagnetic simulations, it turns out that the DC demagnetizing field from the FeCoB free layer of our sensor in the position of the beads is lower than 1 mT, the latter value corresponding to the full saturation of the free layer. As a matter of fact, the first derivative of the resistance is much smaller than the term in brackets proportional to the second derivative. As a consequence, it is the second derivative term which determines the maximum value of sensitivity to the beads (see next section). We can then conclude from Eq. (A.4) that the demagnetizing fields from the electrodes only produce a minor shift of the maxima.

Noteworthy, the maximum sensitivity is still achieved when the product of the second derivative by the DC field, corrected for the perturbation of the demagnetizing field, is maximum. This demonstrates that the criterion proposed in the text is valid also if the stray fields from the layer are considered in the model.

Relative weight of the first and second derivative of the *R*(*H*) sensor characteristic

The relative weight of the two terms appearing within the brackets of Eq. (5.5) can be better appreciated from Fig. A.0.1 where we plot these two contributions as a function of the DC bias field. From the plot, it is evident that the point of the maximum bead sensitivity is essentially determined by the term proportional to the second derivative of the *R(H)* curve, as stated in the criterion proposed in the text. The first derivative term is particularly relevant at low bias fields and determines the point corresponding to the null sensitivity to beads.

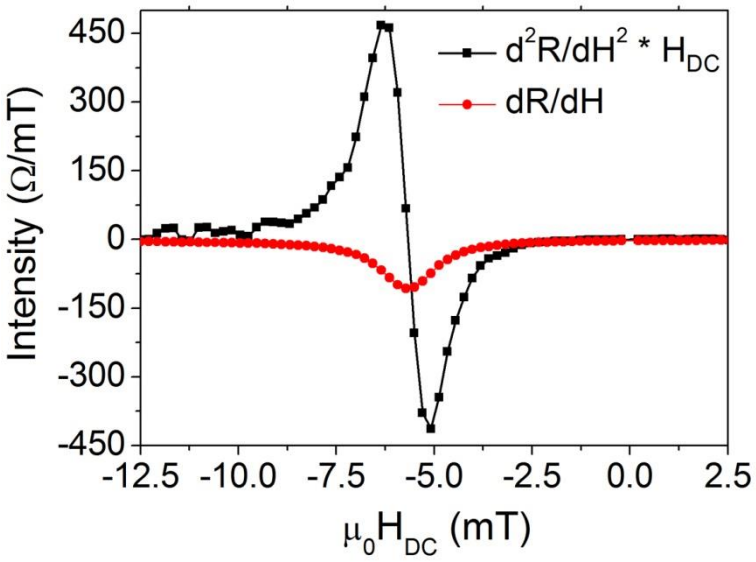

Fig. A.0.1 Relative weight of the two terms within the brackets of Eq. (5.5), as calculated from the characteristic reported in Fig. 5.1 From the supplementary material of [P3].

Appendix B

Calculation of the magnetic field generated by a magnetic bead on the sensor area

The beads were magnetized by an external magnetic field along the *y*-axis, which is the sensing direction in our setup (see Fig. 5.1 B for reference). In order to simulate the magnetic behaviour of the beads, it was assumed that the particles were perfectly spherical and that they can be approximated with an ideal magnetic dipole moment located at the geometrical center of the sphere.[131] The value of the bead magnetization *M(H)* as a function of the external magnetic field *H* was calculated assuming ideal superparamagnetism with a Langevin-like model.

Since the MTJ-based magnetic sensors used in this work are only sensitive to the component of the fringe field of the particles which lies along the *y* direction on the sensor plane, the first step was to calculate the magnetic field generated along the *y*-axis by a single bead:

$$H_y\,(x_b, y_b, x, y, z) = \frac{m}{4\pi}\left(\frac{3y^2}{((x-x_b)^2+(y-y_b)^2+z^2)^{5/2}} - \frac{1}{((x-x_b)^2+(y-y_b)^2+z^2)^{3/2}}\right) \quad \text{(B.1)}$$

Where *(x, y)* determines a generic point on a plane parallel to the sensor surface, placed at a height *z* with respect to the sensor plane, and (x_b, y_b) indicates the bead position with respect to the center of the sensor. $m = 4/3\pi r^3 M$, where *r* is the particle radius.

The average value of this magnetic field $H_{yAv}\,(x_b, y_b)$ over the whole sensor area was calculated integrating the magnetic field generated by the bead in each point of the sensor and dividing by the sensor area. The total average field H_{xAv} on the sensor generated by a monolayer bead distribution was calculated by superposition assuming no interaction among beads.

References

1. McGuire, T. & Potter, R. Anisotropic magnetoresistance in ferromagnetic 3d alloys. *IEEE Trans. Magn.* **11,** 1018–1038 (1975).

2. Stangl, G. *et al.* Cathode sputtered permalloy films of high AMR effect and low coercivity. in *ASDAM 2000. Conf. Proceedings. Third Int. EuroConference Adv. Semicond. Devices Microsystems* 151–155 (IEEE, 2000).

3. Baibich, M. *et al.* Giant Magnetoresistance of (001)Fe/(001)Cr Magnetic Superlattices. *Phys. Rev. Lett.* **61,** 2472–2475 (1988).

4. Valet, T. & Fert, A. Theory of the perpendicular magnetoresistance in magnetic multilayers. *Phys. Rev. B* **48,** 7099–7113 (1993).

5. Hasegawa, N. *et al.* Nano-oxide-layer specular spin valve heads with synthetic pinned layer: Head performance and reliability. *J. Appl. Phys.* **91,** 8774 (2002).

6. Lederman, M. Performance of metallic antiferromagnets for use in spin-valve read sensors. *IEEE Trans. Magn.* **35,** 794–799 (1999).

7. Fert, A. The present and the future of spintronics. *Thin Solid Films* **517,** 2–5 (2008).

8. Yuasa, S. & Djayaprawira, D. D. Giant tunnel magnetoresistance in magnetic tunnel junctions with a crystalline MgO(0 0 1) barrier. *J. Phys. D. Appl. Phys.* **40,** R337–R354 (2007).

9. Julliere, M. Tunneling between ferromagnetic films. *Phys. Lett. A* **54,** 225–226 (1975).

10. Moodera, J. S., Kinder, L. R., Wong, T. M. & Meservey, R. Large Magnetoresistance at Room Temperature in Ferromagnetic Thin Film Tunnel Junctions. *Phys. Rev. Lett.* **74,** 3273–3276 (1995).

11. Wang, D., Nordman, C., Daughton, J. M., Qian, Z. & Fink, J. 70% TMR at Room Temperature for SDT Sandwich Junctions With CoFeB as Free and Reference Layers. *IEEE Trans. Magn.* **40,** 2269–2271 (2004).

12. Bowen, M. *et al.* Nearly total spin polarization in La2/3Sr1/3MnO3 from tunneling experiments. *Appl. Phys. Lett.* **82,** 233 (2003).

13. Butler, W., Zhang, X.-G., Schulthess, T. & MacLaren, J. Spin-dependent tunneling conductance of Fe/MgO/Fe sandwiches. *Phys. Rev. B* **63,** 054416 (2001).

14. Mathon, J. & Umerski, A. Theory of tunneling magnetoresistance of an epitaxial Fe/MgO/Fe(001) junction. *Phys. Rev. B* **63,** 220403 (2001).

15. Parkin, S. S. P. *et al.* Giant tunneling magnetoresistance at room temperature with MgO (100) tunnel barriers. *Group* **3,** 2–7 (2004).

16. Yuasa, S., Nagahama, T., Fukushima, A., Suzuki, Y. & Ando, K. Fe / MgO / Fe magnetic tunnel junctions. *Group* **3,** 868–871 (2004).

17. Gould, C. *et al.* Tunneling Anisotropic Magnetoresistance: A Spin-Valve-Like Tunnel Magnetoresistance Using a Single Magnetic Layer. *Phys. Rev. Lett.* **93,** (2004).

18. Jungwirth, T. *et al.* Tunneling Anisotropic Magnetoresistance : A Spin-Valve-Like Tunnel Magnetoresistance Using a Single Magnetic Layer. **1,** 1–4 (2004).

19. Turner, A. P. F. Biosensors: sense and sensibility. *Chem. Soc. Rev.* **42,** 3184–96 (2013).

20. Herold, K. & Rasooly, A. *Lab on a Chip Technology: Fabrication and Microfluidics*. (Horizon Scientific Press, 2009).

21. Figeys, D. & Pinto, D. Lab-on-a-Chip : A Revolution in Biological and Medical Sciences. *Society* **74,** 330A–335A (2004).

22. Tan, W. *et al.* Optical protein sensor for detecting cancer markers in saliva. *Biosens. Bioelectron.* **24,** 266–71 (2008).

23. Weigl, B. H., Bardell, R. L. & Cabrera, C. R. Lab-on-a-chip for drug development. *Adv. Drug Deliv. Rev.* **55,** 349–77 (2003).

24. Dittrich, P. S., Tachikawa, K. & Manz, A. Micro total analysis systems. Latest advancements and trends. *Anal. Chem.* **78,** 3887–908 (2006).

25. Chin, C. D., Linder, V. & Sia, S. K. Commercialization of microfluidic point-of-care diagnostic devices. *Lab Chip* **12,** 2118–34 (2012).

26. Martins, V. C. *et al.* Femtomolar limit of detection with a magnetoresistive biochip. *Biosens. Bioelectron.* **24,** 2690–2695 (2009).

27. Caruso, F., Rodda, E., Furlong, D. N., Niikura, K. & Okahata, Y. Quartz crystal microbalance study of DNA immobilization and hybridization for nucleic Acid sensor development. *Anal. Chem.* **69,** 2043–9 (1997).

28. Su, M., Li, S. & Dravid, V. P. Microcantilever resonance-based DNA detection with nanoparticle probes. *Appl. Phys. Lett.* **82,** 3562 (2003).

29. Nie, L. B., Yang, Y., Li, S. & He, N. Y. Enhanced DNA detection based on the amplification of gold nanoparticles using quartz crystal microbalance. *Nanotechnology* **18,** 305501 (2007).

30. Ozsoz, M. *et al.* Electrochemical genosensor based on colloidal gold nanoparticles for the detection of Factor V Leiden mutation using disposable pencil graphite electrodes. *Anal. Chem.* **75,** 2181–7 (2003).

31. Wang, J., Liu, G. & Merkoçi, A. Particle-based detection of DNA hybridization using electrochemical stripping measurements of an iron tracer. *Anal. Chim. Acta* **482,** 149–155 (2003).

32. Gaster, R. S. *et al.* Quantification of protein interactions and solution transport using high-density GMR sensor arrays. *Nat. Nanotechnol.* **6,** 314–20 (2011).

33. Teles, F. & Fonseca, L. Trends in DNA biosensors. *Talanta* **77,** 606–623 (2008).

34. Baselt, D. R. *et al.* A biosensor based on magnetoresistance technology. *Biosens. Bioelectron.* **13,** 731–9 (1998).

35. Ejsing, L. *et al.* Planar Hall effect sensor for magnetic micro- and nanobead detection. *Appl. Phys. Lett.* **84,** 4729 (2004).

36. Vavassori, P. *et al.* Domain wall displacement in Py square ring for single nanometric magnetic bead detection. *Appl. Phys. Lett.* **93,** 203502 (2008).

37. Donolato, M. *et al.* Nanosized corners for trapping and detecting magnetic nanoparticles. *Nanotechnology* **20,** 385501 (2009).

38. Miller, M. M., Prinz, G. A., Cheng, S.-F. & Bounnak, S. Detection of a micron-sized magnetic sphere using a ring-shaped anisotropic magnetoresistance-based sensor: A model for a magnetoresistance-based biosensor. *Appl. Phys. Lett.* **81,** 2211 (2002).

39. Ferreira, H. A. *et al.* Rapid DNA hybridization based on ac field focusing of magnetically labeled target DNA. *Appl. Phys. Lett.* **87,** 013901 (2005).

40. Graham, D. L., Ferreira, H., Bernardo, J., Freitas, P. P. & Cabral, J. M. S. Single magnetic microsphere placement and detection on-chip using current line designs with integrated spin valve sensors: Biotechnological applications. *J. Appl. Phys.* **91,** 7786 (2002).

41. Schotter, J. *et al.* A biochip based on magnetoresistive sensors. *IEEE Trans. Magn.* **38,** 3365–3367 (2002).

42. Miller, M. M. *et al.* A DNA array sensor utilizing magnetic microbeads and magnetoelectronic detection. *J. Magn. Magn. Mater.* **225,** 138–144 (2001).

43. Jorge, R. & Janeiro, P. MgO MTJ biosensors for immunomagnetic lateral-flow detection Engenharia Física Tecnológica Júri. *Techniques* (2010).

44. Shen, W., Schrag, B. D., Carter, M. J. & Xiao, G. Quantitative detection of DNA labeled with magnetic nanoparticles using arrays of MgO-based magnetic tunnel junction sensors. *Appl. Phys. Lett.* **93,** 033903 (2008).

45. Shen, W., Liu, X., Mazumdar, D. & Xiao, G. In situ detection of single micron-sized magnetic beads using magnetic tunnel junction sensors. *Appl. Phys. Lett.* **86,** 253901 (2005).

46. Freitas, P. P., Ferreira, R., Cardoso, S. & Cardoso, F. Magnetoresistive sensors. *J. Phys. Condens. Matter* **19,** 165221 (2007).

47. Graham, D. L., Ferreira, H. A. & Freitas, P. P. Magnetoresistive-based biosensors and biochips. *Trends Biotechnol.* **22,** 455–462 (2004).

48. Ferreira, H. A. *et al.* Detection of Cystic Fibrosis Related DNA Targets Using AC Field Focusing of Magnetic Labels and Spin-Valve Sensors. *IEEE Trans. Magn.* **41,** 4140–4142 (2005).

49. Graham, D. *et al.* Magnetic field-assisted DNA hybridisation and simultaneous detection using micron-sized spin-valve sensors and magnetic nanoparticles. *Sensors Actuators B Chem.* **107,** 936–944 (2005).

50. A Barry et al. A CrO2-based magnetic tunnel junction. *J. Phys. Condens. Matter* **12,** L173 (2000).

51. Griffiths, D. J. *Introduction to Quantum Mechanics (2nd Edition)*. (Benjamin Cummings, 2004).

52. Stratton, R. Volt-current characteristics for tunneling through insulating films. *J. Phys. Chem. Solids* **23,** 1177–1190 (1962).

53. Brinkman, W. F. Tunneling Conductance of Asymmetrical Barriers. *J. Appl. Phys.* **41,** 1915 (1970).

54. Simmons, J. G. Generalized Formula for the Electric Tunnel Effect between Similar Electrodes Separated by a Thin Insulating Film. *J. Appl. Phys.* **34,** 1793 (1963).

55. Meservey, R., Tedrow, P. & Fulde, P. Magnetic Field Splitting of the Quasiparticle States in Superconducting Aluminum Films. *Phys. Rev. Lett.* **25,** 1270–1272 (1970).

56. Yuasa, S. & Djayaprawira, D. D. Giant tunnel magnetoresistance in magnetic tunnel junctions with a crystalline MgO(001) barrier. *J. Phys. D. Appl. Phys.* **40,** R337–R354 (2007).

57. Yuasa, S., Fukushima, A., Kubota, H., Suzuki, Y. & Ando, K. Giant tunneling magnetoresistance up to 410% at room temperature in fully epitaxial Co/MgO/Co magnetic tunnel junctions with bcc Co(001) electrodes. *Appl. Phys. Lett.* **89,** 042505 (2006).

58. Ikeda, S. *et al.* Tunnel magnetoresistance of 604% at 300 K by suppression of Ta diffusion in CoFeB/MgO/CoFeB pseudo-spin-valves annealed at high temperature. *Appl. Phys. Lett.* **93,** 082508 (2008).

59. Jiang, L., Naganuma, H., Oogane, M. & Ando, Y. Large Tunnel Magnetoresistance of 1056% at Room Temperature in MgO Based Double Barrier Magnetic Tunnel Junction. *Appl. Phys. Express* **2,** 083002 (2009).

60. Choi, Y. S., Tsunekawa, K., Nagamine, Y. & Djayaprawira, D. Transmission electron microscopy study on the polycrystalline CoFeB⁄MgO⁄CoFeB based magnetic tunnel junction showing a high tunneling magnetoresistance, predicted in single crystal magnetic tunnel junction. *J. Appl. Phys.* **101,** 013907 (2007).

61. Hayakawa, J., Ikeda, S., Matsukura, F., Takahashi, H. & Ohno, H. Dependence of Giant Tunnel Magnetoresistance of Sputtered CoFeB/MgO/CoFeB Magnetic Tunnel Junctions on MgO Barrier Thickness and Annealing Temperature. *Jpn. J. Appl. Phys.* **44,** L587–L589 (2005).

62. Zhang, S., Levy, P., Marley, A. & Parkin, S. Quenching of Magnetoresistance by Hot Electrons in Magnetic Tunnel Junctions. *Phys. Rev. Lett.* **79,** 3744–3747 (1997).

63. Chiba, D., Takamura, K., Matsukura, F. & Ohno, H. Effect of low-temperature annealing on (Ga,Mn)As trilayer structures. *Appl. Phys. Lett.* **82,** 3020 (2003).

64. Shick, A., Khmelevskyi, S., Mryasov, O., Wunderlich, J. & Jungwirth, T. Spin-orbit coupling induced anisotropy effects in bimetallic antiferromagnets: A route towards antiferromagnetic spintronics. *Phys. Rev. B* **81,** (2010).

65. Shick, A., Máca, F., Ondráček, M., Mryasov, O. & Jungwirth, T. Large magnetic anisotropy and tunneling anisotropic magnetoresistance in layered bimetallic nanostructures: Case study of Mn/W(001). *Phys. Rev. B* **78,** 054413 (2008).

66. Wunderlich, J. *et al.* Coulomb Blockade Anisotropic Magnetoresistance Effect in a (Ga,Mn)As Single-Electron Transistor. *Phys. Rev. Lett.* **97,** 077201 (2006).

67. Park, B. G. *et al.* Tunneling Anisotropic Magnetoresistance in Multilayer-(Co/Pt)/AlO_{x}/Pt Structures. *Phys. Rev. Lett.* **100,** 087204 (2008).

68. Park, B. G. *et al.* A spin-valve-like magnetoresistance of an antiferromagnet-based tunnel junction. *Nat. Mater.* **10,** 347–351 (2011).

69. Scholl, A., Liberati, M., Arenholz, E., Ohldag, H. & Stöhr, J. Creation of an Antiferromagnetic Exchange Spring. *Phys. Rev. Lett.* **92,** 247201 (2004).

70. Meiklejohn, W. & Bean, C. New Magnetic Anisotropy. *Phys. Rev.* **105,** 904–913 (1957).

71. Kools, J. C. S. Exchange-biased spin-valves for magnetic storage. *Magn. IEEE Trans.* **32,** 3165 – 3184 (1996).

72. Nogués, J. & Schuller, I. K. Exchange bias. *J. Magn. Magn. Mater.* **192,** 203–232 (1999).

73. Finazzi, M. Interface coupling in a ferromagnet/antiferromagnet bilayer. *Phys. Rev. B* **69,** 1–7 (2004).

74. Scholl, A. *et al.* Domain-size-dependent exchange bias in Co/LaFeO3. *Appl. Phys. Lett.* **85,** 4085 (2004).

75. Nolting, F. *et al.* Direct observation of the alignment of ferromagnetic spins by antiferromagnetic spins. *Nature* **405,** 767–9 (2000).

76. Devasahayam, a. J. The dependence of the antiferromagnet/ferromagnet blocking temperature on antiferromagnet thickness and deposition conditions. *J. Appl. Phys.* **83,** 7216 (1999).

77. Grünberg, P., Schreiber, R. & Pang, Y. Layered Magnetic Structures: Evidence for Antiferromagnetic Coupling of Fe Layers across Cr Interlayers. *Phys. Rev. Lett.* **57,** 2442–2445 (1986).

78. Parkin, S. S. P., More, N. & Roche, K. P. Oscillations in exchange coupling and magnetoresistance in metallic superlattice structures: Co/Ru, Co/Cr, and Fe/Cr. *Phys. Rev. Lett.* **64,** 2304–2307 (1990).

79. Fassbender, J. *et al.* Oscillatory interlayer exchange coupling of Co/Ru multilayers investigated by Brillouin light scattering. *Phys. Rev. B* **46,** 5810–5813 (1992).

80. Bruno, P. Theory of interlayer magnetic coupling. *Phys. Rev. B* **52,** 411–439 (1995).

81. Stiles, M. Exchange coupling in magnetic heterostructures. *Phys. Rev. B* **48,** 7238–7258 (1993).

82. Néel, L. On a new mode of coupling between the magnetizations of two thin ferromagnetic layers. *Comptes Rendus Math.* **255,** 1676 (1962).

83. Zhang, J. & White, R. M. Topological coupling in spin valve type multilayers. *IEEE Trans. Magn.* **32,** 4630–4635 (1996).

84. Kools, J. C. S., Kula, W., Mauri, D. & Lin, T. Effect of finite magnetic film thickness on Neel coupling in spin valves. *J. Appl. Phys.* **85,** 4466 (1999).

85. Bland, J. A. C. & Heinrich, B. *Ultrathin Magnetic Structures III*. *New York* (Springer, 2005).

86. Bertotti, G. *Hysteresis in Magnetism: For Physicists, Materials Scientists, and Engineers (Electromagnetism)*. (Academic Press, 1998).

87. Bedanta, S. & Kleemann, W. Supermagnetism. *J. Phys. D. Appl. Phys.* **42,** 013001 (2009).

88. Pankhurst, Q. A., Connolly, J., Jones, S. K. & Dobson, J. Applications of magnetic nanoparticles in biomedicine. *J. Phys. D. Appl. Phys.* **36,** R167–R181 (2003).

89. Shen, W. *et al.* Effects of superparamagnetism in MgO based magnetic tunnel junctions. *Phys. Rev. B* **79,** 2–5 (2009).

90. Jang, Y. *et al.* Magnetic field sensing scheme using CoFeB/MgO/CoFeB tunneling junction with superparamagnetic CoFeB layer. *Appl. Phys. Lett.* **89,** 163119 (2006).

91. Bretislav Heinrich & J.A.C. Bland. *Ultrathin Magnetic Structures II: Measurement Techniques and Novel Magnetic Properties*. (Springer, 2004).

92. Cappella, B. & Dietler, G. Force-distance curves by atomic force microscopy. *Surf. Sci. Rep.* **34,** 1–104 (1999).

93. Kim, S. *et al.* Direct Fabrication of Arbitrary-Shaped Ferroelectric Nanostructures on Plastic, Glass, and Silicon Substrates. *Adv. Mater.* **23,** 3786–3790 (2011).

94. Wang, D. B. *et al.* Local wettability modification by thermochemical nanolithography with write-read-overwrite capability. *Appl. Phys. Lett.* **91,** 243104 (2007).

95. Wang, D. *et al.* Thermochemical Nanolithography of Multifunctional Nanotemplates for Assembling Nano-Objects. *Adv. Funct. Mater.* **19,** 3696–3702 (2009).

96. Wei, Z. *et al.* Nanoscale tunable reduction of graphene oxide for graphene electronics. *Science* **328,** 1373–6 (2010).

97. Lee, J. *et al.* Electrical, Thermal, and Mechanical Characterization of Silicon Microcantilever Heaters. *J. Microelectromechanical Syst.* **15,** 1644–1655 (2006).

98. King, W. P. *et al.* Design of atomic force microscope cantilevers for combined thermomechanical writing and thermal reading in array operation. *J. Microelectromechanical Syst.* **11,** 765–774 (2002).

99. Nafday, O. A., Weeks, B. L., King, W. P. & Lee, J. Inducing Nanoscale Morphology Changes of Pentaerythritol Tetranitrate Using a Heated Atomic Force Microscope Cantilever. *J. Energ. Mater.* **27,** 1–16 (2008).

100. Wang, D. Thermochemical nanolithography fabrication and atomic force microscopy characterization of functional nanostructures, Ph.D. Thesis, Georgia Institute of Technology, Atlanta Ga, U.S. (2010).

101. B. W. Chui, M. Asheghi, Y. S. Ju, K. E. Goodson, T. W. Kenny, H. J. M. Intrinsic-carrier thermal runaway in silicon microcantilevers. *Microscale Thermophys. Eng.* **3,** 217–228 (1999).

102. Nelson, B. & King, W. Modeling and Simulation of the Interface Temperature Between a Heated Silicon Tip and a Substrate. *Nanoscale Microscale Thermophys. Eng.* **12,** 98–115 (2008).

103. Carroll, K. M. Modeling and controlling Thermochemical Nanolithography, Ph. D. Thesis, Georgia Institute of Technology, Atlanta Ga, U.S. (2013).

104. Carroll, K. M. *et al.* Fabricating Nanoscale Chemical Gradients with ThermoChemical NanoLithography. *Langmuir* **29,** 8675–82 (2013).

105. Stabley, D. R., Jurchenko, C., Marshall, S. S. & Salaita, K. S. Visualizing mechanical tension across membrane receptors with a fluorescent sensor. *Nat. Methods* **9,** 64–7 (2012).

106. Cao, J., Kanak, J., Stobiecki, T., Wisniowski, P. & Freitas, P. P. Effect of Buffer Layer Texture on the Crystallization of CoFeB and on the Tunnel Magnetoresistance in MgO Based Magnetic Tunnel Junctions. *IEEE Trans. Magn.* **45,** 3464–3466 (2009).

107. Liu, H. The optimization of Ta buffer layer in magnetron sputtering IrMn top spinvalve. *Thin Solid Films* **441,** 111–114 (2003).

108. Chung, H.-C., Lee, Y.-H. & Lee, S.-R. Effect of capping layer on the crystallization of amorphous CoFeB. *Phys. Status Solidi* **204,** 3995–3998 (2007).

109. Anderson, G. W., Pakala, M. & Huai, Y. Spin-Valve Thermal Stability : Interdiffusion versus Exchange Biasing. **36,** 2605–2607 (2000).

110. Lee, Y. M., Hayakawa, J., Ikeda, S., Matsukura, F. & Ohno, H. Giant tunnel magnetoresistance and high annealing stability in CoFeB/MgO/CoFeB magnetic tunnel junctions with synthetic pinned layer. *Appl. Phys. Lett.* **89,** 042506 (2006).

111. Wiśniowski, P., Almeida, J. M., Cardoso, S., Barradas, N. P. & Freitas, P. P. Effect of free layer thickness and shape anisotropy on the transfer curves of MgO magnetic tunnel junctions. *J. Appl. Phys.* **103,** 07A910 (2008).

112. Lu, Y. *et al.* Shape-anisotropy-controlled magnetoresistive response in magnetic tunnel junctions. *Appl. Phys. Lett.* **70,** 2610 (1997).

113. Cardoso, F. Design, optimization and integration of magnetoresistive biochips, Ph.D. Thesis, Instituto Superior Técnico, Lisbon, Portugal. (2010).

114. Desai, M., Misra, a. & Doyle, W. D. Effect of interface roughness on exchange coupling in synthetic antiferromagnetic multilayers. *IEEE Trans. Magn.* **41,** 3151–3153 (2005).

115. Hayakawa, J., Ikeda, S., Matsukura, F., Takahashi, H. & Ohno, H. Dependence of Giant Tunnel Magnetoresistance of Sputtered CoFeB/MgO/CoFeB Magnetic Tunnel Junctions on MgO Barrier Thickness and Annealing Temperature. *Jpn. J. Appl. Phys.* **44,** L587–L589 (2005).

116. Sekiguchi, K. *et al.* Observation of full shot noise in CoFeB/MgO/CoFeB-based magnetic tunneling junctions. *Appl. Phys. Lett.* **96,** 252504 (2010).

117. Guerrero, R. *et al.* Low-frequency noise and tunneling magnetoresistance in Fe(110)/MgO(111)/Fe(110) epitaxial magnetic tunnel junctions. *Appl. Phys. Lett.* **87,** 042501 (2005).

118. Arakawa, T. *et al.* Sub-Poissonian shot noise in CoFeB/MgO/CoFeB-based magnetic tunneling junctions. *Appl. Phys. Lett.* **98,** 202103 (2011).

119. La Torre, C. Towards a magnetoresistive platform for detection of DNA pathogens in agrifood industry, Master Thesis, Politecnico di Milano,Milan, Italy. (2013).

120. Sampietro, M., Fasoli, L. & Ferrari, G. Spectrum analyzer with noise reduction by cross-correlation technique on two channels. *Rev. Sci. Instrum.* **70,** 2520 (1999).

121. Almeida, J. M. *et al.* 1⁄f noise in linearized low resistance MgO magnetic tunnel junctions. *J. Appl. Phys.* **99,** 08B314 (2006).

122. Sekiguchi, K. *et al.* Observation of full shot noise in CoFeB/MgO/CoFeB-based magnetic tunneling junctions. *Appl. Phys. Lett.* **96,** 252504 (2010).

123. Han, S.-J., Xu, L., Wilson, R. J. & Wang, S. X. A Novel Zero-Drift Detection Method for Highly Sensitive GMR Biochips. *IEEE Trans. Magn.* **42,** 3560–3562 (2006).

124. Baselt, D. R. *et al.* A biosensor based on magnetoresistance technology. *Biosens. Bioelectron.* **13,** 731–739 (1998).

125. Chaves, R. C., Bensimon, D. & Freitas, P. P. Single molecule actuation and detection on a lab-on-a-chip magnetoresistive platform. *J. Appl. Phys.* **109,** 064702 (2011).

126. Freitas, P. P., Ferreira, R., Cardoso, S. & Cardoso, F. Magnetoresistive sensors. *J. Phys. Condens. Matter* **19,** 165221–42 (2007).

127. Wiśniowski, P., Almeida, J. M., Cardoso, S., Barradas, N. P. & Freitas, P. P. Effect of free layer thickness and shape anisotropy on the transfer curves of MgO magnetic tunnel junctions. *J. Appl. Phys.* **103,** 07A910 (2008).

128. Wang, S. X. *et al.* Towards a magnetic microarray for sensitive diagnostics. *J. Magn. Magn. Mater.* **293,** 731–736 (2005).

129. Ferreira, H. A., Feliciano, N., Graham, D. L. & Freitas, P. P. Effect of spin-valve sensor magnetostatic fields on nanobead detection for biochip applications. *J. Appl. Phys.* **97,** 10Q904 (2005).

130. Donolato, M. *et al.* On-chip measurement of the Brownian relaxation frequency of magnetic beads using magnetic tunneling junctions. *Appl. Phys. Lett.* **98,** 073702 (2011).

131. Hansen, T. B. G., Damsgaard, C. D., Dalslet, B. T. & Hansen, M. F. Theoretical study of in-plane response of magnetic field sensor to magnetic beads magnetized by the sensor self-field. *J. Appl. Phys.* **107,** 124511 (2010).

132. Alom Ruiz, S. & Chen, C. S. Microcontact printing: A tool to pattern. *Soft Matter* **3,** 168 (2007).

133. Suh, K. Y. & Lee, H. H. Capillary Force Lithography: Large-Area Patterning, Self-Organization, and Anisotropic Dewetting. *Adv. Funct. Mater.* **12,** 405–413 (2002).

134. Mitsakakis, K., Sekula-Neuner, S., Lenhert, S., Fuchs, H. & Gizeli, E. Convergence of dip-pen nanolithography and acoustic biosensors towards a rapid-analysis multi-sample microsystem. *Analyst* **137,** 3076–82 (2012).

135. Breitenstein, M., Nielsen, P. E., Hölzel, R. & Bier, F. F. DNA-nanostructure-assembly by sequential spotting. *J. Nanobiotechnology* **9,** 54 (2011).

136. Ulman, A. Formation and Structure of Self-Assembled Monolayers. *Chem. Rev.* **96,** 1533 – 1554 (1996).

137. Love, J. C., Estroff, L. A., Kriebel, J. K., Nuzzo, R. G. & Whitesides, G. M. Self-assembled monolayers of thiolates on metals as a form of nanotechnology. *Chem. Rev.* **105,** 1103–69 (2005).

138. Steel, A. B., Herne, T. M. & Tarlov, M. J. Electrochemical Quantitation of DNA Immobilized on Gold. *Anal. Chem.* **70,** 4670–4677 (1998).

139. Lee, C.-Y., Canavan, H. E., Gamble, L. J. & Castner, D. G. Evidence of impurities in thiolated single-stranded DNA oligomers and their effect on DNA self-assembly on gold. *Langmuir* **21,** 5134–41 (2005).

140. Yang, M. *et al.* One-step photochemical attachment of NHS-terminated monolayers onto silicon surfaces and subsequent functionalization. *Langmuir* **24,** 7931–8 (2008).

141. Yin, H. B., Brown, T., Wilkinson, J. S., Eason, R. W. & Melvin, T. Submicron patterning of DNA oligonucleotides on silicon. *Nucleic Acids Res.* **32,** e118 (2004).

142. Pirri, G., Damin, F., Chiari, M., Bontempi, E. & Depero, L. E. Characterization of a polymeric adsorbed coating for DNA microarray glass slides. *Anal. Chem.* **76,** 1352–8 (2004).

143. Sola, L. & Chiari, M. Modulation of electroosmotic flow in capillary electrophoresis using functional polymer coatings. *J. Chromatogr. A* **1270,** 324–329 (2012).

144. Fogliani, A. Progettazione di un elettromagnete nell'ambito del progetto Locsens, Bachelor Thesis, Politecnico di Milano, Milan, Italy. (2013).

145. Gervasoni, G. Progetto e realizzazione di uno strumento a doppio lock-in per la rivelazione in tempo reale di beads magnetiche, Master Thesis, Politecnico di Milano, Milan, Italy. (2013).

146. Hamill, O. P., Marty, A., Neher, E., Sakmann, B. & Sigworth, F. J. Improved patch-clamp techniques for high-resolution current recording from cells and cell-free membrane patches. *Pflugers Arch.* **391,** 85–100 (1981).

147. Pusch, M. & Neher, E. Rates of diffusional exchange between small cells and a measuring patch pipette. *Pflugers Arch.* **411,** 204–11 (1988).

148. Puia, G., Gullo, F., Dossi, E., Lecchi, M. & Wanke, E. Novel modulatory effects of neurosteroids and benzodiazepines on excitatory and inhibitory neurons excitability: a multi-electrode array recording study. *Front. Neural Circuits* **6,** 94 (2012).

149. Toader, O. *et al.* Dentate gyrus network dysfunctions precede the symptomatic phase in a genetic mouse model of seizures. *Front. Cell. Neurosci.* **7,** 138 (2013).

150. Duan, X. *et al.* Intracellular recordings of action potentials by an extracellular nanoscale field-effect transistor. *Nat. Nanotechnol.* **7,** (2012).

151. Qing, Q. *et al.* Nanowire transistor arrays for mapping neural circuits in acute brain slices. *Proc. Natl. Acad. Sci. U. S. A.* **107,** 1882–7 (2010).

152. Yu, L. M. Y., Leipzig, N. D. & Shoichet, M. S. Promoting neuron adhesion and growth. *Mater. Today* **11,** 36–43 (2008).

153. Jung, D. R. *et al.* Topographical and physicochemical modification of material surface to enable patterning of living cells. *Crit. Rev. Biotechnol.* **21,** 111–54 (2001).

154. Luo, Y. & Shoichet, M. S. A photolabile hydrogel for guided three-dimensional cell growth and migration. *Nat. Mater.* **3,** 249–53 (2004).

155. Burnham, M. R., Turner, J. N., Szarowski, D. & Martin, D. L. Biological functionalization and surface micropatterning of polyacrylamide hydrogels. *Biomaterials* **27,** 5883–5891 (2006).

156. Hynd, M. R., Frampton, J. P., Dowell-Mesfin, N., Turner, J. N. & Shain, W. Directed cell growth on protein-functionalized hydrogel surfaces. *J. Neurosci. Methods* **162,** 255–63 (2007).

157. Dertinger, S. K. W., Jiang, X., Li, Z., Murthy, V. N. & Whitesides, G. M. Gradients of substrate-bound laminin orient axonal specification of neurons. *Proc. Natl. Acad. Sci. U. S. A.* **99,** 12542–7 (2002).

158. Adams, D. N. *et al.* Growth cones turn and migrate up an immobilized gradient of the laminin IKVAV peptide. *J. Neurobiol.* **62,** 134–47 (2005).

159. Martinoia, S., Bove, M., Tedesco, M., Margesin, B. & Grattarola, M. A simple microfluidic system for patterning populations of neurons on silicon micromachined substrates. *J. Neurosci. Methods* **87,** 35–44 (1999).

160. Sorribas, H., Padeste, C. & Tiefenauer, L. Photolithographic generation of protein micropatterns for neuron culture applications. *Biomaterials* **23,** 893–900 (2002).

161. Nicolau, D. V, Taguchi, T., Taniguchi, H., Tanigawa, H. & Yoshikawa, S. Patterning neuronal and glia cells on light-assisted functionalised photoresists. *Biosens. Bioelectron.* **14,** 317–25 (1999).

162. Clémence, J. F., Ranieri, J. P., Aebischer, P. & Sigrist, H. Photoimmobilization of a bioactive laminin fragment and pattern-guided selective neuronal cell attachment. *Bioconjug. Chem.* **6,** 411–7 (1995).

163. Offenh?usser, A. *et al.* Microcontact printing of proteins for neuronal cell guidance. *Soft Matter* **3,** 290 (2007).

164. Millet, L. J., Stewart, M. E., Nuzzo, R. G. & Gillette, M. U. Guiding neuron development with planar surface gradients of substrate cues deposited using microfluidic devices. *Lab Chip* **10,** 1525–35 (2010).

165. Bowen, A. M., Ritchey, J. a, Moore, J. S. & Nuzzo, R. G. Programmable chemical gradient patterns by soft grayscale lithography. *Small* **7,** 3350–62 (2011).

166. Bélisle, J. M., Correia, J. P., Wiseman, P. W., Kennedy, T. E. & Costantino, S. Patterning protein concentration using laser-assisted adsorption by photobleaching, LAPAP. *Lab Chip* **8,** 2164–7 (2008).

167. Staii, C. *et al.* Positioning and guidance of neurons on gold surfaces by directed assembly of proteins using Atomic Force Microscopy. *Biomaterials* **30,** 3397–404 (2009).

168. Chodosh, L. A. Purification of DNA-binding proteins using biotin/streptavidin affinity systems. *Curr. Protoc. Mol. Biol.* **Chapter 12,** Unit 12.6 (2001).

169. Lu, T. *et al.* The immobilization of proteins on biodegradable fibers via biotin-streptavidin bridges. *Acta Biomater.* **4,** 1770–7 (2008).

170. Scott, M. a, Wissner-Gross, Z. D. & Yanik, M. F. Ultra-rapid laser protein micropatterning: screening for directed polarization of single neurons. *Lab Chip* **12,** 2265–76 (2012).

171. Chappert, C., Fert, A. & Van Dau, F. N. The emergence of spin electronics in data storage. *Nat. Mater.* **6,** 813–23 (2007).

172. Martí, X. *et al.* Electrical Measurement of Antiferromagnetic Moments in Exchange-Coupled IrMn/NiFe Stacks. *Phys. Rev. Lett.* **108,** 017201 (2012).

173. Jungwirth, T. *et al.* Demonstration of molecular beam epitaxy and a semiconducting band structure for I-Mn-V compounds. *Phys. Rev. B* **83,** 035321 (2011).

174. Wang, Y. Y. *et al.* Room-Temperature Perpendicular Exchange Coupling and Tunneling Anisotropic Magnetoresistance in an Antiferromagnet-Based Tunnel Junction. *Phys. Rev. Lett.* **109,** 137201 (2012).

175. Park, B. G. *et al.* Tunneling Anisotropic Magnetoresistance in Multilayer-(Co/Pt)/AlO_x/Pt Structures. *Phys. Rev. Lett.* **100,** 087204 (2008).

176. Molina-Ruiz, M. *et al.* Evidence of finite-size effect on the Néel temperature in ultrathin layers of CoO nanograins. *Phys. Rev. B* **83,** 140407 (2011).

177. Chu, J.-H. *et al.* In-plane electronic anisotropy in underdoped $Ba(Fe_{1-x}Co_x)_2As_2$ revealed by partial detwinning in a magnetic field. *Phys. Rev. B* **81,** 214502 (2010).

178. Sakuma, A., Fukamichi, K., Sasao, K. & Umetsu, R. First-principles study of the magnetic structures of ordered and disordered Mn-Ir alloys. *Phys. Rev. B* **67,** 024420 (2003).